



THE UNIVERSITY *of* EDINBURGH

Edinburgh Research Explorer

Cosmogenic Nuclide Systematics and the CRONUScalc Program

Citation for published version:

Marrero, S, Phillips, FM, Borchers, B, Lifton, N, Aumer, R & Balco, G 2016, 'Cosmogenic Nuclide Systematics and the CRONUScalc Program', *Quaternary Geochronology*.

Link:

[Link to publication record in Edinburgh Research Explorer](#)

Document Version:

Peer reviewed version

Published In:

Quaternary Geochronology

Publisher Rights Statement:

Copyright © 2015 Elsevier B.V. All rights reserved.

General rights

Copyright for the publications made accessible via the Edinburgh Research Explorer is retained by the author(s) and / or other copyright owners and it is a condition of accessing these publications that users recognise and abide by the legal requirements associated with these rights.

Take down policy

The University of Edinburgh has made every reasonable effort to ensure that Edinburgh Research Explorer content complies with UK legislation. If you believe that the public display of this file breaches copyright please contact openaccess@ed.ac.uk providing details, and we will remove access to the work immediately and investigate your claim.



1 Cosmogenic Nuclide Systematics and the CRONUScale 2 Program

3 Shasta M. Marrero^{a,b}, Fred M. Phillips^b, Brian Borchers^c, Nathaniel
4 Lifton^d, Robert Aumer^{e,c}, Greg Balco^f

5 ^a*Corresponding author; University of Edinburgh, School of Geosciences, Drummond*
6 *Street, Edinburgh, EH8 9XP, UK*

7 ^b*New Mexico Tech, Earth & Environmental Science Dept., Socorro, NM, 87801, USA*

8 ^c*New Mexico Tech, Department of Mathematics, Socorro, NM, 87801, USA*

9 ^d*Purdue University, West Lafayette, IN, USA*

10 ^e*Current position: BENTEK Energy, 32045 Castle Court, Ste. 200, Evergreen, CO*
11 *80439, USA*

12 ^f*Berkeley Geochronology Center, Berkeley, CA 94709, USA*

13 Abstract

14 As cosmogenic nuclide applications continue to expand, the need for a
15 common basis for calculation becomes increasingly important. In order to
16 accurately compare between results from different nuclides, a single method
17 of calculation is necessary. Calculators exist in numerous forms with none
18 matching the needs of the CRONUS-Earth project to provide a simple and
19 consistent method to interpret data from most commonly used cosmogenic
20 nuclides. A new program written for this purpose, CRONUScale, is presented
21 here. This unified code presents a method applicable to ¹⁰Be, ²⁶Al, ³⁶Cl, ³He,
22 and ¹⁴C, with ²¹Ne in testing. The base code predicts the concentration of
23 a sample at a particular depth for a particular time in the past, which can
24 be used for many applications. The multi-purpose code already includes
25 functions for calculating surface exposure age for a single sample or for a
26 depth profile containing multiple samples. The code is available under the
27 GNU General Public License agreement and can be downloaded and modified
28 to deal with specific atypical scenarios.

29 *Keywords:* cosmogenic nuclide, exposure age calculator, beryllium-10,
30 chlorine-36, aluminum-26, helium-3, carbon-14

1. Introduction

The CRONUS-Earth Project, funded by the U.S. National Science Foundation, is intended to improve many aspects of cosmogenic isotope use and help create a consistent, accurate use of the technique within the community. It functioned in collaboration with CRONUS-EU, a similarly motivated group in Europe funded by the European Commission. One important part of that project is the creation of a code that can consistently perform necessary calculations for different scaling schemes and that is applicable to many of the commonly used nuclides (^{10}Be , ^{26}Al , ^{36}Cl , ^3He , ^{14}C). The program presented here, called CRONUScalc, is a joint effort by the CRONUS Project to incorporate all major contemporary advances in the understanding of cosmogenic-nuclide production and to treat all the commonly used nuclides in an internally consistent fashion. This calculator directly incorporates much of the format and function of the $^{26}\text{Al}/^{10}\text{Be}$ code by Balco et al. (2008), but it extends the functionality beyond $^{26}\text{Al}/^{10}\text{Be}$ as well as introducing other new features. The new CRONUScalc code keeps the original modular format, but has updated the code with functions to perform production/accumulation calculations, calibrations, and surface and depth profile exposure ages and erosion rates.

The base code of CRONUScalc predicts the cosmogenic nuclide concentration in a sample (of either finite or point thickness) at a given depth at a particular time in the past. This function allows great versatility in earth science applications. CRONUScalc can be used to predict concentrations of a suite of nuclides for a variety of purposes. The code is published under the GNU General Public License, version 2 terms. The basic code can be modified to output many different parameters and can be downloaded (<https://bitbucket.org/cronusearth/cronus-calc>) and modified to suit a user's particular needs. The code repository is open to user contributions, allowing for sharing and future growth of the program. The version of the program described in this paper is marked online as Version 2.0 in the downloadable repository.

The code has been used to create two specific calculators to address the common need to calculate surface exposure ages from unknown samples. The two calculators that are included with the program are a single-sample surface exposure age calculator and a multi-sample depth-profile calculator. Additional functions in the code are designed to calibrate production rates, test alternative scaling frameworks, and determine erosion rates.

The fundamental theory and assumptions that have gone into the code are described in this paper. This paper matches the CRONUScalc downloadable version 2.0 available in the repository. There are significant new features in CRONUScalc as compared to previous calculators, including a more accurate method of integration through time and depth, updated geomagnetic history, newly produced calibration data sets, updated and calibrated muon production model, and the ability to calculate exposure ages for single samples at depth or perform a calibration.

2. CRONUScalc Program Systematics

The complete set of equations and fundamental theory behind the code can be found in Appendix A and will be useful for those new to the topic or interested in particular details because Appendix A systematically documents all the equations used in CRONUScalc, without need for the reader to refer back to numerous prior publications. The sections contained in the main body of the paper are designed to provide a general cosmogenic user with a summary of the systematics and relevant publications, focusing on the new research developments compared to the code described in Balco et al. (2008). A standard reference that describes the equations for production of cosmogenic nuclides is Gosse & Phillips (2001). The equations given in that paper have provided the baseline for numerous applications of cosmogenic nuclides. CRONUScalc is an implementation of equations from Gosse & Phillips (2001) and from newer sources, as described in each section.

2.1. Production Equations

2.1.1. Spallation

Cosmogenic-nuclide production from spallation, defined for this purpose as the interaction of a high-energy particle with a target nucleus producing a cosmogenic nuclide as a product of the reaction, follows a well-established exponential decrease with depth. At the surface, spallation is typically the dominant production mechanism. All the nuclides discussed in this paper are produced through at least one spallation pathway. The formula for the instantaneous production rate from spallation ($P_{s,m}$) is (Gosse & Phillips, 2001; Schimmelpfennig et al., 2008):

$$P_{s,m}(Z) = S_T \sum S_{el,s} P_{m,k}(0) C_k \exp\left(-\frac{Z}{\Lambda_{f,e}}\right), \quad (1)$$

100 where $P_{m,k}$ is the modern sea-level, high-latitude production rate of species
 101 m by spallation of element k at 2010 solar modulation (atoms $\text{g}^{-1} \text{a}^{-1}$); S_T
 102 is the topographic shielding factor (unitless); $S_{el,s}$ is the geographical scaling
 103 factor for spallation reactions for the particular reaction of interest, which
 104 varies temporally due to fluctuations in the geomagnetic field or solar mag-
 105 netic field (unitless); C_k is the concentration of the element k (atoms g^{-1}
 106 a^{-1}); and $\Lambda_{f,e}$ is the effective attenuation length for the spallogenic reactions
 107 (applies to fast neutrons and spallogenic protons) (g cm^{-2}). The production
 108 is summed for all target elements k that produce nuclide m to give the total
 109 spallation production rate.

110 *2.1.2. Epithermal and Thermal Neutrons*

111 Low-energy cosmogenic nuclide production, including that from thermal
 112 and epithermal neutrons, does not follow a simple exponential pattern with
 113 depth due to the atmosphere-ground interface effects. Low-energy neutrons
 114 produced in the upper ~ 50 cm of rock tend to diffuse upward out of the
 115 rock and into the atmosphere, resulting in a reduction of the flux as the rock
 116 surface is approached. Phillips et al. (2001) analytically solved the neutron-
 117 flux differential equation across the land/atmosphere interface to obtain the
 118 appropriate production equations.

119 The production of cosmogenic nuclides via the low-energy pathway is
 120 dependent on the neutron flux, which is, in turn, dependent on the composi-
 121 tion of the rock. In order to calculate production from this pathway using a
 122 universal parameter, the value $P_f(0)$ is calibrated instead of any parameter
 123 dependent on composition. The $P_f(0)$ parameter is the production rate of
 124 epithermal neutrons from fast neutrons in the air just above the surface. This
 125 parameter can be used in conjunction with the sample-specific composition
 126 to calculate the applicable production rates.

127 Cosmogenic nuclide production via low-energy neutrons is implemented
 128 as described in Gosse and Phillips (2001), except for a small modification
 129 to the calculation of muon-induced neutrons (discussed in Section 2.1.3). In
 130 several cases, small typos in Gosse and Phillips (2001) were also corrected
 131 (see the appendix for the corrected equations). Low-energy production is
 132 currently only implemented for ^{36}Cl , but could be modified by advanced
 133 users to apply to other nuclides with low-energy production pathways, such
 134 as ^3He .

2.1.3. Muons

Although muons make up a large portion of the incoming cosmic-ray flux at the earth’s surface, the low interaction rate means that they penetrate more deeply into the subsurface than neutrons. Muon contributions to total cosmogenic nuclide production are typically small at the surface, but become important at depth (Stone et al., 1998). Accurate calculation of muogenic production is thus important for sampling sites with large erosion rates or samples at depth.

Early calculators employed an exponential approximation for production from muons reactions according to Stone et al. (1998). Balco et al. (2008) implemented a newer model by Heisinger et al. (2002b,a) that calculates the production from muon reactions using physical parameters determined from laboratory irradiation experiments. Braucher et al. (2003) used a deep core to provide evidence that the parameters specified by Heisinger et al. (2002a,b) overestimated actual ^{10}Be production by fast muons by approximately a factor of two. This was supported by additional profile data measured by Braucher et al. (2011) and by Kim & Englert (2004), as well as reanalysis of previously published deep profile data by Braucher et al. (2013).

Rather than using parameters estimated from laboratory muon irradiations, the CRONUS-Earth Project has adopted values calibrated from nuclide-concentration profiles at carefully selected sites (Fig 1 in Phillips et al., 2015; Marrero, 2012; Borchers et al., 2015). A 30-m deep quartzite core from Antarctica has allowed the calibration of muon production parameters for ^{26}Al and ^{10}Be (Fig 1 in Phillips et al., 2015). For ^{36}Cl , previously published data sets (Evans, 2001; Stone et al., 1998) collected from quarry profiles were used to reparameterize the muon model for cosmogenic ^{36}Cl production from muons on Ca and K (Marrero, 2012). A CRONUS-Earth depth profile was not measured for ^{14}C , and ^{14}C profiles measured by other investigators (Kim et al., 2007; Lupker et al., 2013, 2015) have shown problems with distinguishing slow-muon production from production by muogenic neutrons, therefore at present CRONUScalc uses the values from Heisinger et al. (2002a,b) for ^{14}C . This may result in less accuracy for the calculation of muogenic ^{14}C production than for other nuclides, but ongoing investigations (Lupker et al., 2013, 2015) may yield improved parameter values in the near future.

Nuclide production by fast muon reactions ($P_{\mu,fast}$) is described by Equation 2 (Heisinger et al., 2002b). The parameter σ_0 was selected as the calibration parameter for the production of nuclides by muon reactions, as dis-

172 cussed in (Fig 1 in Phillips et al., 2015). This was mainly because it is the
 173 only nuclide-dependent parameter in the fast production equation. However,
 174 direct calibration of the σ_0 parameter also eliminates any dependence on the
 175 accuracy of the conversion from σ_{190} (the parameter measured in the labo-
 176 ratory irradiation experiments) to σ_0 (see Equation B.27, from Equation 14
 177 in Heisinger et al. (2002b)).

$$P_{\mu,fast} = S_T \phi_{\mu,total}(Z) \beta(Z) (\bar{E}(Z))^\alpha \sigma_0 N_{t,i} \quad (2)$$

178 Where the factor $\beta(Z)$ is a function of the mean total muon energy and
 179 is shown in Equation B.25 and \bar{E} is defined as the mean muon energy at a
 180 given depth Z and is shown in Equation B.26. $\phi_{\mu,total}$ is the total muon flux
 181 at the site, as calculated by the same equations used to calculate the fluxes
 182 for the Lifton et al. (2014) scaling framework. $N_{t,i}$ is the number density of
 183 the atoms in the target element (in units of at/g). This value is a constant
 184 for each nuclide unless the composition of the target changes, as it does for
 185 ^{36}Cl . α is an energy-dependent coefficient that parameterizes the energy
 186 dependence of the cross-section (σ) on muon energy. Experimental results
 187 permit values for α between 0.75 and >1.0 (Heisinger et al., 2002b) so the
 188 CRONUS-Earth Project chose a value of $\alpha = 1.0$. By assuming that α equals
 189 one, β will also be equal to one.

190 Nuclide production by slow negative muon capture ($P_{\mu-}$) is described by
 191 Equation 3, originally from Charalambus (1971) and discussed in detail for
 192 ^{36}Cl by Stone et al. (1998). The production rate depends on the stopping rate
 193 of negative muons ($\phi_{\mu-}$) as well as the nuclide-dependent factors ($f_{i,C}$, $f_{i,D}$,
 194 f_i^*). $\phi_{\mu-}$ is derived from the muon flux calculated by the same equations used
 195 in Lifton et al. (2014). $f_{i,D}$ is the fraction of muons stopped by element k and
 196 absorbed by the nucleus before decay of the muon. $f_{i,C}$, the compound factor,
 197 represents the fraction of the muons that are captured by a target element
 198 (as opposed to the other elements present) within the bulk rock. The formula
 199 for the compound factor (Equation E.40) is taken from Charalambus (1971)
 200 and the values are consistent with those used by Heisinger et al. (2002a).

$$P_{\mu-} = S_T \phi_{\mu-}(Z) f_{i,C} f_{i,D} f_i^* \quad (3)$$

201 The remaining parameter, f_i^* , the particle emission channel probability,
 202 is the probability that the excited nucleus of the target atom will emit the
 203 proper particle to result in transformation to the nuclide of interest. Heisinger
 204 et al. (2002a) experimentally determined f_i^* values for the production of ^{26}Al

205 (from Si), ^{10}Be and ^{14}C (from O), and ^{36}Cl (from K and Ca), but these
 206 values tend to overestimate nuclide concentrations measured in depth profiles
 207 in the same fashion as for fast muon production (Fig 1 in Phillips et al.,
 208 2015; Braucher et al., 2011). The production parameters for slow negative
 209 muon capture, f_i^* , were calibrated by fitting to the measured CRONUS-Earth
 210 profile for ^{10}Be and ^{26}Al and by fitting to previously published profiles
 211 for ^{36}Cl , as previously discussed.

212 The muon-capture reactions can release neutrons that later participate
 213 in neutron-capture reactions (muon-induced neutrons). Instead of assuming
 214 an exponential decrease in muon production with depth to calculate this
 215 flux, as most previous calculators do, the new muon module described above
 216 is used to calculate production with depth. The muon code calculates the
 217 negative muon stopping rate ($\phi_{\mu-}(Z)$) and total muon flux ($\phi_{\mu f}(Z)$) terms
 218 at a given depth for the calculation of the production rate of muon-induced
 219 neutrons (Equation 4). This muon-induced neutron production rate is used
 220 in the thermal and epithermal neutron flux equations (Equations B.30 and
 221 B.34), which are ultimately used to determine the production rate via the
 222 low-energy neutron pathway.

$$P_{n,\mu}(Z) = Y_s \phi_{\mu-}(Z) + 5.8 \times 10^{-6} \phi_{\mu f}(Z), \quad (4)$$

223 where Y_s is the average neutron yield per stopped negative muon (Fabryka-
 224 Martin, 1988).

225 2.1.4. Radiogenic Production

226 Radiogenic production in this context refers to the generation of low-
 227 energy neutrons by reactions related to the radioactive decay or spontaneous
 228 fission of U or Th, and the subsequent absorption of those neutrons to pro-
 229 duce nuclides of interest, principally ^{36}Cl . Although ^3He is also produced
 230 from Li in this manner (Lal, 1987; Dunai et al., 2007), only ^{36}Cl radiogenic
 231 subtraction is incorporated into the program and the discussion below focuses
 232 on ^{36}Cl for that reason. The radiogenic low-energy neutron flux is assumed to
 233 be in equilibrium with the concentrations of uranium (U) and thorium (Th)
 234 in the rock. This component is quantified using measured concentrations
 235 of U and Th and the method described in Fabryka-Martin (1988), which is
 236 based on the formulations developed by Feige et al. (1968). These equations
 237 are shown in Appendix B.5.

238 The quantification of the bulk rock properties requires fundamental nu-
 239 clear properties for each element. The original table of these properties pre-

240 sented in Fabryka-Martin (1988) has now been corrected and updated using
 241 the information in Mughabghab (2006) and Schimmelpfennig et al. (2009).
 242 A table of nuclear properties for all the elements considered in CRONUScale
 243 is shown in Table 1.

244 In most studies, the rocks (not the exposure age) are sufficiently old that
 245 the assumption of equilibrium is reasonable. Even for younger features, such
 246 as a newly-erupted basalt, the assumption of equilibrium is reasonable due to
 247 equilibration with the uranium and thorium concentrations prior to eruption,
 248 so long as the magma did not undergo differentiation or mixing that signifi-
 249 cantly changed its U and Th contents less than ~ 0.5 Ma prior to sampling.
 250 The alternative is to allow production from radiogenic sources to begin at
 251 the exposure age (or any rock formation age). This difference in assumption
 252 is small for most ^{36}Cl samples and no data set currently exists to differen-
 253 tiate between the two assumptions. This assumption is only significant for
 254 young samples with high chlorine contents ($> 50\%$ production from Cl) or
 255 significant U or Th.

256 2.2. Calibration Technique

257 The production rates incorporated into the CRONUScale code are the
 258 results from CRONUS-Earth Project calibrations. The calibration data set
 259 compiled by CRONUS-Earth includes a large number of sites representing a
 260 large range of latitudes, longitudes, and elevations. Ideal sites should have
 261 little uncertainty in the sample parameters (e.g. erosion rate, elevation,
 262 shielding, independent age constraints, etc.). The sites were divided into
 263 two categories based on the quality of the site, with the sites that came clos-
 264 est to fitting the criteria above placed into the 'primary calibration data set'.
 265 Additional sites with independent age constraints, but not meeting the strict
 266 criteria for primary sites, were placed into the 'secondary data set'. These
 267 samples are independent of the primary calibration data set and therefore
 268 can be used to assess the final calibrated parameters.

269 The calibration method, data set details including references, and the
 270 spallation calibration results for all nuclides are discussed in detail in Borchers
 271 et al. (2015). Additionally, some details of the ^{10}Be and ^{26}Al muon calibration
 272 can be found in Phillips et al. (2015) and the full chlorine-36 calibration can
 273 be found in Marrero (2012); Marrero et al. (2015).

El.	A_i	ξ_i	$\sigma_{sc,i}$	$\sigma_{th,i}$	$I_{a,i}$	S_i	$Y_{n,i}^u$	$Y_{n,i}^{th}$	K_m	$St.$	#	P
—	[g/mol]	[—]	[b]	[b]	[1×10^{-24}]	[—]	[—]	[—]	[—]	[—]	[—]	[—]
O	16	0.120004104	3.761	0.00019	0.0002693	539	0.23	0.079	0	0	8	1.00
H	1.01	1	20.49	0.3326	0	1542	0	0	0	0.5	1	0.00
C	12.01	0.157760474	4.74	0.0035	0.0018	573	0.45	0.18	13.691	2	6	0.36
Na	22.99	0.084543589	3.038	0.517	0.311	454	14.5	6.8	19.42	0.5	11	1.00
Mg	24.31	0.08009077	3.414	0.0666	0.038	463	5.8	2.6	14.94	1	12	0.93
Al	26.98	0.072337427	1.413	0.231	0.17	449	5.1	2.6	11.812	1.5	13	0.76
Si	28.09	0.069559975	2.044	0.171	0.082	455	0.69	0.335	10.01	2	14	0.84
P	30.97	0.063210393	3.134	0.165	0.079	444	0	0	8.48	2.5	15	1.04
K	39.1	0.050295528	2.04	2.1	1	432	0.45	0.305	12.78	0.5	19	1.54
Ca	40.08	0.049086179	2.93	0.43	0.233	436	0	0	10.73	1	20	1.90
Ti	47.87	0.041208508	4.09	6.41	3.1	367	0	0	7.53	2	22	2.66
Mn	54.94	0.035968204	2.06	13.36	13.4	351	0	0	8.486	1	25	2.73
Fe	55.85	0.035390922	11.35	2.56	1.36	353	0.19	0.205	7.54	1.5	26	3.28
Cl	35.45	0.055371497	15.8	33.14	13.83	420	0	0	16.98	0	17	1.32
B	10.81	0.174236264	4.27	767	343	537	62.3	19.2	55.68	0	5	0.25
Sm	150.36	0.013242694	38	9640	1400	0	0	0	4.004	0	62	4.4
G	157.25	0.012664667	172	41560	390	0	0	0	3.828	0	64	5.8
U	238.03	0.008378873	9.08	2.68	277	0	0	0	2.529	0	92	4.7
Th	232.04	0.008594581	13.55	7.34	83.3	0	0	0	2.594	0	90	3.0
Li	6.9	0.264	0.95	70.5	0.0	548	21.1	9.6	86.731	0.0	3	0.18
Cr	52.0	0.038	3.38	3.1	1.6	0.0	0.0	0.0	11.578	0.0	24	2.98

Table 1: Table of constants used for elemental parameters. The table was originally taken out of Fabryka-Martin (1988). It has been updated using Mughabghab (2006). El is the element; St is the stoichiometry. Note: 1 barn (b)= 1×10^{-24} cm². The columns correspond to the following parameters: A_i - Atomic weight of element; ξ_i - Average log decrement of energy per neutron collision with element i; $\sigma_{sc,i}$ - Neutron scattering cross-section of element i; $\sigma_{th,i}$ - Thermal neutron absorption cross-section of element i; $I_{a,i}$ - Dilute resonance integral for element i; S_i - Mass stopping power of element i for alpha particles of a given energy; $Y_{n,i}^u$ - neutron yield of element i per ppm U in radioequilibrium; $Y_{n,i}^{th}$ - Neutron yield of element i per ppm Th in radioequilibrium; K_m - 602/atomic weight of sample, used to convert to at/g from ppm; $St.$ - Stoichiometric ratio of oxide (oxygen to element i); # - Atomic number; **P** - Average capture probability relative to oxygen.

2.3. Production Rate Scaling

Cosmogenic nuclide scaling applies the physics governing the modulation of the cosmic-ray flux by atmospheric mass and the terrestrial and solar magnetic fields to provide production rates as a function of location and exposure time. Numerous scaling frameworks have been proposed in order to correct for latitude, elevation, atmospheric pressure anomalies, dipole and non-dipole geomagnetic field changes, and solar modulation. CRONUScale implements seven scaling frameworks, as summarized in Table 2. This includes the original model by Lal (1991), further developed by Stone (2000) (referred to as St), that was based on cosmic-ray emulsion data and some neutron monitor data. A version of the Lal/Stone scaling accounting for geomagnetic field variations is also included (Lm). CRONUScale includes the neutron-monitor-based models of Dunai (Du) (Dunai, 2000, 2001a), Lifton (Li) (Lifton et al., 2005), and Desilets (De) (Desilets & Zreda, 2003; Desilets et al., 2006b). Finally, CRONUScale implements two new models based on Lifton et al. (2014). The Lifton-Sato-Dunai (LSD, denoted SF herein) scaling framework (Lifton et al., 2014) does not rely on empirical fitting to a set of measured data points, but instead is based on analytical fits to physics-based modeling, and has been tested against measured atmospheric secondary nucleon and muon energy spectra.

The energy spectrum of the cosmic-ray flux produced by the LSD framework provides information that is available neither from the traditional Lal (St) scaling, nor neutron-monitor based scaling (Du, Li, De). This, in turn, allows the production rates of cosmogenic nuclides to be calculated by integrating the energy-dependent excitation function with the calculated particle energy spectrum. This is termed “nuclide-dependent scaling” because it results in a separate scaling factor for each nuclide, rather than a single scaling factor applicable to all nuclides, as the previous methods did. In the case of ^{36}Cl , for example, this results in six nuclide-dependent scaling factors, including four high-energy scaling factors to scale the spallation reactions (K, Ca, Ti, and Fe) and one generalized spallation reaction to scale the low-energy reactions. Due to the derivation from the high-energy flux, the low-energy pathways cannot be scaled using the incoming low-energy neutron flux. (Note that since ^{36}Cl is commonly measured in rocks of varying compositions, each reaction has to be individually weighted by the concentration of the target element in the rock, unlike nuclides such as ^{10}Be or ^{26}Al that are commonly measured in minerals of constant composition, such as quartz). In all of the other scaling frameworks, the nuclide-dependent scaling factors still appear in

the code, but all are set equal to the single scaling factor produced by the selected scaling framework. This nuclide-dependent scaling framework (LSDn, denoted SA herein) is the default on the online interface due to its favorable calibration results (see Borchers et al. 2015) and the possibility for future incorporation of updates to the excitation functions and other physics-based research. For all the details of the scaling frameworks themselves, please see the original papers (cited in Table 2); for details of implementation, please see the description in Balco et al. (2008) and Lifton et al. (2014).

In CRONUScalc, the geomagnetic history is consistent across all scaling frameworks, even though each model uses the history in a slightly different manner. This information is available in the code and can be modified directly if a different geomagnetic history is necessary. References for the currently implemented geomagnetic history can be found in Table 3, with relevant details in Lifton et al. (2014). The calculator is flexible, allowing knowledgeable users to modify the code to incorporate alternative geomagnetic models.

Although the various paleomagnetic reconstructions are in broad agreement, there are considerable differences for certain time intervals, indicating some uncertainty with regard to the accuracy of each reconstruction. In addition, each reconstruction contains internal uncertainties stemming from uncertainties in the measurements and chronology. We do not attempt to propagate these uncertainties into the CRONUScalc ages. This is partly due to the difficulty of quantifying the unknown errors in each reconstruction (for example, the assumed constant geomagnetic field of the St model is also clearly in error, but how does one quantify the magnitude and propagate it into the resultant age?). When considering the entire CRONUS-Earth secondary calibration data set (Borchers et al., 2015), the difference between the average normalized Lal-Stone (St; constant geomagnetic field) ages and the Lal (1991) (Lm; time-varying field) ages is only 0.4%, and increases to 1.8% for the same comparison at the high-elevation, low-latitude Breque, Peru, site. However, due to the approximately sinusoidal dipole variation over the exposure time of a significant number of the calibration sites, these comparisons may still underestimate the differences when sample exposure is integrated over longer time spans in which the time-integrated effects might not cancel (<ca. 100 ka). Considering the difficulty of quantifying this uncertainty and propagating it, and the minimal effect the effort would have on age uncertainties for a majority of samples, we have neglected it. We acknowledge that for older or younger samples especially at low latitude, the

Abbr.	Reference	Description
St	Lal (1991); Stone (2000)	Time-independent (constant production rate). Based on two different types of neutron reaction counting methods (photographic emulsions and neutron monitors). Scaling factor inputs are geographic latitude and atmospheric pressure, based on the Stone (2000) modification.
Lm	Lal (1991); Nishiizumi et al. (1989)	Time-dependent version of St based on time-variation in the dipole magnetic field intensity, as formulated by Nishiizumi et al. (1989).
Li	Lifton et al. (2005, 2008)	Time-dependent model based on neutron monitor measurements and incorporating dipole and non-dipole magnetic field fluctuations and solar modulation. The scaling factor is based on actual atmospheric pressure, solar modulation, and a cutoff rigidity calculated using trajectory tracing.
Du	Dunai (2000, 2001a,b)	Time-dependent model based on neutron monitor measurements and incorporating dipole and non-dipole magnetic field fluctuations. The scaling factor is based on an analytically calculated cutoff rigidity and atmospheric pressure. A long-term mean for solar modulation is used in this model.
De	Desilets et al. (2006b); Desilets & Zreda (2003)	Time-dependent model based on neutron monitor measurements and incorporating dipole and non-dipole magnetic field fluctuations. The scaling factor is based on a cutoff rigidity calculated using trajectory tracing and the actual atmospheric pressure.
LSD (Sf)	Lifton et al. (2014)	Time-dependent model based on equations from a nuclear physics model and incorporating dipole and non-dipole magnetic field fluctuations and solar modulation. The scaling factor is based on actual atmospheric pressure, solar modulation, and a cutoff rigidity calculated using trajectory tracing. The total flux (protons+neutrons) is used to scale all reactions.
LSDn (Sa)	Lifton et al. (2014)	Time-dependent model based on equations from a nuclear physics model and incorporating dipole and non-dipole magnetic field fluctuations and solar modulation. The scaling factor is based on actual atmospheric pressure, solar modulation, and a cutoff rigidity calculated using trajectory tracing. Nuclide-dependent scaling is implemented by incorporating cross-sections for the different reactions.

Table 2: Table of scaling frameworks, including abbreviations, original references, and a brief description of each model.

Time period (kyr)	Model name	Reference
3-7ka	CALS7k	Korte & Constable (2005)
7-18ka	GLOPIS-75	Laj et al. (2004)
18ka-2Ma	PADM2M	Ziegler et al. (2011)

Table 3: Geomagnetic history used in all the scaling frameworks.

effect might be larger and we hope that quantification will be addressed in future research. The geomagnetic models used may also include systematic spatial or temporal biases that may be resolved with further research.

While CRONUScalc offers seven different spallation scaling frameworks, it uses only one muon scaling model. Muons were not natively scaled in any of the original models, so we use the energy-dependent Lifton et al. (2014) muon model to scale the muon flux.

A new input to the code is the “year collected” that allows the scaling frameworks to more precisely account for the time of exposure. In previous calibrations, the independent age constraints have been listed as “before present.” For radiocarbon analyses, this is actually “years before 1950.” The calibrations have been updated accordingly and now list independent ages as “years before 2010” and the exposure age calculation routines in CRONUScalc now integrate production through the collection year. For most samples, this is not a critical change, but with the advent of very high-precision cosmogenic ages on very young samples (e.g. Schaefer et al. 2009), it will eliminate the need for ad-hoc corrections for sample date. This capability will only become more important through time. The sample is assumed to have been processed shortly after collection or to have been stored where continued production and decay would be insignificant.

2.4. Attenuation Length

The apparent attenuation length, the attenuation length with respect to a flat surface with no topographic shielding, quantifies the depth distribution of the production by neutron spallation. When the apparent attenuation length is adjusted to account for the dip of the sample surface and any topographic shielding, the result is the effective attenuation length, $\Lambda_{f,e}$. The effective attenuation length is the parameter that should be used in calculations pertaining to production from a particular sample.

The effective attenuation length is an input parameter for each sample. The web-based user interface automatically calculates the effective attenua-

Depth/Cut. Rig.	1100	1000	900	800	700	600	500	400
0	151	152	153	154	155	158	163	172
4	152	152	154	156	159	164	171	185
8	156	159	161	164	168	175	185	204
12	162	165	168	171	176	184	196	218
16	168	170	172	177	182	191	204	228
20	169	171	174	179	184	192	206	231

Table 4: The table used for the interpolation of attenuation lengths based on the given atmospheric depth (top row, in units of g/cm²) and cutoff rigidity (first column, in units of GV). Values based on those obtained using the spreadsheet that accompanied Sato et al. (2008), but include the additional 11.1% correction discussed in the text.

tion length if it is not provided. For use in the raw code where attenuation
length is not automatically calculated, there is a function (`attenuationlengthnormal.m`)
to calculate the parameter at a given location (latitude, longitude, elevation)
and pressure of a sample. The attenuation-length model in CRONUScalc is
based on atmospheric attenuation lengths calculated from the PARMA model
of Sato et al. (2008), which is an analytical model for estimating cosmic-ray
spectra in the atmosphere. The attenuation lengths are interpolated from
the values given in Table 4 using the vertical cutoff rigidity and atmospheric
depth of the site.

The interpolated attenuation lengths have been adjusted upward by 11.1%
to account for systematic differences between atmospheric and lithospheric
attenuation. This adjustment is based on the approximate relation:

$$\frac{\lambda_{f,rock}}{\lambda_{f,atm}} = \left(\frac{A_{rock}}{A_{atm}}\right)^{1/3} \quad (5)$$

where A_{rock} and A_{atm} are the average atomic weights of the rock and
atmosphere, respectively. The average atomic weight of the atmosphere was
taken to be 14.68 g mole⁻¹ and that of average rock 20.40 g mole⁻¹. (We note
that any changes in the chemical composition of the atmosphere over the time
scale of interest for application of cosmogenic-nuclide surface chronology are
too small to affect the attenuation length.) This relation is derived from the
following simple considerations.

The macroscopic cross-sectional area of the atoms in a gram of matter
scales as the product of the number of atoms of each element in the volume

401 multiplied by the average cross-sectional area of the atoms. Assuming that
 402 atomic nuclei are spheres of constant density, and that each nucleus is made
 403 up of spheres of uniform mass and diameter (protons and neutrons), the
 404 radius of each atom will scale by the atomic weight to the one-third power
 405 (Friedlander et al., 1981). The cross-sectional area will then scale as the
 406 square of the radius. The product of these is the average atomic cross-
 407 section to the two-thirds power. The number of atoms per gram will scale
 408 by Avogadro’s number divided by the average atomic weight. Therefore,
 409 the macroscopic cross-sectional area of substance *i* (rock or atmosphere), per
 410 gram, will scale as follows:

$$Area_i \propto \frac{N_A A_i^{2/3}}{A_i} = \frac{N_A}{A_i^{1/3}} \quad (6)$$

411 where N_A is Avogadro’s number. The apparent attenuation length is the
 412 inverse of the macroscopic area per gram. When the ratios of the attenuation
 413 lengths for rock and atmosphere are taken, Equation 5 results. (John Stone,
 414 personal communication, 14 February 2012).

415 The attenuation length will also vary as a function of lithology. The
 416 average atomic weight of common lithologies varies from 19.8 g mole⁻¹ for
 417 quartzite to 21.5 g mole⁻¹ for ultramafic rocks. However, the maximum
 418 difference between the attenuation length calculated for any lithology and
 419 that for the mean atomic weight (averaged over all lithologies) is <2 %.
 420 This is insignificant and hence CRONUScalc does not compute attenuation
 421 lengths on a lithology-specific basis. There is some modeling evidence to
 422 suggest that nuclide-dependent attenuation lengths may be needed in the
 423 future (Argento et al., 2014), something the calculator is already equipped
 424 to accommodate because attenuation length is a sample input.

425 Figure 1 shows the dependence of the modeled effective attenuation length
 426 on elevation and latitude. For samples with large topographic shielding cor-
 427 rections, these values should be adjusted to account for horizon obstructions.

428 The final attenuation lengths overlap with the range of values presented
 429 by Dunai (2000) from 121 to >170 g/cm², with the range for most samples
 430 falling between 150-190 g/cm² (see Figure 1). Although the results are in the
 431 same range as commonly assumed values of 160-170 g cm⁻² (Gosse & Phillips,
 432 2001; Dunai, 2010), a significant difference in age between the use of the two
 433 different attenuation lengths (CRONUS-predicted value vs 170 g cm⁻²) is
 434 possible for samples with high erosion rate, very long exposure times, or at

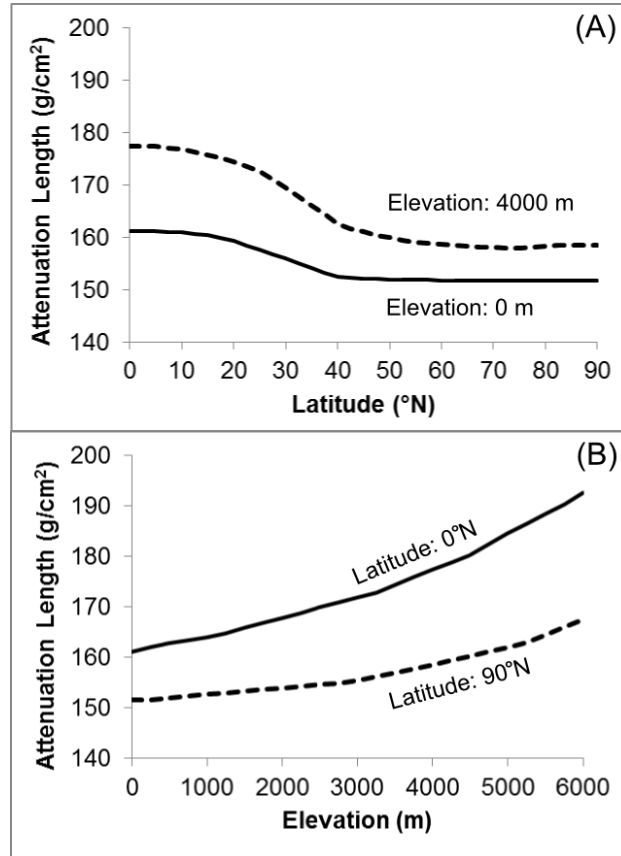


Figure 1: The change in effective attenuation length for a flat surface at various elevations (A), shown for both zero and 90°N latitude, and effective attenuation length at various latitudes (B), shown for elevations of 0 and 4000 m.

435 significant depth. In order to test the magnitude of this effect, we predicted
 436 ^{10}Be concentrations using the CRONUScalc modeled attenuation length of
 437 153 g/cm^2 (corresponding to 40°N at sea level) for artificial samples for a
 438 range of ages and erosion rates. The resulting ages were then determined
 439 using an attenuation length of 170 g/cm^2 . The results (Figure 2, B.6) show
 440 that the attenuation length change from 153 g/cm^2 to 170 g/cm^2 results in
 441 up to a 2% difference on the 20 ka age for erosion rates up to 10 mm/kyr .
 442 The difference is considerably larger for faster eroding samples with longer
 443 exposure times, or alternately samples at depth, with differences of almost
 444 50 % for 300 ka exposure times with erosion rates of 10 mm/kyr . However,
 445 for most surface samples with modest or low erosion rates, this difference is
 446 relatively small. When depth profiles are available, the attenuation length
 447 should still be one of the fitted parameters to ensure the most accurate value
 448 (e.g. Braucher et al. 2013). Use of the surface shielding calculator to estimate
 449 attenuation lengths for depth profiles or very high erosion rates should be
 450 approached with caution.

451 Given the physics-based derivation of the new attenuation length model,
 452 the new attenuation lengths are implemented as the default in the online
 453 calculator interface. However, as this parameter is an input for each sample,
 454 the choice of attenuation length is ultimately left to the user. The final model
 455 for attenuation length is included as its own function in the code repository
 456 (see the Function Appendix in the supplementary materials). A separate
 457 shielding calculator has been developed to simplify the calculation of the
 458 topographic shielding factor as well as the appropriate effective attenuation
 459 length. The attenuation length model accounts for the latitude and elevation
 460 of a sample. If shielding information is included, the effective attenuation
 461 length is modified accordingly. A link to the shielding calculator is available
 462 on the calculators homepage (<http://web1.ittc.ku.edu:8888/>).

463 2.5. Accumulation

464 Instantaneous production rates, such as those described above, must be
 465 integrated in both time and thickness in order to calculate the production
 466 in a real sample. In many common solutions, this is done analytically or
 467 with additional multiplicative factors to account for the finite thickness of
 468 a sample. In the CRONUScalc program, this integration is done numeri-
 469 cally, which is more accurate for depth integrations and makes it simple to
 470 incorporate time-dependent scaling and varying production rates.

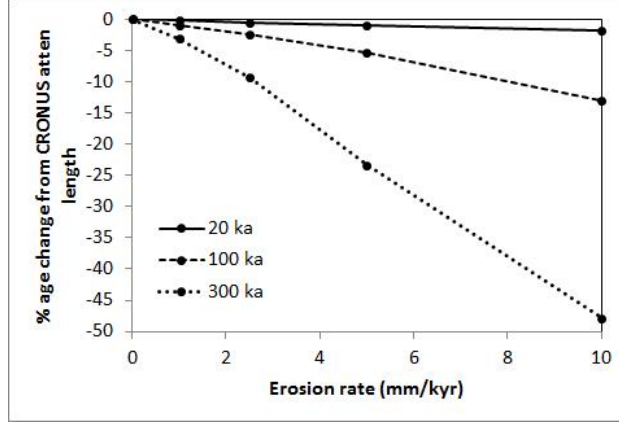


Figure 2: Change in ages due to change in attenuation length from the original CRONUS-calculated value (153 g/cm^2) to 170 g/cm^2 , compared over a range of erosion rates (0, 1, 2.5, 5, and 10 mm/kyr) and three different exposure ages (20, 100, and 300 ka).

471 For a given age, an appropriate time step, Δt , is found such that the
 472 erosion rate is small for that period and the changes in time-dependent pro-
 473 duction rates are not too large. Although larger time steps may be appropri-
 474 ate for some samples or scaling methods, the time step default is set to 100
 475 years in order to maintain time-step errors below 0.4% for all sample types,
 476 as calculated assuming the correct age is the age produced using a time step
 477 of 1 year.

478 The sample begins at depth and the cosmogenic inventory within the
 479 sample is tracked during its migration to the surface. For each time step, the
 480 current scaling factors and production rates are found for the sample. The
 481 inventory accounts for the decay of all previously produced nuclide inventory
 482 (the first term in Equation 7) as well as the production and decay of the
 483 nuclide during the current time step (second term in Equation 7).

$$N_{tot} = N_{prev}e^{-\lambda\Delta t} + P_{tot} * f_{decay} \quad (7)$$

484 where N_{tot} is the total inventory in the sample up to the current time step;
 485 N_{prev} is the inventory from all previous time steps; λ is the decay constant
 486 for the nuclide; P_{tot} is the instantaneous production rate of the nuclide from
 487 all mechanisms; and f_{decay} is the decay factor (Equation 8) that accounts for
 488 the fact that a small amount of the nuclide produced at the beginning of the

time period will have decayed by the end of the period.

$$f_{decay} = \frac{1 - e^{-\lambda\Delta t}}{\lambda} \quad (8)$$

After the nuclide is produced, the samples are “eroded” by updating the depths for the sample by using the erosion rate and the time step, as shown in Equation 9.

$$D_{new} = D_{previous} - \Delta t * \epsilon \quad (9)$$

where D_{new} is the new depth, D_{prev} is the previous sample depth, and ϵ is the erosion rate of the surface.

These steps are repeated from $t=(\text{year sampled})$ -age, with the sample at depth, until t is equal to the year sampled, when the sample reaches the surface. The inventory is then returned by the module and used in any number of other functions, such as surface or depth-profile calculators, or simply returned to the user.

3. Considerations Specific to Individual Cosmogenic Nuclides

While the in-situ cosmogenic nuclides share many similarities in terms of production pathways, they are each produced by a different combination of pathways and there are other individual issues that need to be addressed. In the following sections, the specific pathways for production, uncertainties, and other issues are documented for each of the major four code modules representing five nuclides.

Each nuclide is produced by one or more of the pathways discussed in the previous section. The most common reactions are shown in Table 5 for common nuclides and their common target minerals.

Inputs required by CRONUScalc vary, but the inputs common to all nuclides include location (latitude, longitude, elevation/pressure), sample parameters (thickness, bulk density, depth, and attenuation length), site parameters (topographic shielding, erosion rate, year collected), and chemical parameters (cosmogenic nuclide concentration). Additional inputs are necessary for some nuclides to account for production through low-energy neutron pathways (composition, water content). For all nuclides, the required cosmogenic nuclide concentration is assumed to incorporate any blank corrections, as these vary from lab to lab and therefore cannot be standardized to be included in the program.

Nuclide	Reaction
^3He	Spallation: O, Mg, Si, Ca, Fe, Al $^6\text{Li}(\text{n},\alpha)^3\text{He}$
^{10}Be	$^{16}\text{O}(\text{n},4\text{p}3\text{n})^{10}\text{Be}$ $^{28}\text{Si}(\text{n},\text{x})^{10}\text{Be}$ $^{16}\text{O}(\mu^-, \alpha\text{pn})^{10}\text{Be}$ $^{28}\text{Si}(\mu^-, \text{x})^{10}\text{Be}$
^{14}C	$^{16}\text{O}(\mu^-, 2\text{p})^{14}\text{C}$ $^{16}\text{O}(\text{n}, 2\text{pn})^{14}\text{C}$ $^{17}\text{O}(\text{n}, \alpha)^{14}\text{C}$ $^{28}\text{Si}(\text{n}, \text{x})^{14}\text{C}$
^{26}Al	$^{28}\text{Si}(\text{n}, 2\text{pn})^{26}\text{Al}$ $^{28}\text{Si}(\mu^-, 2\text{n})^{26}\text{Al}$
^{36}Cl	$^{40}\text{Ca}(\text{n}, 2\text{n}3\text{p})^{36}\text{Cl}$ $^{39}\text{K}(\mu^-, \text{p}2\text{n})^{36}\text{Cl}$ $^{40}\text{Ca}(\mu^-, \alpha)^{36}\text{Cl}$ $^{35}\text{Cl}(\text{n}, \gamma)^{36}\text{Cl}$ $^{39}\text{K}(\text{n}, \alpha)^{36}\text{Cl}$ $\text{Fe}(\text{n}, \text{x})^{36}\text{Cl}$ $\text{Ti}(\text{n}, \text{x})^{36}\text{Cl}$

Table 5: Common reactions producing in-situ terrestrial cosmogenic nuclides (Gosse & Phillips, 2001). The symbolism is as follows for the X(a,b)Y reaction: X is the target element, a is the particle interacting with the target, b is emitted during the reaction, and Y is the final nuclide product. "x" in the second place inside the parentheses indicates a reaction for which several different combinations of emitted particles are possible. Reactions are only shown for the pathways discussed in the paper. For beryllium, aluminum, and carbon, only those reactions possible in a quartz target mineral are shown.

3.1. Aluminum-26 and Beryllium-10

^{10}Be is the most commonly used cosmogenic nuclide. ^{26}Al is also produced in quartz and is commonly processed in the same samples as ^{10}Be . Both nuclides are produced in quartz through only two mechanisms: spallation and muogenic production. Muogenic production of ^{10}Be and ^{26}Al accounts for only $\sim 1.5\%$ and $\sim 2\%$ of total surface SLHL production, respectively, as calculated using CRONUScalc. CRONUScalc employs the currently accepted half-life and AMS standard values for ^{10}Be (Nishiizumi et al., 2007; Korschinek et al., 2010; Chmeleff et al., 2010). The online interface performs automatic renormalization for all ^{10}Be and ^{26}Al concentrations based on the standards selected by the user. The interface passes this information to the underlying raw CRONUScalc program, which assumes the concentration is normalized to 07KNSTD for ^{10}Be and KNSTD for ^{26}Al . For discussions concerning these normalizations, see Balco et al. (2008) and Nishiizumi et al. (2007).

When ^{26}Al and ^{10}Be are both being analyzed for a particular sample, they can be processed in the same quartz split. The code operates in a fashion similar to that of Balco et al. (2008) in that it allows any given sample to be associated with data from either ^{10}Be or ^{26}Al , or both nuclides. The production rates for both nuclides have only been determined reliably in quartz, so this is the only mineral target supported by CRONUScalc at this time.

Additional information, such as erosion rate or burial history, can be determined if more than one nuclide is analyzed in a sample (Bierman, 1994; Granger & Muzikar, 2001). The common Al/Be pair is frequently used for these investigations. CRONUScalc does not currently provide figures for the paired interpretation if ^{10}Be and ^{26}Al , but these capabilities could be added by an advanced user following the method described in Granger & Muzikar (2001); Granger (2006).

For information on the production rates used in the calculator, see the CRONUS-Earth spallation production rate calibration paper (Borchers et al., 2015) or the summary paper (Phillips et al., 2015).

3.2. Chlorine-36

Cosmogenic ^{36}Cl is produced by a wide range of pathways that have been discussed in the production systematics section. The main three pathways are spallation (Ca, K, Ti, Fe), low-energy neutron absorption (Cl), and muogenic production (Ca, K, Ti, Fe). Note that we include the production of ^{36}Cl

557 by relatively low-energy neutrons (down to approximately 3 MeV) by the
558 reaction $^{39}\text{K}(\text{n},\alpha)^{36}\text{Cl}$ in the "spallation" category, using the cross-section of
559 Reedy (2013), since this energy is still well above the epithermal level.

560 Previous studies have resulted in production-rate estimates that differ
561 from each other by up to 40%. One goal of the CRONUS-Earth project
562 was to resolve these uncertainties (Marrero, 2012; Marrero et al., 2015, this
563 volume, submitted). For spallation production rates, only CRONUS-Earth
564 mineral separate data is used in the calibration and the resulting production
565 rates fit the independent secondary data set very well (see evaluation of the
566 secondary ^{36}Cl data set in Borchers et al. (2015)). For the low-energy neu-
567 tron production pathway, however, there are additional unknown complicat-
568 ing factors, potentially water content or other site-specific parameters, which
569 influenced the $P_f(0)$ calibration. A more complete discussion of calibration
570 results and factors affecting ^{36}Cl production can be found in Marrero et al.
571 (2015), but the resulting value for $P_f(0)$ fits the secondary data set well and
572 is used in CRONUScalc until additional ^{36}Cl calibrations can be performed.
573 The $P_f(0)$ value that was obtained during the CRONUS-Earth calibration
574 has a larger uncertainty (about 20%) than the other ^{36}Cl production param-
575 eters. Ideally, ^{36}Cl should be measured on low-chlorine mineral separates to
576 eliminate the uncertainty associated with this pathway (cf. Schimmelpfennig
577 et al. 2009). Analysis of low-chlorine mineral separates should help to keep
578 ^{36}Cl ages to a similar level of uncertainty as other nuclides.

579 It is important to note that the predicted nuclide concentrations are more
580 sensitive to certain parameters than others. For example, hydrogen is the
581 most effective moderator of neutron energy (Fabryka-Martin, 1988), and thus
582 the amount of water in a sample can strongly affect the magnitude of the
583 low-energy neutron flux and consequently influence the production of ^{36}Cl
584 through the low-energy pathway. The importance of water was evaluated
585 theoretically by Dep et al. (1994) and experimentally substantiated by Dunai
586 et al. (2014), indicating that the presence of hydrogen can significantly influ-
587 ence production. There is some evidence to indicate that the water content
588 of the surrounding landscape may also affect the low-energy neutron flux
589 (Zreda et al., 2008). The sensitivity of sample age to water in the current
590 calculator is included in the sensitivity study in Section 5.2.

591 Chlorine-36 dating requires compositional parameters that most cosmo-
592 genic nuclides do not. The code allows for the input of both "mineral target"
593 and "bulk-rock" compositions. The bulk-rock analysis permits the calcula-
594 tion of the neutron-transport parameters. If a mineral separate has been used

for the analysis, the target-element concentrations (comprehensively, K, Ca, Ti, Fe, and Cl) are also needed for the sample on which the measurement was performed. The bulk-rock composition includes data on trace-elements, such as boron and uranium, that are needed for the appropriate calculation of neutron-absorption properties of the rock and radiogenic subtraction. For samples with low Cl content and high concentrations of K and/or Ca, the full range of trace element analyses may be superfluous. Given a complete analysis of a rock sample, CRONUScalc calculates the percentage of the production originating from low-energy neutron absorption by Cl, spallation on Ca and K, and muons. This can be used to determine whether chemical analysis of elements that modulate the low-energy neutron flux are needed for every sample.

Isotope Dilution Mass Spectrometry (IDMS) is a standard method for highly accurate elemental and isotopic analysis. In cosmogenic-nuclide applications it is commonly used for analysis of ^{36}Cl and elemental Cl. The process includes adding a “spike” of known isotope ratio that has been enriched in one of the stable chlorine isotopes, either ^{35}Cl or ^{37}Cl . In either case, the ratios of $^{36}\text{Cl}/^{35}\text{Cl}$ and $^{35}\text{Cl}/^{37}\text{Cl}$ are measured by the accelerator mass spectrometer. The stable chloride concentration and the ^{36}Cl concentration of the rock can both be back-calculated using the ratios from the accelerator and the recorded spike and sample masses from sample preparation. The process is described in detail in Desilets et al. (2006a).

When using IDMS for chlorine, there is a correlation between the uncertainties in stable chloride concentration and the uncertainties on ^{36}Cl concentration because they both depend on the same isotope ratios. In order to produce the correct uncertainties from raw laboratory results, a set of additional codes were created to handle this calculation. This code is external to the main CRONUScalc program, but is distributed with the code. It is designed to assist the user in calculating the correct concentrations of ^{36}Cl and Cl and correctly assigning their uncertainties for samples reported as $^{36}\text{Cl}/\text{total Cl}$ and $^{35}\text{Cl}/^{37}\text{Cl}$ by AMS. A linearized uncertainty method was used to calculate the stable chlorine concentration (`spiketoconc.m`). However, the traditional error propagation does not work for low-Cl samples due to the non-linear response in this range, so uncertainties are calculated using a Monte Carlo method (`spiketoconcmc.m`). In the Monte Carlo code, the uncertainty in the stable chlorine concentration is calculated 10,000 times using the nominal inputs (spike mass, sample mass, spike concentration, etc.) and a random uncertainty. The random quantity added to the nominal value

of the parameter is normally distributed with a mean of 0 and standard deviation equal to the uncertainty in the parameter. For samples with high chlorine concentrations, the Monte Carlo result is essentially the same as the linearized approximations; however, at low chlorine concentrations, the uncertainties can be a significant percentage of the total concentration (>90%).

3.3. Carbon-14

Production of in-situ cosmogenic ^{14}C is primarily from the spallation of oxygen, but also other elements including Mg, Al, and Si (Dunai, 2010). Unlike ^{10}Be , muons contribute significantly (15-20%) to the cosmogenic production at the surface and increasingly at depth. Quartz is the only mineral phase in which ^{14}C is commonly measured, although it is possible to measure it in other minerals as well (Handwerger et al., 1999; Dunai, 2010). Carbon-14 has a short half-life and therefore reaches secular equilibrium between production and decay relatively quickly ($\sim 25\text{-}30$ kyr) (Lifton et al., 2001). Due to these factors, ^{14}C is well-suited for short-term erosion rate studies using multiple nuclides and young burial-history studies (Dunai, 2010).

In situ ^{14}C is extracted from quartz typically by stepped combustion/ dissolution (e.g. Lifton et al., 2001; Pigati et al., 2010; Goehring et al., 2014) or stepped combustion (Hippe et al., 2014). Reproducibility of intercomparison materials is typically ca. 5% among labs (Jull et al., 2013), but occasional discrepancies on replicate analyses have been as much as 5-10% in the past (Borchers et al. 2015). As a result, in situ ^{14}C production rates have tended to exhibit somewhat greater uncertainties than other nuclides, although the situation is improving as extraction techniques continue to advance.

In CRONUScalc, only the production of ^{14}C in quartz by spallation and by muons is available. This should provide adequate functionality for the majority of ^{14}C users. For information on the ^{14}C production rates used in the calculator, see the CRONUS-Earth spallation production rate calibration paper (Borchers et al., 2015).

3.4. Helium-3

Cosmogenic ^3He is produced primarily by spallation reactions on most elements present in a rock (Mg, Si, Fe), but also through low-energy neutron absorption by lithium (Li) (Dunai et al., 2007). Moderate amounts of Li (50-200 ppm) can cause a significant amount of production to originate from cosmogenic thermal neutrons, affecting neighboring (and potentially Li-free) mineral phases (Dunai et al., 2007). Even in relatively low-Li samples (1

669 ppm), radiogenic production can be important in rocks where the formation
670 age of the rock is much greater than the exposure age of the sample (Lal,
671 1987; Farley et al., 2006; Dunai et al., 2007). There is currently no evidence
672 of significant contribution to production via muon reactions (Kurz, 1986;
673 Dunai, 2010). The most commonly used minerals are pyroxene and olivine,
674 however ^3He has been measured in other mineral phases (e.g. apatite, zircon,
675 biotite, titanite, kyanite, and hornblende) (Amidon & Farley, 2012; Amidon
676 et al., 2009; Amidon & Farley, 2010; Farley et al., 2006; Amidon et al., 2008).

677 When evaluating ^3He data, the inherited (magmatic) component must
678 be subtracted from the measured concentration in order to include only the
679 cosmogenically produced ^3He in the dating. This is done through methods
680 that vary by lab (Kurz, 1986; Cerling, 1990; Blard & Pik, 2008; Blard &
681 Farley, 2008; Williams et al., 2005). The input needed for CRONUScale is the
682 cosmogenic concentration of ^3He in units of atoms per gram. CRONUScale
683 assumes that any corrections for blanks or inherited component have already
684 been performed.

685 Currently, CRONUScale only incorporates spallation production for ^3He .
686 The spallation production rate is currently calibrated from a combined data
687 set consisting of olivine and pyroxene samples from the compilation by Goehring
688 et al. (2010b). The publication includes both official CRONUS data and
689 high-quality external data sets. Individual sites were determined to be either
690 primary or secondary data sets based on quality of the independent age con-
691 trol and other site parameters. For information on the ^3He calibration, see
692 Borchers et al. (2015).

693 Recommended use of the calculator is currently limited to olivine and
694 pyroxene due to the limitations of the calibration data set. For pyroxene
695 and olivine derived from basalt and xenoliths, Li concentrations are typically
696 very low (<5 ppm) so the presence of cosmogenic or radiogenic ^3He from
697 low-energy neutrons should be negligible (Dunai et al., 2007). The lithium
698 low-energy pathway needs to be considered for minerals in rocks that are
699 more evolved than primitive basalts and generally for rocks whose geological
700 age is much larger than the exposure age (Dunai et al., 2007; Lal, 1987).
701 Until this pathway is incorporated into the program, users are cautioned to
702 limit the use to low-Li samples.

703 The calculation of the low-energy production pathway is complicated by
704 the large number of additional parameters that would be needed (e.g. grain
705 size of target minerals, complete major and trace element composition of
706 the host rock, water content) (Dunai et al., 2007). The calculator is already

707 designed to take the mineral phase as an input and a thermal neutron com-
 708 ponent could be added by adapting the low-energy production calculations
 709 already in place for ^{36}Cl . This would increase the applicability of CRONUS-
 710 calc to helium samples with higher Li contents and ultimately allow inclusion
 711 of other mineralogies.

712 4. CRONUScalc Calculators

713 The program written to perform a range of cosmogenic nuclide calcu-
 714 lations is named "CRONUScalc." It is written in the MATLAB program-
 715 ming language, but can also be run under open-source Octave. The pro-
 716 gram is available under the GNU General Public License agreement and can
 717 be accessed and downloaded at: [https://bitbucket.org/cronusearth/](https://bitbucket.org/cronusearth/cronus-calc)
 718 **cronus-calc**. In the repository, users can upload their own files alongside
 719 the main code in order to share new features or functions using CRONUScalc.

720 The program is organized by scaling model, with folders containing code
 721 to perform various calculations. The core functions (Section 4.1) and the
 722 functions common to all nuclides are contained in the **production** folder. Ad-
 723 ditional folders are available for surface sample dating (**surfacecalc**), depth
 724 profile dating (**profilecalc**), and calibration of production rates (**calib**,
 725 **muoncalib**, **pfzero**).

726 4.1. Core Functionality

727 The code is designed to predict concentration at a particular depth for
 728 the specified nuclide. This is done using a function called **predNXX**, where
 729 **XX** represents the desired nuclide (i.e. **predN36** calculates production of
 730 ^{36}Cl). There are a few preliminary code modules necessary to build the in-
 731 puts required for the main code. These include creating constants for physi-
 732 cal parameters (**physpars**), calculating scaling factors (**scalefacsXX**), orga-
 733 nizing the input sample parameters (**sampparsXX**), and computing sample-
 734 dependent parameters that are needed for later calculations (**compparsXX**).
 735 These are not discussed in detail here, but can be found in the Function
 736 Appendix in the Supplementary Materials and will be available online for
 737 download with the code. **PredNXX** uses all this preliminary information in
 738 order to predict concentrations of the nuclide. This is summarized in Figure
 739 3 for the ^{10}Be code.

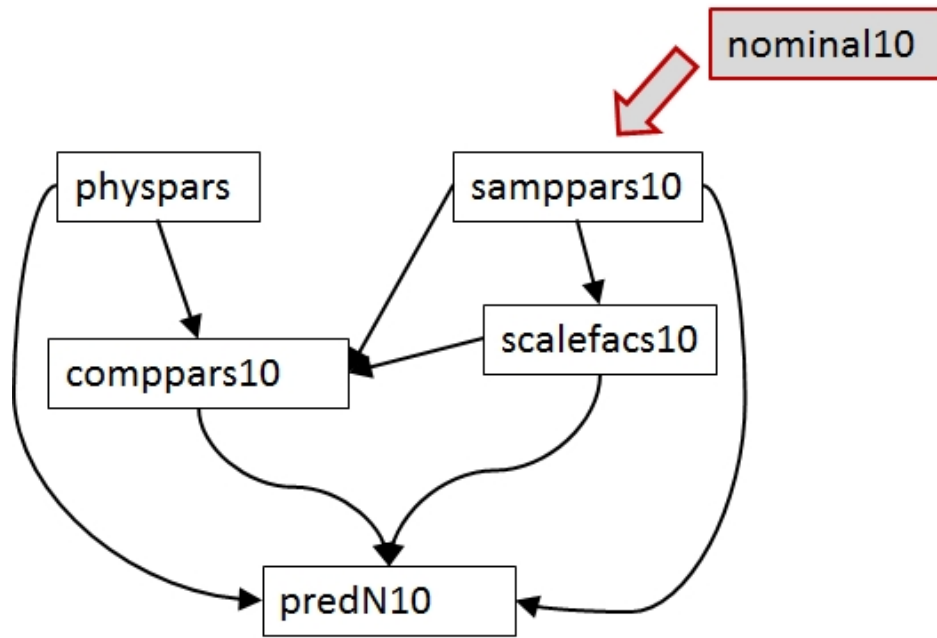


Figure 3: Data flow diagram showing the relationship between different parts of the code for a ^{10}Be sample. Inputs include the nominal inputs (**nominal10**) and the uncertainties on each of those inputs (**uncerts10**, not shown). Other code pieces (**physpars**, **samppars10**, **comppars10**, and **scalefacs10**) set up the correct variables for the upper-level code pieces. **predN10** predicts the concentration for a given age and depth.

740 4.2. Features

741 This program has several differences as compared to previous calculators.
742 The CRONUScalc program is designed to work for all the commonly used
743 nuclides, including ^{10}Be , ^{26}Al , ^3He , ^{36}Cl , and ^{14}C , with ^{21}Ne in testing. The
744 modular nature of the program means that the scaling frameworks are ap-
745 plied in an identical manner to each nuclide, avoiding possible inconsistencies
746 from errors in coding or using two different calculators for cross-nuclide com-
747 parisons. The addition of a new scaling framework by Lifton et al. (2014)
748 allows for a physics-based calculation of the incoming cosmic-ray flux as well
749 as nuclide-dependent scaling frameworks that incorporate the individual nu-
750 clide reaction cross-sections. This calculator has an easy input structure so
751 that samples can be copied from spreadsheets and allows the user to run
752 multiple samples simultaneously. This is one of the only calculators to allow
753 the user to specify uncertainties on all input parameters and propagate those
754 to the resulting exposure age. Finally, this program does not require any pro-
755 prietary software because it can be run on either MATLAB or Octave, the
756 latter being open-source.

757 CRONUScalc is able to calculate production and accumulation for any
758 given sample as well as perform calibrations and calculate surface sample
759 and depth-profile exposure ages. This calculator provides both surface sam-
760 ple and depth-profile dating abilities based on the same underlying code.
761 Included in the surface calculator is the ability to date a single sample at
762 depth. The code does not currently calculate burial ages.

763 Other new features that are not clearly visible in the upper levels of the
764 program are the new integration method and the newly calibrated Heisinger
765 muon production formulation. Some previous calculators relied on analytical
766 solutions to integrate over depth by incorporating a 'thickness correction
767 factor'. In this program, a numerical depth integration is performed, which
768 removes approximations necessary in the analytical solution. This results in
769 a more accurate inventory of accumulated nuclide in the sample as well as
770 the ability to easily modify the code to look at multiple time periods with
771 varying erosion rates. The new muon production is scaled using Lifton et al.
772 (2014), and includes new production rate parameters calibrated from deep
773 profiles for ^{10}Be , ^{26}Al , and ^{36}Cl (for both Ca and K).

774 Finally, although this paper discusses primarily the code behind the pro-
775 gram, there is an online interface for the surface calculator, and other small
776 tools such as the topographic shielding calculator, available to the public
777 with no need to directly manipulate the code (<http://web1.ittc.ku.edu>:

778 8888/). This simplifies the process and makes the technique available to a
779 much broader range of users. Instructions for use of the interface calculators
780 will be maintained online.

781 5. Surface Sample Calculator

782 The Balco et al. (2008) calculator put the Al/Be cosmogenic nuclide com-
783 munity on a consistent platform by providing a reliable tool for consistent
784 ^{10}Be and ^{26}Al exposure age calculations. However, this did not apply to any
785 other nuclides and the code did not allow the user to fully propagate uncer-
786 tainties on all input parameters. CRONUScalc extends this idea to include
787 multi-nuclide capability, full propagation of uncertainties, and the ability to
788 work with single samples at depth.

789 Using the equations given in the previous sections, we can compute the
790 rate of production of a cosmogenic nuclide at any depth within the subsur-
791 face at any point in the past. This production rate varies over time due to
792 time-dependent scaling as well as varying due to changes in depth caused
793 by erosion or aggradation. While the nuclide is accumulating it is also con-
794 tinuing to decay - the radioactive decay rate must be subtracted from the
795 production rate. The time-dependent production rate can be numerically
796 integrated over time in order to predict the concentration of the cosmogenic
797 nuclide at a specific depth after a specified exposure history. By averaging
798 the accumulated production at depths throughout the thickness of a sam-
799 ple, we can predict the average concentration of the cosmogenic nuclide as a
800 function of the exposure age of the sample.

801 5.1. Computing the Exposure Age or Erosion Rate

802 To compute the exposure age of a sample, we begin by checking for sat-
803 uration. This is done by computing the sample-specific saturation concen-
804 tration by predicting the accumulated concentration in the sample assuming
805 an exposure time of at least six half-lives, incorporating time-dependent pro-
806 duction rates and ending in the sample collection year, and using all other
807 user-provided inputs (see Section 3 for a list of inputs). If the measured
808 concentration of the cosmogenic nuclide is close to or exceeds the satura-
809 tion concentration (95% or more), then it is not possible to determine an
810 exposure age for the sample because the sample is effectively saturated. If
811 not, then we use the bisection method to find an age at which the predicted
812 concentration matches the measured concentration of the nuclide. A similar

method is applied in order to determine erosion rate for a sample when either an independent age is supplied or equilibrium with erosion rate can be assumed.

5.2. *Input Uncertainties and Derivatives*

The computed exposure age for a sample depends on a number of sample parameters in addition to the measured nuclide concentration, including its thickness and density, the assumed erosion rate, the assumed atmospheric pressure at the exposure site, etc. For each of these parameters, we compute the derivative of the exposure age with respect to the parameter by finite difference approximation. If the user supplies uncertainties for these parameters, then these derivatives are employed to propagate the uncertainties in the parameters into an uncertainty on the computed exposure age, using first order Taylor series expansion (Bevington & Robinson, 1992).

The code allows for detailed quantification of the uncertainties associated with a sample. The commonly reported uncertainty, that from only the AMS analysis, represents the minimum uncertainty in the age of an unknown sample. There are uncertainties in the other measurements (chemical concentrations, field measurements, etc.), production rates, scaling, and laboratory processing. CRONUScalc allows an uncertainty to be assigned to each of the input parameters, a feature that is unavailable in other single-sample surface exposure age calculators. This idea was addressed in the multi-sample depth-profile calculator using Monte Carlo methods presented by Hidy et al. (2010), but is treated more systematically here using derivatives. In a manner similar to that employed by Balco et al. (2008), CRONUScalc distinguishes between analytical (internal) uncertainty, which is calculated by propagating uncertainties on every input parameter in `uncertsXX`, and total uncertainty, which is calculated by fully propagating the production-rate uncertainty and combining it with the analytical uncertainty. Although statistically-based uncertainties on the production rate parameters were not possible (Borchers et al., 2015), an alternative method to assess the uncertainty on this parameter was used in an attempt to provide a more complete uncertainty estimate.

The uncertainty associated with the nuclide production rate (i.e., the uncertainty added to the analytical uncertainty to give the total uncertainty) is based on a comparison of the deviations of the calculated ages for the secondary data set with the independent (and assumed correct) ages for those samples. In essence, the uncertainty associated with the production rate was increased until the average standard deviation of the calculated ages matched

850 the spread of the deviations of the calculated ages from the independent
 851 ages. This empirical estimation of the additional uncertainty assumes that
 852 the residuals between the calculated ages and the independent ages averages
 853 zero and has a normal distribution. The actual distribution of residuals only
 854 marginally supports this assumption. The most significant sources of the
 855 additional uncertainty (not accounted for by the assigned analytical or other
 856 measurement uncertainties) are the following four. (1) Underestimation of
 857 the actual analytical uncertainties. Jull et al. (2013) have presented evidence
 858 that laboratory-reported uncertainties generally underestimate, sometimes
 859 by significant amounts, the actual spread of the cosmogenic-nuclide analytical
 860 data. (2) Errors in spatial scaling. Regularities in the residuals as a function
 861 of location and elevation give clues that even the best scaling models may
 862 not completely predict the global pattern of nuclide production (Phillips
 863 et al., 2015). (3) Errors in the assigned independent ages for the primary
 864 calibration data sites. Although sites with very well constrained ages were
 865 used, they cannot be guaranteed to all be completely accurate. (4) Site-
 866 specific factors. Assumptions regarding factors such as snow cover, lack of
 867 covering deposits in the past, and erosion rates may have been in error for
 868 some sites. In summary, the additional uncertainty that is specified for the
 869 production-rate terms incorporates all sources of uncertainty or bias that are
 870 not included in the reported laboratory analytical uncertainties. It reflects
 871 the likelihood that a single, randomly selected, high-quality, cosmogenic-
 872 nuclide age will correspond to an independently determined exposure age for
 873 the same material, empirically assessed using the CRONUS-Earth secondary
 874 data sets. Full details on the method, assumptions, and the uncertainty
 875 sources incorporated into the production-rate uncertainty are discussed in
 876 Phillips et al. (2015).

877 It is important to differentiate between the two reported uncertainty types
 878 (analytical and total). For example, analytical uncertainties alone are likely
 879 to underestimate realistic uncertainties when comparing to other dating tech-
 880 niques or comparing widely geographically or temporally separated cosmo-
 881 genic samples. On the other hand, the total uncertainty may overestimate
 882 uncertainties when comparing between groups of samples from a single ge-
 883 ographic location where uncertainties are not independent (e.g. in certain
 884 cases, production rate uncertainties are unimportant for relative chronology
 885 at a single site) (Dunai, 2010; Balco et al., 2008). Comparisons between nu-
 886 clides can be complicated by the use of different calibration data sets and
 887 production models, so it may be necessary to use the external uncertainties

888 to compare between samples from different nuclides located at the same site
889 (Balco et al., 2008). Both uncertainties are reported, allowing the user to
890 determine which is the most appropriate for each particular study. The user
891 is encouraged to report all inputs, including assigned uncertainties, and note
892 the type of uncertainty used in analyses.

893 A sensitivity analysis was performed in order to determine which inputs
894 and their uncertainties have a significant effect on the sample exposure age.
895 The results of the sensitivity analysis are presented in Figure 4. It is based
896 on a random selection of the ^{36}Cl primary and secondary calibration samples
897 (see Marrero (2012) for details), although similar results were seen for ^{10}Be
898 samples. The results presented are merely intended to be representative and
899 will vary from sample to sample. Sensitivities are only given for standard
900 environmental parameters that are applicable for all nuclides. Chlorine-36
901 uncertainties are also sensitive to sample chemical composition. This topic
902 is dealt with separately for ^{36}Cl in Marrero et al. (2015).

903 Based on this sensitivity analysis, there are some uncertainties that are in-
904 significant. For example, realistic uncertainties on longitude and latitude are
905 not important when compared to uncertainties on the concentration. Other
906 variables that realistically do not require uncertainties include shielding and
907 year collected. On the other hand, relatively large and potentially biased
908 uncertainties are expected on parameters such as erosion rate and water con-
909 tent because these require estimation and some knowledge of the site and
910 can rarely be precisely calculated.

911 When comparing different nuclide results, especially those from different
912 sites, all uncertainties must be assessed in a consistent manner. The un-
913 certainties from scaling and methodological considerations become primary
914 issues. The interlaboratory studies associated with the CRONUS project
915 (Jull et al., 2011, 2013; Vermeesch et al., 2012; Schaefer et al., 2014; Blard
916 et al., 2014) were designed to address the uncertainties that arise solely from
917 different processing techniques and accelerator measurements. These results
918 were used to incorporate realistic uncertainty into the nuclide concentrations
919 used for calibration (see Phillips et al. 2015 for details).

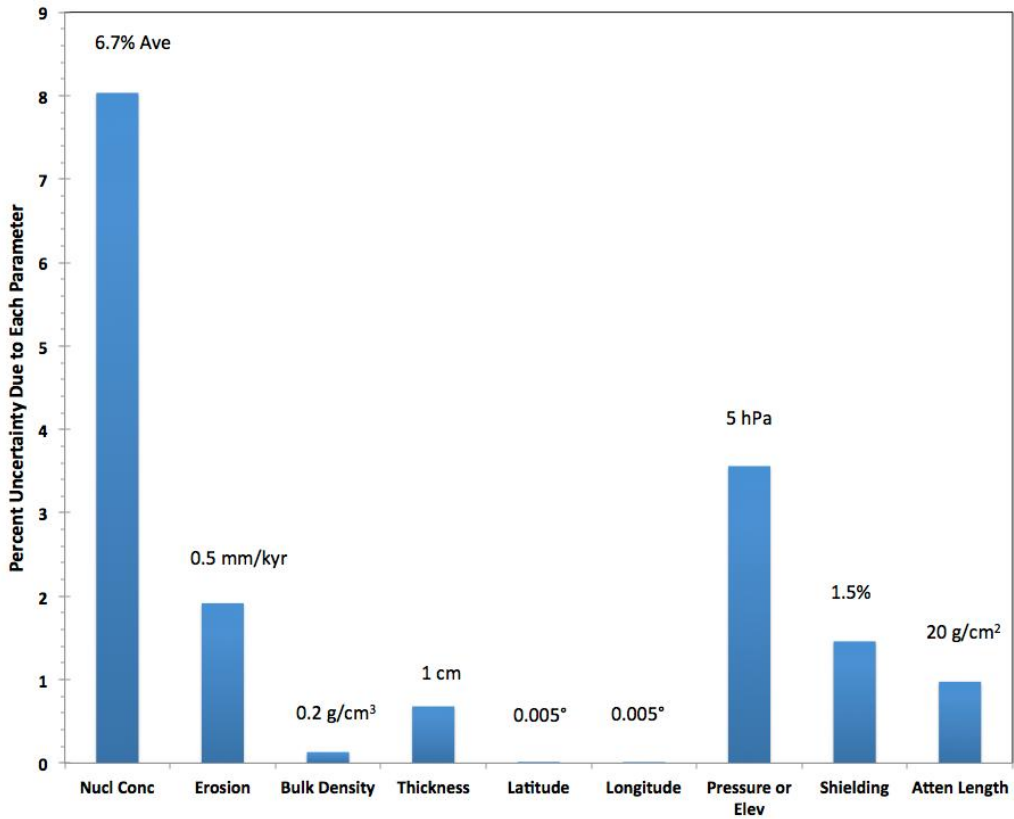


Figure 4: Amount of uncertainty (as a percentage of the final calculated age) contributed by conservative uncertainties assigned to individual sample parameters. The analysis presents the average of the propagated uncertainties for 15 primary and secondary ³⁶Cl calibration samples (Marrero, 2012; Marrero et al., 2015). The values above each bar give the assigned uncertainty in the parameter.

920 6. Depth-Profile Calculator

921 The depth profile calculation is formulated as a Bayesian inverse prob-
922 lem. This approach has several advantages. First, unlike using a classical
923 statistics approach to parameter estimation, the Bayesian approach treats un-
924 known parameters as random variables. Doing so allows the resulting fitted
925 parameters to be reported as expected values, accompanied by a probability
926 distribution. Second, this approach allows the user to submit prior infor-
927 mation or expert knowledge, influencing the solution. The selection of an
928 informative prior distribution for parameters will strongly bias the resulting
929 posterior distribution. Therefore the responsible user is obligated to report
930 the effect that different priors have on their solution. Third, from a compu-
931 tational standpoint, the method presented in this section is not susceptible
932 to the convergence failures that iterative line-search solvers can encounter in
933 certain cases.

934 The inputs to the depth profile code are the same as those for the surface
935 calculator, with several additional parameters required only for the profile
936 calculation. The new parameters include maximum and minimum values
937 for erosion rate, exposure age, and inheritance. In addition to erosion rate
938 bounds, a value for total maximum erosion (positive or negative) can be used
939 to additionally constrain the final results, which can be useful as total erosion
940 can sometimes be easier to determine in the field. Some parameters common
941 to the surface calculator, such as depth to top of sample and attenuation
942 length, become more significant in the depth profiles than they were for
943 surface samples. These parameters are both user inputs (i.e. the calculator
944 assumes these are known parameters), although the uncertainties in these
945 parameters have the potential to increase the uncertainty in the calculated
946 age of the profile. One initial sensitivity test on a profile indicated that
947 reasonable uncertainties on attenuation length were relatively insignificant,
948 although reasonable uncertainties on bulk density measurements could result
949 in up to 5% change in nominal age. For details on other parameters, see the
950 sensitivity study results in Section 5.2. The depth profile calculator does not
951 explicitly incorporate uncertainties on input parameters other than nuclide
952 concentration.

953 Performing the depth profile calculation requires the simultaneous esti-
954 mation of three parameters: age (t), erosion rate (ϵ), and inheritance (inh).
955 The steps necessary for the computations are summarized here. First, an
956 evenly spaced, 3-dimensional grid over the parameters of age, erosion rate,

957 and inheritance is created. Note that the spacing is consistent only within
 958 each dimension and the parameter range for each is specified by the user.
 959 Second, the misfit χ^2 value is calculated at each node (each age, erosion rate,
 960 and inheritance point) using Equation 10.

$$\chi_{t,\epsilon,inh}^2 = \sum_i^n \left(\frac{x_i}{\sigma_i} \right)^2 \quad (10)$$

where

$$x_i = ConcPred_{t,\epsilon,inh} - ConcMeas_i$$

961 Next, the approximated χ^2 hyper-surface is transformed into a likelihood
 962 surface using Equation 11.

$$L(\mathbf{x}|\boldsymbol{\theta}) = \prod_{i=1}^n \left(\frac{1}{\sqrt{2\pi}\sigma_i} \right) \cdot \exp \left(-\frac{\chi_{t,\epsilon,inh}^2}{2} \right). \quad (11)$$

963 Finally, to calculate the joint posterior from the likelihood we use Bayes
 964 rule, shown in Equation 12.

$$p(\boldsymbol{\theta}|\mathbf{x}) = \frac{L(\mathbf{x}|\boldsymbol{\theta})\pi(\boldsymbol{\theta})}{\int_{-\infty}^{\infty} L(\mathbf{x}|\boldsymbol{\theta})\pi(\boldsymbol{\theta})d\boldsymbol{\theta}}, \quad (12)$$

965 where $\pi(\boldsymbol{\theta})$ is the joint prior distribution set by the user on the following
 966 parameters: age, erosion rate, and inheritance. A trapezoidal integration
 967 scheme is used to calculate the denominator, leaving the joint posterior den-
 968 sity, $p(\boldsymbol{\theta}|\mathbf{x})$.

969 When assigning uncertainties to a solution, it is important to determine
 970 if any multiple interactions exist between erosion rate, age, and inheritance.
 971 To display these interactions, the calculator produces 3 pairwise 2-D contour
 972 plots of the joint posterior distribution with contours of 68% and 95% regions
 973 of probability. For example, integrating $p(\boldsymbol{\theta}|\mathbf{x})$ over inheritance gives the
 974 probability distribution given by $p(\epsilon, t|\mathbf{x})$. This effectively marginalizes the
 975 joint posterior over one of the three parameters. An example of the resulting
 976 2-D contour plots are shown in Figure 5, along with the predicted versus
 977 measured profile plot.

978 The best-fitting solution is the lowest chi-squared value over the entire
 979 three-dimensional grid. This is called the maximum a posterior (MAP) solu-
 980 tion. In the 2-D pairwise plots, the MAP solution and the apparent 2-D best-
 981 fit solution do not always coincide due to the interaction of the parameters

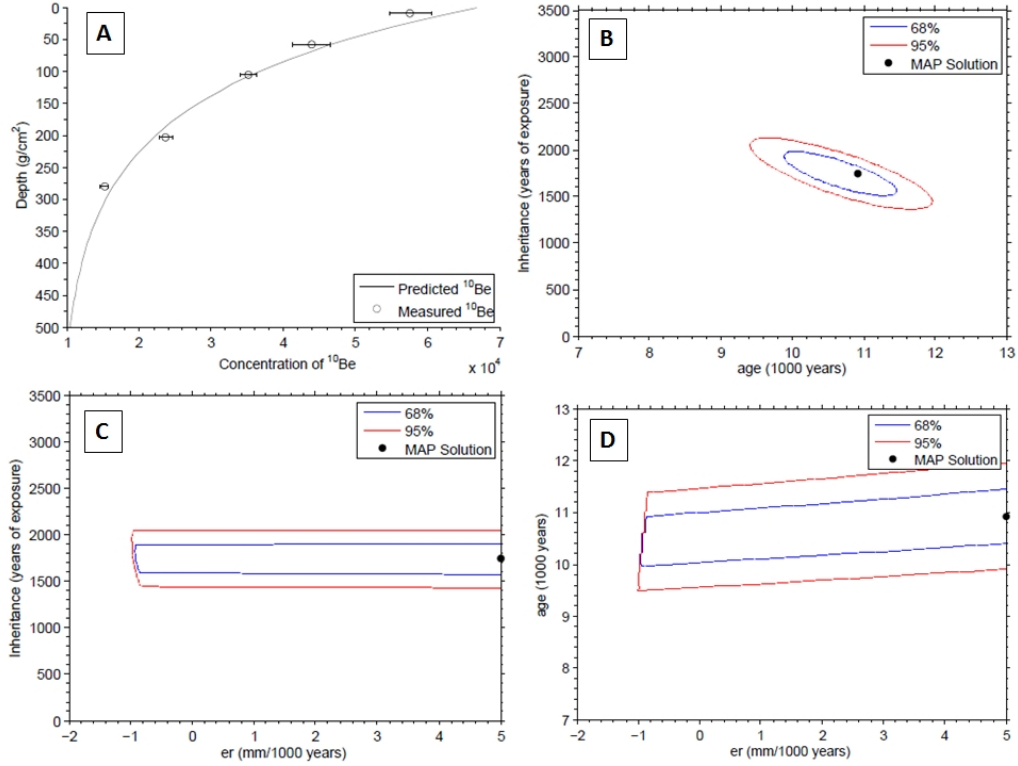


Figure 5: Example of the profile and pairwise plots produced by the depth profile calculator. The example is a ^{10}Be profile published by Goehring et al. (2010a) and used as an example in Aumer (2010). MAP solution is the best-fitting 3-D solution. 68% and 95% contours are the confidence intervals for the chi-squared values. (A) Figure shows the measured data and the predicted profile with depth; (B) Figure shows the confidence intervals for the plot of the inheritance and age; (C) Figure shows the confidence intervals for the plot of the inheritance and erosion rate; (D) Figure shows the confidence intervals for the plot of the age and erosion rate.

with the third dimension. The direct calculation of posterior probabilities eliminates the need for Monte Carlo, as was used by Hidy et al. (2010). In contrast to Hidy et al. (2010), this code also computes a posterior probability distribution, allowing for an assessment of the probability of the resulting age being within particular age bounds. While there are other mathematical methods or spreadsheets available for calculating depth profiles (Braucher et al., 2009; Hein et al., 2009; Schaller et al., 2009), we discuss CRONUScalc in relation to Hidy et al. (2010) because of its similar format and explicit distribution for use as a depth profile calculator.

7. Discussion and Cautions

7.1. Atmosphere and Elevation Relationships

The relevant inputs are both elevation and atmospheric pressure for the sample. Elevation, which is more easily measured and can be found on a topographic map even after sampling, is the traditional input for these codes. The additional pressure input is necessary because it is the more accurate measure of the sample location in the atmosphere. If the user does not specify a site pressure, the online user interface automatically estimates the pressure using the ERA40 Reanalysis data set. The ERA40 reanalysis is a synthesis of comprehensive global observations and analyses over a 45 year period, as discussed in Uppala et al. (2005). This pressure calculation module is available with the code and pressure is a required input (not automatically calculated) within the raw code. The production-rate calibrations were all done using pressures determined from ERA40 and it is recommended that this conversion be used unless there is a specific reason to suspect a significantly different pressure relationship over the sample exposure period. ERA40 functions in Antarctica so no separate atmosphere relationship is required.

Uncertainty in the sample pressure is a significant contributor to sample uncertainty. The uncertainty associated with the pressure based on uncertainties in elevation is quite small (<1 hPa for elevation uncertainties up to 15 m). This results in only a small amount of total uncertainty on the sample age ($<1\%$). A more realistic source of uncertainty associated with pressure is the difference between the current pressure and the average pressure over the exposure time of the sample. The pressure history through time is not a factor that can be accurately calculated. Our assumption that the pressure has remained relatively constant through time adds additional uncertainty. Based on the maximum differences observed between corresponding grid cells

in the NCEP/NCAR and ERA40 (Uppala et al., 2005) reanalyses, we have added a conservative uncertainty of 5 hPa to the CRONUS-Earth samples to account for this and this addition results in uncertainties of 2-5% for most samples.

7.2. Uncertainties Due to Scaling

Not all scaling frameworks fit the calibration data equally well. For each nuclide, a single data set was used to produce a production rate for each combination of scaling framework and nuclide. Because of its favorable analytical precision and accuracy, relative simplicity of its production mechanisms, and the large number of analyses, the nuclide best suited to evaluating the adequacy of scaling frameworks is ^{10}Be . This topic is discussed more fully in Borchers et al. (2015) and Phillips et al. (2015), but is briefly summarized here. The average absolute error, by site averages, of the predicted vs. measured concentrations for the neutron-monitor-based scaling methods (Lifton, Dunai, Desilets) varied from 15.7 to 18.1 %. Those for the scaling methods based on more direct measures of spallation reactions (Lal-based and LSD) varied from 8.5 to 9.7 %. The second group is clearly more accurate. Although within this group the LSD-flux based model gave the best fit, the differences are so small that no clear preference is evident. In the following discussion of scaling uncertainty, the neutron-monitor based scaling methods were not considered due to the poor fit to the data set.

A second issue associated with scaling is the uncertainty from determining the scaling factor at a new location that is not a calibration site. The basis for estimating this contribution to the total age uncertainty is weak. The best basis available is found by comparing the fit of the primary CRONUS-Earth ^{10}Be data set (to which the production rates were calibrated) to the fit of the secondary data set (which is independent of the primary data set) in Borchers et al. (2015). For the best-fitting scaling framework (LSD-flux based), the average absolute error was 5.4 % for the primary data set, compared to 8.5 % for the secondary data set. The difference between these two uncertainties could be interpreted to suggest that error in predicting scaling at non-calibration sites contributes about 3 % to the total age uncertainty. However, the following factors must be considered: (1) the source of the variability cannot be assigned strictly to scaling and could, in fact, be due to other issues, such as the production rate calibration (2) samples were assigned to the secondary data set because they were weaker than those in the primary one due to factors such as less well constrained exposure histories,

and therefore there are undoubtedly factors in addition to scaling uncertainty contributing to their larger scatter, and (3) error in scaling clearly contributes to the 5 % scatter obtained for the primary data set, giving a contribution to the uncertainty from scaling that is not accounted for in the comparison. Factors (1) and (2) contribute to a decrease in scaling uncertainty while factor (3) contributes to an increase in uncertainty. The balance between these cannot at present be known, but likely the error in scaling, on average, contributes significantly less than 3 % to the total age uncertainty.

The original CRONUS-Earth production-rate calibration was not able to calculate statistical uncertainties on the production rate parameters (Borchers et al., 2015). Instead, the CRONUS-Earth Project employed an empirical method for estimating production-rate uncertainty based on the secondary data set (Phillips et al., 2015). The empirical method does not break out the contribution to that uncertainty from scaling alone, but it does incorporate that source of uncertainty into the production-rate uncertainty recommendation. This inferred production-rate uncertainty is propagated along with other parameter uncertainties in CRONUScalc to provide the total uncertainty on a sample. Additional insight into scaling uncertainty can be obtained from the "leave-one-out cross-validation exercise" in Borchers et al. (2015).

7.3. Limitations of CRONUScalc

Although CRONUScalc has new capabilities not previously available in other calculators, there are some limitations to the program. CRONUScalc was designed to provide the most accurate model for a wide range of samples, meaning that approximations were avoided in most cases unless they could be shown not to increase uncertainty or error. The incorporation of more physics-based modeling into the program has substantially increased the calculation time for each sample. The online interface minimizes this problem by emailing the user with results, original inputs, and all data necessary to recreate the graphs prior to their deletion from the server so no further contact with the website is required. While samples are running, the user is provided a link that shows current progress on submitted samples. The use of email avoids browser timeout problems and decreases the dependence on a reliable internet connection. Emails and all sample data, except usage statistics on general location and nuclide, are automatically deleted every 24 hours from the server to protect anonymity.

The current program only process one scaling model at a time for each sample. While it can be instructive to examine outputs from multiple scaling models, the addition of two new scaling models, for a total of seven, makes this time-prohibitive given the new framework. By allowing multiple samples to be submitted simultaneously, users can still perform the scaling comparisons by submitting samples more than once with a different scaling model selection.

7.4. *Expected Changes in Performance Due to New Scientific Content*

Comparisons to results from other similar cosmogenic calculators do not serve to show that CRONUScalc functions as expected for two main reasons. First, differences in the calibration data sets used by each program lead to very different results. Second, CRONUScalc has a different set of assumptions, parameters, and implementations than other programs, leading to results that differ by more than rounding error from the other programs, even when identical calibration data sets are used. Fundamentally, differences between the various programs are expected and this makes it impossible to prove the accuracy of CRONUScalc by obtaining the same results as those produced by other programs. The main differences are discussed later in this section.

However, in the very simplest case where there is only spallogenic production and we assume a time-independent production rate, it is possible to compare results from our code with the analytical solution given by equation 4.11 in Dunai (2010). The ^3He calculator was tested against analytically predicted concentrations for sample ages varying between 0.001-7000 ka and erosion rates of 0, 1, and 10 mm/kyr. At the highest erosion rates, the oldest samples were saturated. For all unsaturated samples, the differences between the analytically produced concentrations and the CRONUScalc solution were less than 0.005%, with most several orders of magnitude smaller. The results are presented in Appendix D. The agreement between CRONUScalc and analytical solutions indicates that the CRONUScalc numerical integration performs well over a variety of erosion rates and ages. CRONUScalc results for other nuclides cannot be directly compared to analytical solutions due to the complex muon model and other new features, but the underlying age integration will be as accurate as demonstrated for ^3He , because of the shared numerical integration code.

The section below highlights the new scientific content in CRONUScalc that is most likely to contribute to differences in performance when compared

to other similar calculators. This section does not discuss the features of other calculators, but reiterates the key scientific content present in CRONUScalc and the situations that may yield major differences.

The addition of a new pair of scaling models (flux-based and nuclide-dependent models from Lifton et al. (2014)) provides a flexible, physics-based model for scaling production rates, but it also introduces the possibility for differences that vary by location and elevation when compared to results from other scaling models available in CRONUScalc or other programs. Lifton et al. (2014) contains a more detailed discussion of differences between resulting scaling factors, including the effects of solar modulation and the updated geomagnetic history.

CRONUScalc allows the user to specify an uncertainty for each parameter in the input. In addition to those analytical uncertainties, the production-rate uncertainty is propagated through to produce a total uncertainty for each sample (see Sections 5.2 and 7.2). Although the added flexibility to include an uncertainty on each input is useful, especially for older samples where fewer parameters were accurately reported, the CRONUScalc uncertainties will likely be different from those reported by other available calculators.

CRONUScalc muon production follows the Heisinger model, but uses CRONUS-Earth calibrated muon production rates (Fig 1 in Phillips et al., 2015) and is scaled using Lifton et al. (2014). In the fast muon formulation, CRONUScalc assumes a value for α (the parameter that defines how the cross-section scales with muon energy) equals one (see Section 2.1.3). This has a small effect on the elevation dependence on production rates when compared to models that use the value of α equal to 0.75 reported in the original paper (Heisinger et al., 2002b).

As discussed in Section 3.4, CRONUScalc only includes the spallation pathway for ^3He production calculations. This may be appropriate for some samples, but users are cautioned to check the composition of samples to confirm that this is true. Even moderate to low concentrations of lithium (Li) in a sample can potentially contribute significant production via thermal neutron production, which is not accounted for in this model.

CRONUScalc calculations for ^{36}Cl are more complex than for other nuclides, introducing more possible contributors to differences when comparing results from other programs. CRONUScalc includes ^{36}Cl production from both fast and slow muons. For samples with higher chlorine concentrations, an updated set of elemental parameters (Table 1) may make significant differences in calculated sample results, especially for samples high in boron.

1166 Finally, CRONUScalc assumes that the ^{36}Cl concentration is in equilibrium
1167 with the radiogenic and nucleogenic production rates in order to calculate the
1168 radiogenic subtraction (only significant for samples high in Th or U). This
1169 is unimportant for rocks with very old formation ages, but it is less clear
1170 whether this is appropriate for rocks where the formation age is equal to the
1171 exposure age. For example, based on available data for basalts, it is unclear
1172 if radiogenic production should begin at eruption or if it is in equilibrium
1173 prior to that time. Additional research is required to distinguish between
1174 these two models.

1175 8. Conclusion

1176 The CRONUScalc program, designed to predict sample concentrations at
1177 a particular depth, is intended to be versatile and work quickly for the largest
1178 number of possible applications without sacrificing accuracy. The program's
1179 abilities to calculate surface and depth-profile exposure ages, calculate ero-
1180 sion rates, and perform calibrations offer many options to the user. However,
1181 the code is available under a public license, so advanced users can modify the
1182 code to work for unusual scenarios. The new features, including a new scal-
1183 ing framework that performs nuclide-dependent scaling and a more accurate
1184 integration method, provide an internally consistent option for cosmogenic
1185 nuclide modeling. While the code can be adapted to many different functions,
1186 an online calculator with a simple interface has been designed for surface and
1187 depth-profile exposure age calculation (<http://web1.ittc.ku.edu:8888/>)
1188 in order to remove any necessity of a Matlab license or knowledge of coding
1189 and make the code easily available to the general cosmogenic isotope user
1190 community.

1191 All the previous CRONUScalc versions will be archived in the online code
1192 repository and available for calculation of previously published results.

1193 9. Acknowledgments

1194 This research was supported by the National Science Foundation through
1195 the Cosmic-Ray-Produced Nuclides on Earth (CRONUS-Earth) Project through
1196 grant EAR-0345949. We would like to thank all the members of the CRONUS-
1197 Earth and CRONUS-EU Projects for their input. This manuscript benefited
1198 from three thorough reviews by P. Vermeesch, R. Braucher, and an anony-
1199 mous reviewer.

1200 Appendix A. Production Models

1201 The sections below describe the fundamental theory behind the code.
1202 This appendix is provided to summarize the systematics of the program
1203 without referring back to numerous previous publications. See the main text
1204 for summaries of the key developments of CRONUScale.

1205 *Appendix A.1. Cosmic Rays*

1206 Cosmic rays originate primarily from Milky Way galaxy supernova, but
1207 also from the sun and other energetic phenomena (Dunai, 2010; Gaisser,
1208 1990; Gosse & Phillips, 2001; Pigati & Lifton, 2004). The main cosmogenic
1209 particles reaching the atmosphere are protons (87% of the cosmic-ray flux),
1210 with a smaller portion of the cosmic-ray flux composed of alpha particles
1211 (12%) and other heavier nuclei (1%) (Dunai, 2010). These incoming particles
1212 have a wide range of energies, with typical energies ranging from a few MeV
1213 to 10^{20} eV (Dunai, 2010). Over long periods (10 Ma), the integrated cosmic-
1214 ray flux has been shown to be constant (to within 10%) when averaged over
1215 500 kyr timescales, with the uncertainties becoming larger (up to 30% or
1216 more) when averaged over timescales of hundreds of thousands to millions of
1217 years (Wieler et al., 2013).

1218 As incoming cosmic-ray particles reach the top of the atmosphere, they
1219 interact with the earth's magnetic field. Only particles with sufficiently high
1220 energy and the correct trajectory will actually reach the earth's surface. This
1221 control on the magnitude of the cosmic-ray flux is quantified by means of the
1222 cutoff rigidity. The rigidity of a particle (R) is given by Equation A.1. In
1223 the equation for rigidity, p is the particle momentum, c is the speed of light,
1224 and e is the particle charge.

$$R = pc/e \tag{A.1}$$

1225 The vertical cutoff rigidity, the minimum threshold for the particle energy
1226 necessary in order to penetrate the field on a path normal to the magnetic
1227 field, is the standard parameter used to organize the effect of the dipole
1228 field on the cosmic-ray flux as a function of location on the surface of the
1229 earth (Dunai, 2010; Gosse & Phillips, 2001; Lifton et al., 2005). The cutoff
1230 rigidities are related to geomagnetic latitude, having very low values near the
1231 poles ($>58^\circ$ at sea level), resulting in admittance of essentially all cosmic-ray
1232 particles, and increasing towards the equator (Lifton et al., 2005).

The complexity of the paths of cosmic-ray particles due to interaction of looping trajectories with the solid earth results in an area where there are both allowed and forbidden trajectories in an alternating pattern known as the penumbra (Hillas, 1972). In order to determine where this region is and its effects on the cosmic-ray flux, reverse particle tracking (or trajectory tracing) can be performed for particles within 20 km of the earth’s surface to determine the effective vertical cutoff rigidity of a location (Shea & Smart, 1983; Dunai, 2010; Lifton et al., 2005). The effective vertical cutoff rigidity is used in scaling frameworks to parameterize the cosmic-ray flux of a site. Additional detail is given in the scaling section, Appendix C.

After the primary cosmic-ray particles reach the top of the atmosphere, they interact with atmospheric particles and create a cascade of secondary particles. As these secondary particles are produced and the cascade propagates through the atmosphere, several trends are apparent: the energy of the secondary particles decreases, the total flux of particles decreases, and the flux becomes dominated by neutrons due to the ionization losses of protons (Dunai, 2010). During these reactions, muons are also produced due to secondary reactions by energetic incoming particles high in the atmosphere (Eidelman, 2004). Unlike the hadronic component of the flux, the muonic flux increases and then reaches a plateau as the cascade moves down through the atmosphere because muons do not interact as strongly as neutrons and are lost very slowly through ionization (Gaisser, 1990). At the earth’s surface, muons comprise the majority of the particles in the incoming cosmic-ray flux (Lal, 1988), but contribute less to surface production than do neutrons due to their lower propensity for nuclear interactions.

The energy spectrum of the neutrons that reach the earth’s surface determines the rate of cosmogenic-nuclide-producing reactions. The neutrons, which compose 98% of the nucleonic flux at the earth’s surface (Dunai, 2010), have peaks in the energy spectrum at 100 MeV, 1-10 MeV, and <1 eV (Dunai, 2010; Goldhagen et al., 2002). The neutron energies discussed in this paper will be categorized as high (>10 MeV), fast (0.1 to 10 MeV), epithermal (0.5 eV to 0.1 MeV), and thermal (<0.5 eV). While these conventions follow other papers in the field (Gosse & Phillips, 2001; Schimmelpfennig et al., 2008), there are no consistent classifications and the actual energies associated with the categories may vary in other publications (Dunai, 2010).

Appendix B. Production Equations

The production equations for CRONUScalc are provided here. The details below are discussed in general terms for production of any nuclide, designated 'k', while details specific to a particular nuclide are discussed in later sections.

Appendix B.1. Spallation

Spallation refers to the emission of a large number of nucleons (relative to the original mass of the nucleus) when an atomic nucleus interacts closely with a high-energy particle. In some cases (e.g. ^3He) a cosmogenic nuclide of interest may be one of the ejected particles. More commonly, (e.g. ^{26}Al), it is the remainder of the target nucleus. Cosmogenic-nuclide production from spallation follows a well-established exponential decrease with depth. At the surface, spallation is typically the dominant production mechanism. All the nuclides discussed in this paper are produced through at least one spallation pathway. The formula for the instantaneous production rate from spallation ($P_{s,m}$) is (Gosse & Phillips, 2001; Schimmelpennig et al., 2008):

$$P_{s,m}(Z) = S_T \sum S_{el,s} P_{m,k}(0) C_k \exp\left(-\frac{Z}{\Lambda_{f,e}}\right), \quad (\text{B.1})$$

where $P_{m,k}$ is the sea-level, high-latitude production rate of species m by spallation of element k (atoms $\text{g}^{-1} \text{a}^{-1}$; S_T is the topographic shielding factor (unitless); $S_{el,s}$ is the geographical scaling factor for spallation reactions for the particular reaction of interest, including temporal variation in the production rate due to fluctuations in the geomagnetic field or solar magnetic field (unitless); C_k is the concentration of the element k (atoms $\text{g}^{-1} \text{a}^{-1}$); and $\Lambda_{f,e}$ is the effective attenuation length for fast neutrons (g cm^{-2}). The production is summed for all target elements k that produce nuclide m to give the total spallation production rate.

Appendix B.1.1. Attenuation Length

The particle attenuation length is the passage length through a medium required to attenuate the original intensity of a collimated beam of particles by a factor of e^{-1} (Gosse & Phillips, 2001). This value varies depending on the type of particle (proton, neutron, muon) and the associated energy level (fast, thermal, epithermal, etc.). For neutrons, the main factor is the energy level, with higher energy particles penetrating further into the subsurface

than lower energy particles. The apparent attenuation length, $\lambda_{f,e}$, is the flux-weighted integral of the particle attenuation length over the entire sky.

The apparent attenuation length is an important parameter because it quantifies the depth distribution of the production by neutron spallation. The apparent attenuation length is defined with respect to a flat sample with no topographic shielding. When the apparent attenuation length is adjusted to account for the dip of the sample surface and any topographic shielding, the result is the effective attenuation length, $\Lambda_{f,e}$. The effective attenuation length is the parameter that should be used in calculations pertaining to production from a particular sample.

Typically, as the topographic shielding increases, the effective attenuation length increases (Dunne et al., 1999). The spectrum of neutron energy varies depending on the azimuth angle. The highest energy cosmic rays are vertically incident upon the sample and the flux is dominated by these rays (Dorman et al., 1999, in Dunai 2010). As the incident angle decreases going from vertical to horizontal, the intensity of the cosmic rays decreases due to the longer transport paths through the atmosphere (Dunai, 2010). The equation for this change in intensity is shown in Equation B.2. As topography typically blocks out only cosmic rays near the horizon, the average energy of the remaining cosmic rays increases. The sample dip also contributes to a change in the effective attenuation length and shielding, as described in Dunne et al. (1999).

$$I(\theta) = I_0 \sin^m \theta, \quad (\text{B.2})$$

where I is the particle beam intensity and θ is the inclination angle from the vertical. The exponent m , which is dependent on both energy and particle type, has been experimentally fit in several papers with significant differences in the results, as discussed in Dunai (2010). The most commonly cited value is 2.3 ± 0.5 from Nishiizumi et al. (1989), although Lal (1958) also gives a value of 2.3. However, Conversi and Rothwell (1954), cited by Lal, give a value of 2.1 ± 0.3 for 60 MeV nucleons (2.6 ± 0.2 for 750 MeV). In other studies, values of 2.5 ± 0.5 to 3.0 ± 0.5 (Barford and Davis, 1952), 3.5 ± 1.2 (Heidbreder et al., 1971), and 2.65 (Masarik et al., 2000) have also been provided. Using Sato's PARMA model, the exponent is ca. 2.8 for neutrons (calculated for neutrons >100 MeV, at solar minimum, 200 m altitude, $R_c = 0$ GV). The corresponding result for protons of similar energies is on the order of 3-3.5. Comparisons between this value and those reported in other

studies must be considered with carefully because the energy ranges of the measurements are potentially quite different. Muons follow a similar trend, although the exponent in this case is 2 (Eidelman, 2004) or about 3.5 using the PARMA model. CRONUScalc does not use this formulation, however, and calculates the apparent attenuation length by interpolating from the values in Table 4, which were obtained using the spreadsheet published with Sato et al. (2008) and the adjustments described in the text.

The effective attenuation length depends on the sample location as well as the dip and shielding. The values for real samples vary from approximately 150-190 g/cm², which overlaps with the measured values for the apparent attenuation length, Λ_f , for fast nucleonic particles, which range from 121 to >170 g/cm² (Dunai, 2000). Some recent studies for Be use a value of 177 (Farber et al., 2008; Schimmelpfennig et al., 2008). In addition to the dependence of the effective attenuation length on topographic shielding, it also depends on site cutoff rigidity and elevation, due to the dependence of the particle penetration length on particle energy. Samples from lower elevation and lower latitude will have longer attenuation lengths because of the increasing hardness of the neutron energy spectrum.

The attenuation-length model in CRONUScalc is based on atmospheric attenuation lengths calculated from the PARMA model of Sato et al. (2008). These are adjusted upward by 11.1% to account for systematic differences between atmospheric and lithospheric attenuation. See Section 2.4 for the complete derivation of the CRONUScalc attenuation length model. The data for the comparison of synthetic sample ages using different attenuation length models are presented here (B.6).

Appendix B.2. Epithermal Neutrons

Low-energy cosmogenic nuclide production, including that from thermal and epithermal neutrons, does not follow a simple exponential pattern with depth due to the atmosphere-ground interface effects. Due to the large cross-section of nitrogen for absorption of low-energy neutrons, the flux of cosmogenic thermal and epithermal neutrons in equilibrium with air is much less than that in equilibrium with rock. Low-energy neutrons produced in the upper ~50 cm of rock therefore tend to diffuse upward out of the rock and into the atmosphere, resulting in a reduction of the flux as the rock surface is approached (see Figure B.6). Phillips et al. (2001) analytically solved the neutron-flux differential equation across the land/atmosphere interface to

Erosion (mm/kyr)	Be conc (at/g)	153 g/cm ² Age (ka)	170 g/cm ² Age (ka)
0	73513	20.0	20.0
0	360327	100.0	100.0
0	1029138	300.0	300.0
1	72154	20.0	20.0
1	328482	100.0	99.1
1	789962	300.0	290.8
2.5	70156	20.0	19.9
2.5	287378	100.0	97.6
2.5	558968	300.0	272.2
5	66974	20.0	19.8
5	233598	100.0	94.7
5	354648	300.0	230.2
10	61176	20.0	19.6
10	163166	100.0	86.9
10	195499	300.0	156.6

Table B.6: Summary of comparison of exposure ages using two different attenuation lengths for a variety of erosion rates. Sample parameters assumed in the calculations for CRONUScalc were: 40 deg latitude, 0 deg longitude, 0 m elevation, thickness of 0.001 cm, shielding of 1, density of 2.65 g/cm³, collection date of 2014 AD.

1371 obtain the equations below. These, in turn, were combined with the formu-
 1372 lations for muon-induced neutron production by Gosse and Phillips (2001)
 1373 to obtain the complete equations for epithermal production.

1374 The general form for the equation for the production of the cosmogenic
 1375 nuclide of interest from epithermal neutrons is shown in Equation B.3. The
 1376 epithermal neutron attenuation length ($\Lambda_{eth,ss}$, Equation B.4) accounts for
 1377 both moderation and absorption of epithermal neutrons and parameterizes
 1378 the effective depth of penetration of the epithermal neutron flux (Gosse &
 1379 Phillips, 2001).

$$P_{eth,ss,m} = \frac{f_{eth,ss,m}}{\Lambda_{eth,ss}} \Phi_{eth,ss,total}(Z)(1 - p(E_{th})_{ss}), \quad (B.3)$$

1380 where $f_{eth,ss,m}$ is the fraction of epithermal neutrons absorbed that are taken
 1381 up by target element k to produce nuclide m (eqn E.15); $\Phi_{eth,ss,total}$ is the
 1382 epithermal neutron flux (eqn B.8).

$$\Lambda_{eth,ss} = [\bar{\xi}_{bulk}(I_{eff,ss} + \Sigma_{sc,ss})]^{-1} = \Sigma_{eth,ss}^{-1}, \quad (B.4)$$

1383 where $\bar{\xi}_{bulk}$ is the average macroscopic log decrement energy loss per neutron
 1384 collision in the subsurface (eqn E.28); $I_{eff,ss}$ is the macroscopic resonance
 1385 integral for absorption of epithermal neutrons in the subsurface (eqn E.16);
 1386 $\Sigma_{sc,ss}$ is the macroscopic neutron scattering cross-section in the subsurface
 1387 (Equation E.27).

1388 The distribution of epithermal neutrons in the subsurface can be de-
 1389 scribed by Equation B.5. The epithermal neutrons are assumed to be pro-
 1390 duced entirely from the moderation of both spallation and evaporation neu-
 1391 trons and are assumed to be in equilibrium with the high-energy flux (Gosse
 1392 & Phillips, 2001).

$$D_{eth,ss} \frac{d^2 \Phi_{eth,ss}}{dZ^2} = \frac{\Phi_{eth,ss}}{\Lambda_{eth,ss}} - R_{eth,ss} P_f, \quad (B.5)$$

1393 where the diffusion coefficient for epithermal neutrons in the subsurface
 1394 ($D_{eth,ss}$) is defined in Equation E.9, with the corresponding parameter in
 1395 the atmosphere, defined in Equation E.10; $R_{eth,ss}$ is the normalization factor
 1396 for the epithermal neutron production rate (eqn E.25); P_f is the production
 1397 rate of epithermal neutrons from fast neutrons, with the value at the surface
 1398 represented as $P_f(0)$, which is a calibrated production rate parameter for
 1399 ^{36}Cl .

1400 The observed subsurface, epithermal neutron flux, $\Phi_{eth,ss}$, at a particular
 1401 point is the balance of exponential production with depth against the loss of
 1402 neutrons through diffusion at the rock/air interface as well as loss through
 1403 absorption and moderation. The hypothetical epithermal neutron flux in the
 1404 subsurface assuming that there is no boundary (all material is the same as
 1405 the subsurface) is indicated by $\Phi_{eth,ss}^*$ and is given in Equation B.6. The
 1406 difference between the hypothetical equilibrium flux in the air ($\Phi_{eth,a}^*$) and
 1407 the hypothetical equilibrium flux in the subsurface ($\Phi_{eth,ss}^*$) is $\Delta\Phi_{eth,ss}^*$. The
 1408 physical cause of the difference between the fluxes (no interface vs interface)
 1409 is the effect of diffusion. This is shown mathematically in Equation B.7 and
 1410 graphically in Figure B.6.

$$\Phi_{eth,ss}^*(Z) = P_f(0) \frac{R_{eth,ss}}{\Sigma_{eth,ss} - D_{eth,ss}/\Lambda_{f,e}^2} \quad (B.6)$$

$$\Delta\Phi_{eth,ss}^* = \Phi_{eth,a}^* - \Phi_{eth,ss}^* = -\Delta\Phi_{eth,a}^* \quad (B.7)$$

1411 For the purposes of this initial solution, photodisintegration and other
 1412 neutron-producing interactions are neglected. The diffusion-like behavior of
 1413 low-energy neutrons means that the diffusion equation, in addition to the
 1414 production equations, must be solved in order to predict the appropriate
 1415 amount of cosmogenic nuclide from this type of production. The solution to
 1416 the coupled differential equations (originally solved in Phillips et al. (2001))
 1417 yields Equation B.8.

$$\Phi_{eth,ss} = S_T S_{el,s} \Phi_{eth,ss}^* \exp\left(-\frac{Z}{\Lambda_{f,e}}\right) + (F\Delta\Phi)_{eth,ss}^* \exp\left(-\frac{|Z|}{L_{eth,ss}}\right), \quad (B.8)$$

1418 where the physical meaning of the $(F\Delta\Phi)_{eth,ss}^*$ term (Equation B.9) is
 1419 the difference between the actual observed flux (with an interface present)
 1420 and the flux that would be observed at the surface ($Z=0$) if all materials
 1421 were the same as those in the subsurface. This can also be formulated for
 1422 the air, as seen in Equation E.12. $L_{eth,ss}$ (eqn E.19) is the diffusion length
 1423 for epithermal neutrons in the subsurface and the corresponding parameter
 1424 in the atmosphere, $L_{eth,a}$, is shown in Equation E.20. $S_{el,s}$ is the scaling
 1425 factor for spallation reactions, as the flux is derived from the high-energy
 1426 component.

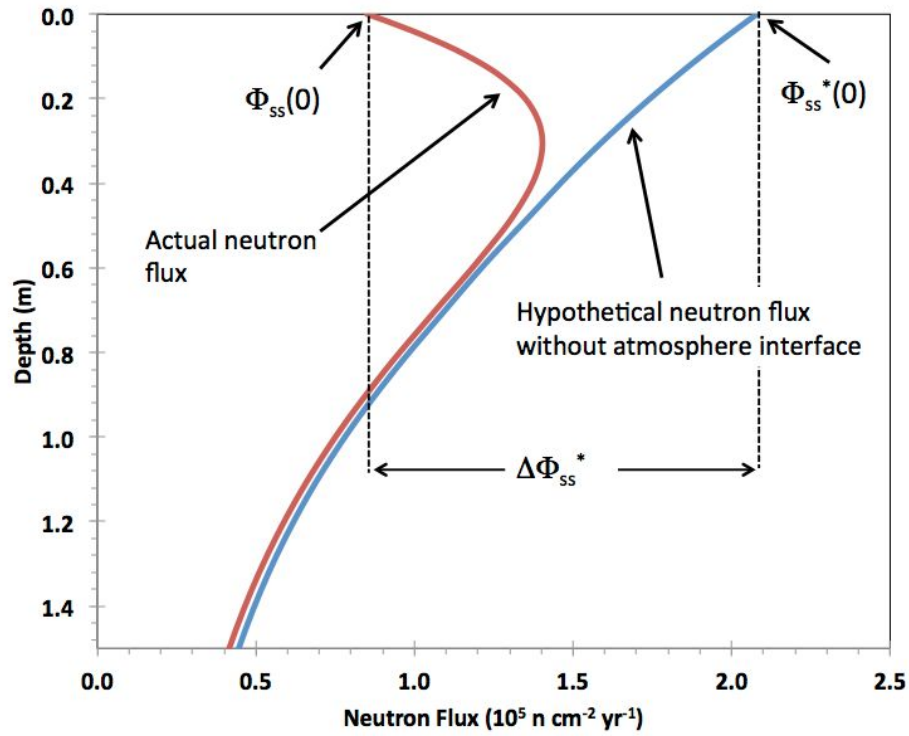


Figure B.6: Thermal-neutron flux profile calculated for standard granite from Fabryka-Martin (1988), illustrating the physical meaning of the terms $\Phi_{ss}(0)$, $\Phi_{ss}^*(0)$, and $\Delta\Phi_{ss}^*$. The physical meaning is equivalent for both thermal and epithermal neutron fluxes.

$$(F\Delta\Phi)_{eth,ss}^* = \frac{\Delta\Phi_{eth,ss}^* D_{eth,a}/L_{eth,a} - \Delta\Phi_{eth,a}^{**} D_{eth,ss}/\Lambda_{f,e}}{D_{eth,a}/L_{eth,a} + D_{eth,ss}/L_{eth,ss}}, \quad (B.9)$$

1427 where:

$$\Delta\Phi_{eth,a}^{**} = \Delta\Phi_{eth,ss}^* - \frac{D_{eth,a}}{D_{eth,ss}} \Phi_{eth,a}^* \quad (B.10)$$

1428 *Appendix B.3. Thermal Neutrons*

1429 Cosmogenic thermal neutrons are produced as a result of the moderation
 1430 of cosmogenic epithermal neutrons (in other words, cosmogenic epithermal
 1431 neutrons lose energy through collisions with atoms in the subsurface and end
 1432 up as thermal neutrons, having only the ambient energy imparted by ordi-
 1433 nary thermal vibration). The source term for thermal-neutron production is
 1434 therefore the epithermal neutron distribution with depth. The production
 1435 equations for thermal neutron pathways are analogous to those for epither-
 1436 mal neutrons. In the general production equation, the form is very similar
 1437 with many parameters being replaced by ones specific for thermal neutrons
 1438 instead of epithermal neutrons. The production rate ($P_{th,m}$) for thermal
 1439 neutrons is shown in Equation B.11 (Gosse & Phillips, 2001).

$$P_{th,ss,m} = \frac{f_{th,ss,m}}{\Lambda_{th,ss}} \Phi_{th,ss,total}(Z), \quad (B.11)$$

1440 where $f_{th,ss,m}$ is the fraction of absorbed thermal neutrons that are taken
 1441 up by element k to produce nuclide m (eqn E.32); $\Phi_{th,ss,total}$ is the thermal
 1442 neutron flux (eqn B.13); and $\Lambda_{th,ss}$ is the effective thermal neutron attenua-
 1443 tion length (Equation E.33).

1444 The distribution for thermal neutrons in the subsurface (Equation B.12)
 1445 is also similar to that of epithermal neutrons, except that the thermal neutron
 1446 source is assumed to be only neutrons moderated from the epithermal energy
 1447 range.

$$D_{th,ss} \frac{d^2 \Phi_{th,ss}}{dZ^2} = \frac{\Phi_{th,ss}}{\Lambda_{th,ss}} - R_{th,ss} \frac{p(E_{th})_a}{\Lambda_{eth,ss}} [\Phi_{eth,ss}^* \exp(-\frac{Z}{\Lambda_{f,e}}) + (F\Delta\Phi)_{eth,ss}^* \exp(-\frac{|Z|}{L_{eth,ss}})], \quad (B.12)$$

1448 where $D_{th,ss}$ (Equation E.29) is the diffusion coefficient for thermal neu-
 1449 trons; $R_{th,ss}$ is the ratio of thermal neutron production in the rock to that in
 1450 the atmosphere (Equation E.38). The term $p(E_{th})_a$ is the resonance escape
 1451 probability of a neutron from the epithermal energy range in the atmosphere
 1452 (Equation E.24), with the corresponding subsurface term shown in Equation
 1453 E.23.

1454 The equations described above can be solved for the thermal neutron
 1455 flux using the same boundary conditions assumed in the epithermal problem.
 1456 The thermal neutron flux, discounting muon-induced neutrons, is shown in
 1457 Equation B.13.

$$\begin{aligned} \Phi_{th,ss} = S_T S_{el,s} \Phi_{th,ss}^* \exp\left(-\frac{Z}{\Lambda_{f,e}}\right) + (\mathcal{F} \Delta \Phi)_{eth,ss}^* \exp\left(-\frac{|Z|}{L_{eth,ss}}\right) \\ + (\mathcal{F} \Delta \Phi)_{th,ss}^* \exp\left(-\frac{|Z|}{L_{th,ss}}\right) \end{aligned} \quad (B.13)$$

1458 where:

$$\Phi_{th,ss}^* = \frac{p(E_{th})_a R_{th,ss} \Phi_{eth,ss}^*}{\Lambda_{eth,ss} (\Sigma_{th,ss} - \frac{D_{th,ss}}{\Lambda_{eth,ss}^2})} \quad (B.14)$$

$$(\mathcal{F} \Delta \Phi)_{eth,ss}^* = \frac{p(E_{th})_a R_{th,ss} (F \Delta \Phi)_{eth,ss}^*}{\Lambda_{eth,ss} (\Sigma_{th,ss} - D_{th,ss}/L_{eth,ss}^2)} \quad (B.15)$$

$$\begin{aligned} (\mathcal{F} \Delta \Phi)_{th,ss}^* = [D_{th,a} \left(\frac{\Phi_{th,a}^*}{\Lambda_{f,e}} - \frac{(\mathcal{F} \Delta \Phi)_{eth,a}^*}{L_{eth,a}} \right) \\ - D_{th} \left(\frac{\Phi_{th,ss}^*}{\Lambda_{f,e}} - \frac{(\mathcal{F} \Delta \Phi)_{eth,ss}^*}{L_{eth,ss}} \right) \\ + \frac{D_{th,a}}{L_{th,a}} (\Delta \Phi_{th,ss}^* + \Delta (\mathcal{F} \Delta \Phi)_{eth,ss}^*)] / \left(\frac{D_{th,ss}}{L_{th,ss}} + \frac{D_{th,a}}{L_{th,a}} \right) \end{aligned} \quad (B.16)$$

1459 In Equation B.16, additional parameters of $\Delta \Phi_{th,ss}^*$ and $\Delta (\mathcal{F} \Delta \Phi)_{eth,ss}^*$
 1460 are described in Equations E.31 and E.4, respectively. $S_{el,s}$ is the scaling
 1461 factor for spallation reactions.

1462 *Appendix B.4. Muons*

1463 Muons are unstable, charged subatomic particles with a mass of about 207
 1464 times that of an electron and a mean life of about 2.2 s. They are produced by

decay of charged pions and K mesons, which in turn result from the interaction of high-energy cosmic-ray protons with matter in the atmosphere and the solid earth (Lal & Peters, 1967). Cosmic-ray muons possess a wide spectrum of energies and the nature of their interaction with atomic nuclei depends strongly on energy. Lower energy (“slow”) muons can participate in muon-capture reactions. The muon-capture reactions can release neutrons that later participate in neutron-capture reactions. Higher energy (“fast”) muons can produce nuclear transmutations through inelastic scattering reactions, including both primary scattering reactions by the muons themselves and secondary ones by hadrons and photons released as a result of the primary muon interaction. The hadrons released include neutrons, and neutrons are also produced by gamma rays from muon-induced bremsstrahlung reactions (emission of electromagnetic radiation from an atomic nucleus stimulated by deflection of an energetic charged particle passing close to the nucleus). The energetic bremsstrahlung gamma rays can produce neutrons if they participate in (γ, n) reactions with the nuclei of other atoms. These neutrons also can later participate in neutron-absorption reactions. Muons can thus induce the production of the nuclides modeled by CRONUScalc by means of a wide variety of reactions (Charalambus, 1971; Fabryka-Martin, 1988; Gaisser, 1990; Heisinger et al., 2002a,b).

Although the cosmic-ray muon flux is larger than the hadron flux at the earth’s surface, the rate of interaction is much lower. The muonic component of the cosmic radiation is thus much more penetrating than the hadronic component. The slow component of the muon flux tends to be lost more rapidly due to muon-capture reactions and thus, although the magnitude of the flux decreases with depth below the earth’s surface, the average energy increases. Whereas the hadron flux is important for cosmogenic-nuclide production down to about $1,000 \text{ g cm}^{-2}$, the slow-muon flux is important down to about $2,500 \text{ g cm}^{-2}$ and nuclides produced by the fast-muon flux are detectable down to $10,000 \text{ g cm}^{-2}$. The penetration of muons producing cosmogenic nuclides is often characterized by an attenuation length employed in an exponential depth-dependent equation (e.g., Braucher et al. 2013), but due to the continuous hardening of the muon energy spectrum with depth, the muon flux does not have an exponential dependence on depth and the apparent attenuation length will increase as the depth of the measurements increases.

Muon contributions to total production are typically small at the surface, but become predominant at depths exceeding $\sim 1,000 \text{ g cm}^{-2}$. Accurate

1503 calculation of muogenic production is thus important for sampling sites with
1504 large erosion rates or depth profiles. Accurate muon production formulations
1505 are also necessary for depth profiles deeper than about 3 m (Stone et al., 1998;
1506 Granger & Smith, 2000), where the simultaneous evaluation of spallogenic
1507 and muogenic fractions offers the opportunity to uniquely determine both
1508 age and erosion rate (Braucher et al., 2009).

1509 The original CRONUS-Earth calculator of Balco et al. (2008) imple-
1510 mented the Heisinger et al. (2002a,b) muon model as an improvement over
1511 the more empirical formulation in Stone et al. (1998). However, soon after
1512 Heisinger’s publications, Braucher et al. (2003) used a deep core to provide
1513 evidence that the parameters specified by Heisinger et al. (2002a,b) overes-
1514 timated actual ^{10}Be production by fast muons by approximately a factor of
1515 two. This was supported by additional profile data measured by Braucher
1516 et al. (2011) and by Kim & Englert (2004), as well as reanalysis of previ-
1517 ously published deep profile data by Braucher et al. (2013). This result has
1518 been confirmed by a deep profile drilled in a very low-erosion environment at
1519 Beacons Hills, Antarctica, by the CRONUS-Earth Project (Fig 1 in Phillips
1520 et al., 2015). CRONUScalc employs the Heisinger formulation for calculation
1521 of the subsurface muon flux for all nuclides, but uses calibrated production
1522 parameters obtained by fitting to the Beacon Heights profile data for ^{10}Be
1523 and ^{26}Al .

1524 The muon-flux model of Sato et al. (2008), combined with the previous
1525 Heisinger muon production equations and CRONUS-Earth data, has been
1526 employed to formulate a new hybrid muon production model that combines
1527 aspects of each of these models. The CRONUScalc muon code has been
1528 constructed by N. Lifton by modifying the Heisinger muon implementation
1529 described in Balco et al. (2008) and supplemental materials. The procedure
1530 followed by the code is summarized here along with the relevant equations.

1531 The muon flux at the surface is scaled based on the Lifton-Sato-Dunai
1532 model (Lifton et al., 2014). The scaling is done by computing the omnidirec-
1533 tional muon flux as a function of energy at the site and at a reference location
1534 (SLHL) and dividing the site flux by the reference flux. The CRONUScalc
1535 muon module initially calculates the omnidirectional muon flux at SLHL and
1536 at the site of interest using the PARMA-based equations (Sato et al., 2008).
1537 Energy-dependent scaling factors are then calculated as the ratio of site flux
1538 to that at SLHL for each energy interval. A single scaling factor is similarly
1539 calculated for the stopping muon flux at the surface - we define stopping
1540 muons as those that have ranges less than 10 g/cm^2 (equivalent to ca. 40

1541 MeV energy) (Groom et al., 2001). The vertical muon flux at SLHL is calcu-
 1542 lated using the equation presented in Equation 3 in Heisinger et al. (2002a)
 1543 and shown here as Equation B.17.

$$\phi_{\nu,0}(Z) = \frac{a}{(Z + b)([Z + 1000]^{1.66} + c)} e^{dZ}, \quad (\text{B.17})$$

1544 where the coefficients are as follows: $a = 5.401 \times 10^7$, $b = 21000$, $c =$
 1545 1.567×10^5 , $d = -5.5 \times 10^{-6}$. This formulation is only valid down to 200,000
 1546 g/cm² (~ 750 m depth) and the alternative formulation provided in Balco
 1547 (2008 supplemental material - Eqns. 49-51) should be used for deeper appli-
 1548 cations.

1549 The stopping rate of the vertically incident muons ($R_{\nu,0}(Z)$) is calculated
 1550 by equivalence to the range spectrum of the muons at the surface. Equation
 1551 B.18 shows this calculation.

$$R_{\nu,0}(Z) = \frac{d}{dz}(\phi_{\nu,0}(Z)) = -5.401 \times 10^7 \left[\frac{bc \frac{da}{dz} - a(\frac{db}{dz}c + \frac{dc}{dz}b)}{b^2 c^2} \right], \quad (\text{B.18})$$

1552 where $a = e^{-5.5 \times 10^{-6} z}$; $b = (z + 21000)$; $c = (z + 1000)^{1.66} + 1.567 \times 10^5$;
 1553 $\frac{da}{dz} = -5.5 \times 10^{-6} e^{-5.5 \times 10^{-6} z}$; $\frac{db}{dz} = 1$; $\frac{dc}{dz} = 1.66(z + 1000)^{0.66}$ (Balco et al.,
 1554 2008; Heisinger et al., 2002b).

1555 The vertical muon flux as a function of depth ($\phi_{\nu}(Z)$) at the site is found
 1556 by numerically integrating the stopping rate from infinite depth to the depth
 1557 of interest (Equation B.19).

$$\phi_{\nu}(Z) = \int_Z^{\infty} R_{\nu}(x) dx \quad (\text{B.19})$$

1558 The vertical muon flux is converted to total muon flux at the site following
 1559 Heisinger et al. (2002b) (Equation B.20), but modified to use depth units of
 1560 g/cm² by Balco et al. (2008), as shown in Equation B.21.

$$\phi(Z, \theta) = \phi_{\nu}(Z) \cos^{n(Z)} \theta \quad (\text{B.20})$$

$$n(Z) = 3.21 - 0.297 \ln\left(\frac{Z}{100} + 42\right) + Z * 1.21 \times 10^{-5} \quad (\text{B.21})$$

1561 The total muon flux at a given depth ($\phi_{\mu}(Z)$) is given by Equation B.22.

$$\phi_{\mu}(Z) = \frac{2\pi}{n(Z + \delta Z) + 1} \phi_{\nu}(Z) \quad (\text{B.22})$$

1562 where δZ is the difference between the site of interest and sea level in units
 1563 of g cm^{-2} . The total muon stopping rate as a function of depth ($R(Z)$) can
 1564 be calculated by Equation B.23, following Balco (2007). The total stopping
 1565 rate in muons $\text{g}^{-1} \text{s}^{-1}$ is converted to the negative muon stopping rate by
 1566 accounting for the percentage of all stopped muons that are negative stopped
 1567 muons (44%) and then converting the units to muons $\text{g}^{-1} \text{yr}^{-1}$. In both flux
 1568 calculations (total muon flux and stopped negative muon flux) the values are
 1569 calculated so that the flux is a positive value.

$$R(Z) = \frac{2\pi}{n(Z + \delta Z) + 1} R_{\nu}(Z) - \phi_{\nu}(Z)(-2\pi) * \\ (n(Z + \delta Z) + 1)^2 \left[\frac{-0.297 \times 10^{-2}}{\frac{Z + \delta Z}{100} + 42} + 1.21 \times 10^{-5} \right] \quad (\text{B.23})$$

1570 *Appendix B.4.1. Fast Muon Production*

1571 Production from fast muons as a function of depth is calculated using the
 1572 formulas in Heisinger et al. (2002b), with the general production described
 1573 by Equation B.24.

$$P_{\mu,fast} = S_T \phi_{\mu,total}(Z) \beta(Z) (\bar{E}(Z))^{\alpha} \sigma_0 N_{t,i} \quad (\text{B.24})$$

1574 Where the factor $\beta(Z)$ is a function of the mean total muon energy and
 1575 is shown in Equation B.25 and \bar{E} is defined as the mean muon energy at a
 1576 given depth Z and is shown in Equation B.26. $N_{t,i}$ is the number density of
 1577 the atoms in the target element (in units of at/g). This value is a constant
 1578 for each nuclide unless the composition of the target changes, as it does for
 1579 ^{36}Cl .

$$\beta(Z) = 0.846 - 0.015 \log\left(\frac{Z}{100} + 1\right) + 0.003139 \left(\log\left(\frac{Z}{100} + 1\right)\right)^2 \quad (\text{B.25})$$

$$\bar{E}(Z) = 7.6 + 321.7 * (1 - \exp(-8.059 \times 10^{-6} Z)) + 50.7 (1 - \exp(-5.05 \times 10^{-7} Z)) \quad (\text{B.26})$$

In Heisinger et al. (2002b), the experimentally-determined value of σ_{190} (i.e., the energy-dependent reaction cross-section measured at 190 GeV) was used to calculate the value for σ_0 (the cross-section at 1 GeV) using Equation B.27, which can then be used to calculate the production from muons for a particular nuclide, as shown in Equation B.24. Alpha (α) is an only weakly energy-dependent coefficient that parameterizes the energy dependence of the cross-section on muon energy, with low values indicating a weaker dependence and higher values a stronger dependence. Based on a survey of the literature, Heisinger et al. (2002b) adopted a value of $\alpha \approx 0.75$, but their own experimental evidence supported a value of about 0.93. $^{26}\text{Al}/^{10}\text{Be}$ ratios measured by Kim & Englert (2004) in a profile down to 50,000 g/cm⁻² depth are higher than predicted by Heisinger et al. (2002b), supporting a larger value of α . Experimental results are permissive of values between 0.75 and >1.0 (Heisinger et al., 2002b) so the CRONUS-Earth Project chose a value of $\alpha = 1.0$. By assuming that α equals one, β will also be equal to one. Heisinger et al. (2002b) reported experimentally determined values of σ_{190} for many of the nuclides of interest including ^{26}Al , ^{10}Be , ^{14}C , and ^{36}Cl from calcium. Note that there is no value for ^{36}Cl from potassium. However, application of these values in many cases produced calculated concentrations in excess of what has been measured in deep profiles (Braucher et al., 2011, 2013).

Rather than using parameters estimated from laboratory muon irradiations, the CRONUS-Earth Project has adopted values calibrated from nuclide-concentration profiles at carefully selected sites whenever possible (Fig 1 in Phillips et al., 2015; Borchers et al., 2015; Marrero, 2012). σ_0 was selected as the calibration parameter for the production of nuclides by muon reactions, as discussed in Marrero (2012). This was done mainly for two reasons. First, σ_0 is the only nuclide-dependent parameter in the fast production equation, so it is the logical choice. Second, by directly calibrating the σ_0 parameter, any dependence on the accuracy of the conversion from σ_{190} to σ_0 is eliminated. Equation B.27 was used to calculate initial starting parameters for the σ_0 calibration.

$$\sigma(E) = \sigma_0 E^\alpha, \quad (\text{B.27})$$

where E is the muon energy in GeV.

Appendix B.4.2. Slow Negative Muon Capture Production

Nuclide production by slow negative muon capture ($P_{\mu-}$) is described by Equation B.28, originally from Charalambus (1971) and discussed in detail for ^{36}Cl by Stone et al. (1998). The production rate depends on the stopping rate of negative muons ($\phi_{\mu-}$) as well as the nuclide-dependent factors ($f_{i,C}$, $f_{i,D}$, f_i^*). $f_{i,D}$ is the fraction of muons stopped by element k and absorbed by the nucleus before decay of the muon. $f_{i,C}$, the compound factor, represents the fraction of the muons that are captured by a target element (as opposed to the other elements present) within the bulk rock. The formula for the compound factor is taken from Charalambus (1971) and the values are consistent with those used by Heisinger et al. (2002a). In the case of nuclides measured in a rock of uniform composition, the compound factor is a constant parameter; however, for cases where the lithology, and hence the chemical composition, is spatially variable, the compound factor will also vary. The value for $f_{i,C}$ can be calculated using the formula in Equation E.40 and the values in von Egidy & Hartmann (1982).

$$P_{\mu-} = S_T \phi_{\mu-}(Z) f_{i,C} f_{i,D} f_i^* \quad (\text{B.28})$$

The remaining parameter, f_i^* , the particle emission channel probability, is the probability that the excited nucleus of the target atom will emit the proper particle to result in transformation to the nuclide of interest. Heisinger et al. (2002a) report experimentally determined f_i^* values for the production of ^{26}Al (from Si), ^{10}Be and ^{14}C (from O), and ^{36}Cl (from K and Ca). As for the fast muon production reactions, the parameters of Heisinger et al. (2002a) tend to overestimate nuclide concentrations measured in depth profiles (Fig 1 in Phillips et al., 2015; Braucher et al., 2011), so f_i^* for ^{10}Be , ^{26}Al , ^{36}Cl were calibrated by fitting to the measured CRONUS-Earth profiles (Phillips et al., 2015; Borchers et al., 2015; Marrero, 2012).

Appendix B.4.3. Muon-induced Neutrons

As muons react with atomic nuclei in the subsurface, neutrons are released. These can, in turn, react with other nuclei to produce cosmogenic nuclides of interest. The principal reactions responsible for the production of neutrons are muon capture and (γ , n) reactions resulting from interaction of high-energy gamma from muon-induced bremsstrahlung reactions with the nuclei of atoms in the subsurface. In order to calculate the nuclide production due to these muonic neutrons, it is necessary to know the muon flux as

1647 a function of depth. Due to the capabilities of the muon model, the quan-
 1648 tification of fluxes has improved and they need no longer be approximated
 1649 using a simple exponential equation (Stone et al., 1998), as was previously
 1650 done in most models, including CHLOE (Phillips & Plummer, 1996) and the
 1651 Schimmelpfennig et al. (2009) calculator, but instead are directly calculated
 1652 using Equation B.29. The muon module, described in the previous section, is
 1653 used to calculate the negative muon stopping rate ($\phi_{\mu-}(Z)$) and total muon
 1654 flux ($\phi_{\mu f}(Z)$) terms at a given depth.

$$P_{n,\mu}(Z) = Y_s \phi_{\mu-}(Z) + 5.8 \times 10^{-6} \phi_{\mu f}(Z), \quad (\text{B.29})$$

1655 where Y_s is the average neutron yield per stopped negative muon (Fabryka-
 1656 Martin, 1988).

1657 Near the atmosphere/subsurface interface, muon-induced low-energy neu-
 1658 trons are assumed to follow the same distribution as the spallation-induced
 1659 neutrons. Although the muon-induced neutron flux near the surface is not
 1660 in equilibrium with the production rate due to diffusion, the diffusion is
 1661 occurring based on the total concentration of neutrons at the surface. The
 1662 dominant source of neutrons is spallation reactions, so the muons are assumed
 1663 to follow the same pattern as the spallation-induced neutrons, leading to the
 1664 incorporation of the muogenic neutrons into the epithermal neutron flux as
 1665 shown in Equation B.30.

$$\begin{aligned} \Phi_{\text{eth,ss}}(Z) = & S_T S_{el,s} \Phi_{\text{eth,ss}}^* \exp\left(-\frac{Z}{\Lambda_{f,e}}\right) \\ & + (1 + R_\mu(0) R_{\text{eth,ss}}) (F \Delta \Phi)_{\text{eth,ss}}^* \exp\left(-\frac{Z}{L_{\text{eth,ss}}}\right) \\ & + R_\mu(Z) \Phi_{\text{eth,ss}}^* \end{aligned} \quad (\text{B.30})$$

1666 There are two different values used in the code for the muon-induced
 1667 neutron factor, R_μ . $R_\mu(Z)$ is defined in Equation B.31. In the parts of the
 1668 equation dealing with epithermal neutrons, the surface production rate of
 1669 the muogenic neutrons ($R_\mu(0)$) is used because of the assumption that the
 1670 production follows the same trend as the spallogenic neutrons. For the parts
 1671 of the equation dependent on the attenuation at depth of the muon flux, the
 1672 actual values for $R_\mu(Z)$ are calculated from the muon module and used in
 1673 the equation.

$$R_\mu(Z) = \frac{S_{el,\mu}P_{n,\mu}(Z)}{S_{el,eth}P_f(0)R_{eth}} \quad (\text{B.31})$$

1674 The code calculates the epithermal neutron flux and the subsequent cos-
 1675 mogenic nuclide production by combining the muon-induced neutrons with
 1676 the original epithermal neutron production equation, Equation B.8, to pro-
 1677 duce the total epithermal neutron production for nuclide m, as shown in
 1678 Equation B.32.

$$\begin{aligned} P_{\text{eth,ss,m}}(Z) = & \frac{f_{\text{eth,ss}}\Phi_{\text{eth,ss,total}}}{\Lambda_{\text{eth,ss}}} = \frac{f_{\text{eth,ss}}}{\Lambda_{\text{eth,ss}}} \left\{ \Phi_{\text{eth,ss}}^* \exp\left(-\frac{Z}{\Lambda_{\text{f,e}}}\right) \right. \\ & + (1 + R_\mu(0)R_{\text{eth,ss}})(F\Delta\Phi)_{\text{eth,ss}}^* \exp\left(-\frac{z}{L_{\text{eth,ss}}}\right) \\ & \left. + R_\mu(Z)\Phi_{\text{eth,ss}}^* \right\} \end{aligned} \quad (\text{B.32})$$

1679 Similar considerations for muon-induced neutrons must be made for the
 1680 thermal energy range. Some of the epithermal-range neutrons produced by
 1681 muon interactions lose enough energy to become thermal neutrons. The
 1682 contribution of these muon-induced neutrons to the thermal flux is shown
 1683 in Equation B.33. Once again, the muon-induced neutrons are assumed to
 1684 follow the same trends as the spallogenic neutrons and are scaled appropri-
 1685 ately using only the surface value of $R'_\mu(Z)$ for the spallogenic parts of the
 1686 equation. For the neutron-dependent term, the actual values for each depth
 1687 are calculated. The final equation for the thermal neutron flux is shown in
 1688 Equation B.34.

$$R'_\mu(Z) = \frac{p(E_{th})_a}{p(E_{th})} R_\mu(Z) \quad (\text{B.33})$$

$$\begin{aligned}
\Phi_{th,ss,total} = S_T S_{el,s} & \left\{ \Phi_{th,ss}^* \exp\left(-\frac{Z}{\Lambda_{f,e}}\right) + \right. \\
& (1 + R'_\mu(0))(\Im\Delta\Phi)_{eth,ss}^* \exp\left(-\frac{Z}{L_{eth,ss}}\right) \\
& + (1 + R'_\mu(0)R_{th,ss})(\Im\Delta\Phi)_{th,ss}^* \exp\left(-\frac{Z}{L_{eth,ss}}\right) + \\
& \left. R'_\mu(Z)\Phi_{th,ss}^* \right\} \quad (B.34)
\end{aligned}$$

1689 The total production of cosmogenic nuclide k via thermal neutron path-
 1690 ways is described by combining Equation B.34 with Equation B.11 and yields
 1691 an equation for total production with depth from thermal neutrons, shown
 1692 in Equation B.35.

$$\begin{aligned}
P_{th,ss,m}(Z) = S_T S_{el,s} \frac{f_{th}\Phi_{th,ss,total}}{\Lambda_{th,ss}} = \frac{f_{th}}{\Lambda_{th,ss}} & \left\{ \Phi_{th,ss}^* \exp\left(-\frac{Z}{\Lambda_{f,e}}\right) \right. \\
& + (1 + R'_\mu(0))(\Im\Delta\Phi)_{eth,ss}^* \exp\left(-\frac{Z}{L_{eth,ss}}\right) \\
& + (1 + R'_\mu(0)R_{th})(\Im\Delta\Phi)_{th,ss}^* \exp\left(-\frac{Z}{L_{eth,ss}}\right) \\
& \left. + R'_\mu(Z)\Phi_{th,ss}^* \right\} \quad (B.35)
\end{aligned}$$

1693 *Appendix B.5. Radiogenic Production*

1694 “Radiogenic production” in this context refers to the generation of low-
 1695 energy neutrons by reactions related to the radioactive decay or spontaneous
 1696 fission of U or Th, and the subsequent absorption of those neutrons to pro-
 1697 duce nuclides of interest, principally ^{36}Cl . The radiogenic low-energy neutron
 1698 flux is assumed to be in equilibrium with the concentrations of uranium (U)
 1699 and thorium (Th) in the rock. This component is quantified using measured
 1700 concentrations of U and Th and the method described in Fabryka-Martin
 1701 (1988), which is based on the formulations developed by Feige et al. (1968).
 1702 The uranium and thorium α -decay chain members produce alpha particles

(α) as they decay. The alpha particles react with light nuclei in the rock matrix to produce low-energy neutrons. In turn, the neutrons can react with target elements in the rock in the same way that cosmogenically produced neutrons react to produce nuclides such as ^{36}Cl . The equations for calculating this contribution to the total nuclide inventory within a sample are provided in detail in Fabryka-Martin (1988) and are summarized here.

The radiogenic production of nuclides is given by Equation B.36. The elements with the maximum yield of neutrons due to alpha particle reaction are Be, B, F, and Li. However, due to the low concentration of these elements in most rocks, the largest concentrations of neutrons result from targets with larger matrix concentrations, such as Al, Si, Mg, O, and Na. The concentrations of both O and H are calculated from the oxide measurements performed on the other elements.

$$P_r = P_{eth,r}f_{eth} + P_{th,r}f_{th} \quad (\text{B.36})$$

where P_r is the total radiogenic production from all mechanisms in a particular sample; $P_{eth,r}$ is the total radiogenic epithermal neutron production (Equation B.37); $P_{th,r}$ is the total radiogenic thermal neutron production (Equation B.38).

Although the concentrations of the largest producers of neutrons are the most important elements to quantify, the remaining rock matrix composition must still be quantified in addition to the elements listed above so that all elements can be used to calculate the stopping power of the rock. In particular, there are several elements, such as boron and gadolinium, that have large thermal neutron absorption cross-sections, meaning that they have a large probability of absorbing neutrons (from both radiogenic and cosmic sources) (Fabryka-Martin, 1988). This decreases the actual amount of ^{36}Cl formed within the rock because these other elements intercept the neutrons prior to formation of ^{36}Cl .

$$P_{eth,r} = (P_{n,\alpha} + P_{n,sf})(1 - p(E_{th})), \quad (\text{B.37})$$

$$P_{th,r} = (P_{n,\alpha} + P_{n,sf})(p(E_{th})), \quad (\text{B.38})$$

where $P_{n,\alpha}$ is the production rate of neutrons from alpha particles in neutrons $\text{g}^{-1} \text{yr}^{-1}$ (Equation B.39). $P_{n,sf}$ is the neutron production rate due to the spontaneous fission of ^{238}U and can be calculated as $0.429[\text{U}]$, where $[\text{U}]$ is the concentration of uranium in ppm.

$$P_{n,\alpha} = X[U] + Y[Th], \quad (\text{B.39})$$

where [Th] is the thorium concentration in ppm. X and Y are neutron production factors related to the light isotope composition of the rock matrix and are described in Equations B.40 and B.41, respectively. These were originally described by Feige et al. (1968).

$$X = \frac{\sum k S_k F_{k,bulk} Y_n^U}{\sum k S_k F_{k,bulk}}, \quad (\text{B.40})$$

$$Y = \frac{\sum k S_k F_{k,bulk} Y_n^{Th}}{\sum k S_k F_{k,bulk}}, \quad (\text{B.41})$$

where S_k is the mass stopping power of element k for α -particles of a given energy; Y_n^U and Y_n^{Th} are the neutron yields of element i per ppm U or Th in equilibrium; $F_{k,bulk}$ is the fractional abundance of element k in ppm in the bulk rock.

Appendix C. Scaling

Cosmogenic nuclide scaling applies the physics governing the modulation of the cosmic-ray flux by atmospheric mass and the terrestrial and solar magnetic fields to provide production rates as a function of location and exposure time. Numerous scaling frameworks have been proposed in order to correct for latitude, elevation, atmospheric pressure anomalies, dipole and non-dipole geomagnetic field changes, and solar modulation. For all the details of the scaling frameworks themselves, please see the original papers (cited in Table 2); for details of implementation, please see the descriptions in Balco et al. (2008) and Lifton et al. (2014).

The fundamental correction for elevation and latitude is the key part of each scaling framework. The first scaling framework to implement this was Lal (1991). Eventually, Stone (2000) reformulated the original equations to take atmospheric pressure, instead of elevation, as an input. This is still a commonly cited scaling framework. However, the original, time-independent Lal/Stone scaling (abbreviated as St in the code) does not account for changes in production rate that we know are occurring through time due to fluctuations in the terrestrial and solar magnetic fields.

The production rates of cosmogenic nuclides are a function of the magnetic field strength. As the geomagnetic field of the earth changed in the

past, production rates of the nuclides also changed. This fact has led to the development of scaling frameworks that incorporate the geomagnetic history of the earth. Dunai (2000, 2001a) (Du) , Desilets et al. (2006b); Desilets & Zreda (2003) (De) , and Lifton et al. (2005, 2008) (Li), and Lifton-Sato-Dunai (Lifton et al., 2014) (LSD, herein labeled Sf) have all implemented different models to incorporate the changing magnetic field. Following Balco et al. (2008), we have also provided the time-dependent Lal scaling (Lm, including dipole geomagnetic effects as approximated by Nishiizumi et al. (1989)) in order to differentiate between the geomagnetic effects and other differences in the models.

In CRONUScalc, the geomagnetic history is consistent across all scaling frameworks and is summarized in Table 3. The Lifton et al. (2005) and the more recent model presented in Lifton et al. (2014) (LSD) also incorporate the effects of solar modulation into the scaling framework. For a discussion of the uncertainties associated with geomagnetic models, see Section 2.3.

In each scaling framework that incorporates geomagnetic effects, the appropriate input is cutoff rigidity. However, each scaling framework implements the rigidity cutoff calculations differently (see Schimmelpfennig (2009) for a summary of these differences). See each original scaling reference for the equations for cutoff rigidity. In the program, most of the scaling frameworks are taken directly from Balco et al. (2008) and complete descriptions can be found in the original calculator supplemental material (Balco et al., 2008). For the Sa and Sf models, see the paper by Lifton et al. (2014).

Appendix D. Comparison of CRONUScalc and Analytical Solutions for ^3He

Synthetic ^3He concentrations were predicted using the analytical solution presented in Dunai (2010) for samples undergoing both production and erosion. The CRONUS-Earth calibrated production rate for ST scaling and the erosion rate (Table D.7, column 1) were used to predict the concentration (Table D.7, column 2). The resulting CRONUScalc ages for ST scaling are presented in Table D.7, column 4. The differences in terms of % are provided in the final column of the table. Saturated samples were excluded from comparison. Samples were assumed to be located at SLHL, 0 degrees longitude, and have a density of 2.65 g/cm^3 , shielding of 1, thickness of 0.001 cm , an effective attenuation length of 136 g/cm^2 and were collected in 2014 AD.

Erosion rate (mm/kyr)	Concentration (atoms g ⁻¹)	Actual age (ka)	Calc age (ka)	% Difference (%)
0	118	0.001	0.001	4.6×10^{-7}
0	11821	0.1	0.100	2.0×10^{-7}
0	1182137	10	10.000	-4.9×10^{-7}
0	5910685	50	50.000	5.6×10^{-7}
0	11821370	100	100.000	5.6×10^{-7}
0	23642739	200	200.000	5.6×10^{-7}
0	47285479	400	400.000	5.6×10^{-7}
0	118213696	1000	1000.000	-7.5×10^{-7}
0	236427393	2000	2000.000	-7.5×10^{-7}
0	354641089	3000	3000.000	-9.9×10^{-7}
0	591068482	5000	5000.000	6.0×10^{-7}
0	827495875	7000	7000.000	8.5×10^{-7}
1	11820	0.1	0.100	2.0×10^{-7}
1	1170695	10	10.000	6.8×10^{-7}
1	5631906	50	50.000	5.6×10^{-7}
1	10741040	100	100.000	5.6×10^{-7}
1	19580586	200	200.000	5.6×10^{-7}
1	32842095	400	400.000	5.6×10^{-7}
1	52026941	1000	1000.000	7.5×10^{-7}
1	59441147	2000	2000.000	2.2×10^{-6}
1	60497723	3000	3000.000	8.9×10^{-6}
1	60669750	5000	5000.014	2.8×10^{-4}
1	60673244	7000	7000.662	9.5×10^{-3}
10	11810	0.1	0.100	11.7×10^{-5}
10	1074104	10	10.000	1.7×10^{-5}
10	3776908	50	50.000	2.7×10^{-5}
10	5202694	100	100.000	4.9×10^{-5}
10	5944115	200	200.000	2.0×10^{-4}
10	6064829	400	400.020	4.9×10^{-3}

Table D.7: Summary of comparison between analytical solutions for ³He and CRONUScalc results over a range of erosion rates and exposure ages.

Table E.8: Glossary of terms and equations

Term	Definition
<i>General parameters and subscripts</i>	
bulk	In reference to the bulk rock composition of the sample as opposed to the target (processed) material
C_k	Mass concentration of element k [(g element k) (g material) ⁻¹]
eth	Subscript used to denote the epithermal production pathway, defined as neutrons with energies of 0.5 eV to 0.1 MeV.
h	Atmospheric depth [g cm ⁻²]
k	Subscript used to denote a particular cosmogenic-producing element
m	Subscript used to denote a particular cosmogenic nuclide
m	Molar concentration
μ	Subscript used to denote the muon production pathway
ρ	Density [g cm ⁻³]
s	Subscript used to denote the spallation production pathway
target	In reference to the particular target fraction of the sample, specifically in the case of mineral separates
th	Subscript used to denote the thermal production pathway, defined as neutrons with energies of <0.5 eV.
z	Ordinary linear distance [cm]
Z	Mass depth below the surface [g cm ⁻²] $Z(z) = \int_0^z \rho(z) dz \quad (\text{E.1})$
<i>Cosmic Rays</i>	
c	Speed of light (see eqn A.1)
e	Particle charge (see eqn A.1)
p	Particle momentum (see eqn A.1)
Continued on next page	

Table E.8 – continued from previous page

Term	Definition
R	Rigidity of a particle (see eqn A.1)
S_{el}	Latitude/Elevation scaling coefficient (see scaling scheme section) [<i>unitless</i>]
S_T	Topographic scaling coefficient describing the shielding from surrounding topography [<i>unitless</i>]
θ	Inclination angle from the horizontal [<i>degrees</i>]
z_p	Vertical penetration depth [g cm^{-2}] $z_p = \Lambda_{f,p} \cos \phi \quad (\text{E.2})$

Spallation

$I(\theta)$	Intensity. See eqn B.2. I_0 is the intensity of I for a sample with 0 dip.
$\Lambda_{f,e}$	Effective attenuation length for fast neutrons. See Appendix B.1.1.
$P_{s,m}$	Production rate for spallation of nuclide m. See eqn 1.
$P_{m,k}$	Production rate of nuclide m from target element k. See eqn 1.
θ	Sample dip/inclination as measured from the horizontal. See eqn B.2.

Epithermal Production

\bar{A}_{ss}	Average atomic weight of the bulk rock [g mol^{-1}] $\bar{A}_{ss} = \frac{\sum_k A_k N_{k,ss,bulk}}{\sum_k N_{k,ss,bulk}} \quad (\text{E.3})$
\bar{A}_a	Average atomic weight of the atmosphere; constant = 14.5 [g mol^{-1}] (Phillips & Plummer, 1996)
A_k	Atomic weight of element k [g mol^{-1}]

Continued on next page

Table E.8 – continued from previous page

Term	Definition
$\Delta(\mathcal{F}\Delta\Phi)_{eth,ss}^*$	<p>Difference between $\mathcal{F}\Delta\Phi_{eth}^*$ in the atmosphere ($\mathcal{F}\Delta\Phi_{eth,a}^*$) and the subsurface ($\mathcal{F}\Delta\Phi_{eth,ss}^*$)</p> $\Delta(\mathcal{F}\Delta\Phi)_{eth,ss}^* = (\mathcal{F}\Delta\Phi)_{eth,a}^* - (\mathcal{F}\Delta\Phi)_{eth,ss}^* \quad (E.4)$
$\Delta\Phi_{eth,ss}^*$	<p>Difference between the hypothetical equilibrium epithermal neutron fluxes in atmosphere and rock [neutrons $\text{cm}^{-2} \text{yr}^{-1}$]</p> $\Delta\Phi_{eth,ss}^* = \Phi_{eth,a}^* - \Phi_{eth,ss}^* \quad (E.5)$
$\Delta\Phi_{eth,a}^*$	<p>Difference between the hypothetical equilibrium epithermal neutron fluxes in atmosphere and rock [neutrons $\text{cm}^{-2} \text{yr}^{-1}$]</p> $\Delta\Phi_{eth,a}^* = \Phi_{eth,ss}^* - \Phi_{eth,a}^* \quad (E.6)$
$\Delta\Phi_{eth,ss}^{**}$	<p>Adjusted difference between the hypothetical equilibrium epithermal neutron fluxes in atmosphere and rock. [neutrons $\text{cm}^{-2} \text{yr}^{-1}$]</p> $\Delta\Phi_{eth,ss}^{**} = \Phi_{eth,a}^* - \frac{D_{eth,ss}}{D_{eth,a}} \Phi_{eth,ss}^* \quad (E.7)$
$\Delta\Phi_{eth,a}^{**}$	<p>Adjusted difference between the hypothetical equilibrium epithermal neutron fluxes in atmosphere and rock. [neutrons $\text{cm}^{-2} \text{yr}^{-1}$]</p> $\Delta\Phi_{eth,a}^{**} = \Phi_{eth,ss}^* - \frac{D_{eth,a}}{D_{eth,ss}} \Phi_{eth,a}^* \quad (E.8)$
Continued on next page	

Table E.8 – continued from previous page

Term	Definition
$D_{eth,ss}$	<p>Diffusion coefficient for epithermal neutrons in subsurface [g cm⁻²]</p> $D_{eth,ss} = [3\Sigma_{sc}(1 - \frac{2}{3\bar{A}})]^{-1} \quad (E.9)$
$D_{eth,a}$	<p>Diffusion coefficient for epithermal neutrons in air [g cm⁻²] can be calculated using values of ($\Sigma_{sc,a}$)=0.3773 [cm⁻² g⁻¹] (Phillips & Plummer, 1996).</p> $D_{eth,a} = [3\Sigma_{sc,a}(1 - \frac{2}{3\bar{A}})]^{-1} \quad (E.10)$
$(F\Delta\Phi)_{eth,ss}^*$	<p>Difference between the epithermal neutron flux if there was no boundary ($\Phi_{eth,ss}^*$) and the actual epithermal neutron flux at the atmosphere/subsurface interface (see equation B.9) [neutrons cm⁻² yr⁻¹]</p> $(F\Delta\Phi)_{eth,ss}^* = \frac{\Delta\Phi_{eth,ss}^* D_{eth,a}/L_{eth,a} - \Delta\Phi_{eth,a}^{**} D_{eth,ss}/\Lambda_{f,e}}{D_{eth,a}/L_{eth,a} + D_{eth,ss}/L_{eth,ss}} \quad (E.11)$
$(F\Delta\Phi)_{eth,a}^*$	<p>Difference between $\Phi_{eth,a}^*$ (the epithermal neutron flux in the atmosphere if there was no boundary) and $\Phi_{eth,a}$ (the actual epithermal neutron flux at the atmosphere/subsurface interface) [neutrons cm⁻² yr⁻¹]</p> $(F\Delta\Phi)_{eth,a}^* = \frac{\Delta\Phi_{eth,a}^* D_{eth,ss}/L_{eth,ss} - \Delta\Phi_{eth,a}^{**} D_{eth,ss}/\Lambda_{f,e}}{D_{eth,a}/L_{eth,a} + D_{eth,ss}/L_{eth,ss}} \quad (E.12)$
Continued on next page	

Table E.8 – continued from previous page

Term	Definition
$(\mathcal{F}\Delta\Phi)_{eth,ss}^*$	<p>Describes the difference between $\Phi_{eth,ss}^*$ and the actual flux due to the shape of the epithermal neutron profile across the atmosphere/subsurface interface</p> $(\mathcal{F}\Delta\Phi)_{eth,ss}^* = \frac{p(E_{th})_a R_{th,ss} (F\Delta\Phi)_{eth,ss}^*}{\Lambda_{eth,ss} (\Sigma_{th,ss} - D_{th,ss}/L_{eth,ss}^2)} \quad (E.13)$
$(\mathcal{F}\Delta\Phi)_{eth,a}^*$	<p>Describes the difference between $\Phi_{eth,a}^*$ and the actual flux due to the shape of the epithermal neutron profile across the atmosphere/subsurface interface</p> $(\mathcal{F}\Delta\Phi)_{eth,a}^* = \frac{p(E_{th})_a R_{th,a} (F\Delta\Phi)_{eth,a}^*}{\Lambda_{eth,a} (\Sigma_{th,a} - D_{th,a}/L_{eth,a}^2)} \quad (E.14)$
$f_{eth,m,ss}$	<p>Fraction of total epithermal neutrons absorbed per unit mass of rock that react to produce nuclide m; compositionally dependent [<i>unitless</i>]</p> $f_{eth,m,ss} = \frac{N_{k,ss} I_{a,k}}{I_{eff}} \quad (E.15)$
$\Gamma_{eth,m,ss}$	Total rate of epithermal neutron absorption in subsurface [neutrons g ⁻¹ yr ⁻¹]
$I_{a,k}$	Dilute resonance integral for absorption of epithermal neutrons by element k [$10^{-24} cm^{-2}$]
$I_{eff,ss}$	<p>Effective/macroscopic resonance integral for absorption of epithermal neutrons in subsurface [$cm^{-2} g^{-1}$]</p> $I_{eff} = \sum_k I_{a,k} N_{k,bulk} \quad (E.16)$
Continued on next page	

Table E.8 – continued from previous page

Term	Definition
$\Lambda_{eth,ss}$	Effective epithermal neutron attenuation length in subsurface, accounting for both absorption and moderation [g cm ⁻²] $\Lambda_{eth,ss} = [\xi(I_{eff,ss} + \Sigma_{sc,ss})]^{-1} = \Sigma_{eth,ss}^{-1} \quad (E.17)$
$\Lambda_{eth,a}$	Effective epithermal neutron attenuation length in the atmosphere, accounting for both absorption and moderation [g cm ⁻²] $\Lambda_{eth,a} = [\xi(I_{eff,a} + \Sigma_{sc,a})]^{-1} = \Sigma_{eth,a}^{-1} \quad (E.18)$
$L_{eth,ss}$	Diffusion length for epithermal neutrons in the subsurface [g cm ⁻²] $L_{eth,ss} = (\sqrt{3\Sigma_{sc,ss}\Sigma_{eth,ss}})^{-1} \quad (E.19)$
$L_{eth,a}$	Diffusion length for epithermal neutrons in the air [g cm ⁻²] $L_{eth,a} = (\sqrt{3\Sigma_{sc,a}\Sigma_{eth,a}})^{-1} \quad (E.20)$
$N_{k,ss,bulk/target}$	Atomic concentration of element k in subsurface (target or bulk specified as additional subscript) [at/g]
$N_{k,a}$	Atomic concentration of element k in air [at/g]
$P_{eth,m}$	Production rate for epithermal production of nuclide m. See eqn B.28.
$\Phi_{eth,ss}(z)$	Epithermal neutron flux in subsurface [neutrons cm ⁻² yr ⁻¹]
Continued on next page	

Table E.8 – continued from previous page

Term	Definition
$\Phi_{eth,ss}^*$	<p>Epithermal neutron flux that would be observed at the land surface if the properties of the medium did not change (e.g. identical to the subsurface.) [neutrons $\text{cm}^{-2} \text{yr}^{-1}$] (See equation B.6)</p> $\Phi_{eth,ss}^* = P_f(0) \frac{R_{eth,ss}}{\Sigma_{eth,ss} - \frac{D_{eth,ss}}{\Lambda_{f,e}^2}} \quad (\text{E.21})$
$\Phi_{eth,a}^*$	<p>Epithermal neutron flux that would be observed at the land surface if the properties of the medium did not change (e.g. atmosphere identical to the air.) [neutrons $\text{cm}^{-2} \text{yr}^{-1}$]</p> $\Phi_{eth,a}^* = P_f(0) \frac{R_{eth,a}}{\Sigma_{eth,a} - \frac{D_{eth,a}}{\Lambda_{f,e}^2}} \quad (\text{E.22})$
$P_f(Z)$	Production rate of epithermal neutrons from fast secondary cosmogenic neutrons as a function of depth. [neutrons $(\text{g air})^{-1} \text{yr}^{-1}$]
$P_f(0)$	is P_f at depth equal to 0 and is a calibrated production rate parameter. [neutrons $(\text{g air})^{-1} \text{yr}^{-1}$]
$p(E_{th})_{ss}$	<p>Resonance escape probability in the subsurface - probability that a neutron will pass through the epithermal energy range to the thermal range without being absorbed [unitless]</p> $p(E_{th}) = \exp\left[-\frac{I_{eff}}{\sum_k \xi_k N_{k,bulk} \sigma_{sc,k}}\right] \quad (\text{E.23})$
Continued on next page	

Table E.8 – continued from previous page

Term	Definition
$p(E_{th})_a$	<p>Resonance escape probability in the air - probability that a neutron will pass through the epithermal energy range to the thermal range without being absorbed [unitless]. Value according to Phillips & Plummer (1996).</p> $p(E_{th})_a = 0.56 \quad (\text{E.24})$
$R_{eth,ss}$	<p>Ratio of epithermal neutron production in the rock to that of the atmosphere [unitless]</p> $R_{eth,ss} = \sqrt{\frac{\bar{A}_{ss}}{A_a}} \quad (\text{E.25})$
$R_{eth,a}$	<p>Ratio of epithermal neutron production in the atmosphere to that of the atmosphere [unitless].</p> $R_{eth,a} = \sqrt{\frac{\bar{A}_a}{A_a}} = 1 \quad (\text{E.26})$
$\Sigma_{eth,ss}$	Effective epithermal loss cross-section in subsurface, by both absorption and energy moderation [$\text{cm}^2 \text{ g}^{-1}$]
$\Sigma_{eth,a}$	Effective epithermal loss cross-section in air, by both absorption and energy moderation [$\text{cm}^2 \text{ g}^{-1}$]
$\Sigma_{sc,ss}$	<p>Macroscopic neutron scattering cross-section in subsurface [$\text{cm}^2 \text{ g}^{-1}$]</p> $\Sigma_{sc,ss} = \sum_k N_{k,bulk} \sigma_{sc,k} \quad (\text{E.27})$
$\Sigma_{sc,a}$	Macroscopic neutron scattering cross-section in air. Constant = 0.3773 [$\text{cm}^2 \text{ g}^{-1}$]
Continued on next page	

Table E.8 – continued from previous page

Term	Definition
$\sigma_{sc,k}$	Neutron scattering cross-section for element k [1×10^{-24} cm ²]
ξ_{bulk}	Macroscopic average log decrement neutron energy loss per collision for the bulk rock $\bar{\xi}_{bulk} = \frac{\sum_k \xi_k \sigma_{sc,k} N_{k,ss,bulk}}{\sum_k \sigma_{sc,k} N_{k,ss,bulk}} \quad (E.28)$
ξ_k	Average log decrement of energy loss for element k
<i>Thermal Production</i>	
$D_{th,ss}$	Diffusion coefficient for thermal neutrons in the subsurface [<i>unitless</i>] $D_{th,ss} = [3\Sigma_{sc,ss}(1 - \frac{2}{3A_{ss}})]^{-1} \quad (E.29)$
$D_{th,a}$	Diffusion coefficient for thermal neutrons in the atmosphere [<i>unitless</i>] $D_{th,a} = [3\Sigma_{sc,a}(1 - \frac{2}{3A_a})]^{-1} \quad (E.30)$
$\Delta\Phi_{th,ss}^*$	Describes the difference between the hypothetical equilibrium thermal neutron flux in the air and the subsurface [neutrons cm ⁻² yr ⁻¹] $\Delta\Phi_{th,ss}^* = \Phi_{th,a}^* - \Phi_{th,ss}^* \quad (E.31)$
Continued on next page	

Table E.8 – continued from previous page

Term	Definition
$f_{th,ss,m}$	Fraction of thermal neutrons absorbed per unit mass by target k that react to form cosmogenic nuclide m [<i>unitless</i>] $f_{th,ss,m} = \frac{\sigma_{th,k} N_{k,ss,target}}{\Sigma_{th,ss}} \quad (\text{E.32})$
$(\mathcal{F} \Delta \Phi)_{th,ss}^*$	Describes the difference between $\Phi_{th,ss}^*$ and the actual flux due to the shape of the thermal neutron flux profile across the interface. See equation B.16
$\Lambda_{th,ss}$	Effective thermal neutron attenuation length for medium i [g cm^{-2}] $\Lambda_{th,ss} = \sum_{th,ss}^{-1} \quad (\text{E.33})$
$L_{th,ss}$	Diffusion length for thermal neutrons in the subsurface [g cm^{-2}] $L_{th,ss} = \sqrt{\frac{D_{th,ss}}{\Sigma_{th,ss}}} \quad (\text{E.34})$
$P_{th,ss,m}$	production rate of nuclide m by thermal neutrons [$\text{atoms g}^{-1}\text{yr}^{-1}$]
$L_{th,a}$	Diffusion length for thermal neutrons in the air [g cm^{-2}] $L_{th,a} = \sqrt{\frac{D_{th,a}}{\Sigma_{th,a}}} \quad (\text{E.35})$
$\Phi_{th,ss}(Z)$	Thermal neutron flux at depth Z [$\text{neutrons cm}^{-2}\text{yr}^{-1}$]
Continued on next page	

Table E.8 – continued from previous page

Term	Definition
$\Phi_{th,ss}^*$	<p>Thermal neutron flux that would be observed at the land surface if the properties of the atmosphere and subsurface were identical [neutrons $\text{cm}^{-2} \text{yr}^{-1}$]</p> $\Phi_{th,ss}^* = \frac{p(E_{th})_a R_{th,ss} \Phi_{eth,ss}^*}{\Lambda_{eth,ss}(\Sigma_{th,ss} - \frac{D_{th,ss}}{\Lambda_{eth,ss}^2})} \quad (\text{E.36})$
$\Phi_{th,a}^*$	<p>Thermal neutron flux that would be observed at the land surface if the properties of the medium did not change and were identical to the atmosphere [neutrons $\text{cm}^{-2} \text{yr}^{-1}$]</p> $\Phi_{th,a}^* = \frac{p(E_{th})_a R_{th,a} \Phi_{eth,a}^*}{\Lambda_{eth,a}(\Sigma_{th,a} - \frac{D_{th,a}}{\Lambda_{eth,a}^2})} \quad (\text{E.37})$
$R_{th,ss}$	<p>Ratio of thermal neutron production in the rock to that in the atmosphere [unitless]</p> $R_{th,ss} = \frac{p(E_{th,ss})}{p(E_{th,a})} \quad (\text{E.38})$
$\sigma_{th,ss,k}$	Elemental thermal neutron cross-section for the subsurface [barns] 1 barn = 10^{-24}cm^2
$\sigma_{th,a,k}$	Elemental thermal neutron cross-section for the air [barns] 1 barn = 10^{-24}cm^2
$\Sigma_{th,ss}$	<p>Macroscopic neutron absorption cross section [$\text{cm}^2 \text{g}^{-1}$]</p> $\Sigma_{th,ss} = \sum_k \sigma_{th,k} N_{k,ss,bulk} = \Lambda_{th,ss}^{-1} \quad (\text{E.39})$
$\Gamma_{th,ss,m}$	Total rate of thermal neutron absorption [neutrons $\text{g}^{-1} \text{yr}^{-1}$]

Muons

Continued on next page

Table E.8 – continued from previous page

Term	Definition
f_i^*	Probability for particle emission to the radionuclide. See Heisinger et al. (2002a).
$f_{i,D}$	Fraction of muons stopped by element k and absorbed by the nucleus before decay of the muon (Fabryka-Martin, 1988) [<i>unitless</i>]
$f_{i,C}$	Chemical compound factor [<i>unitless</i>] Chemical compound factor (for Be, Al, C, see Heisinger et al. (2002a)); values computed on a sample by sample basis for ^{36}Cl due to variations in composition using values from von Egidy & Hartmann (1982). $f_{i,C} = \frac{M_{k,bulk}\Omega_k}{\sum j M_{j,bulk}\Omega_j} \quad (\text{E.40})$
N_{atoms}	Atom number density of the target atom [atoms g $^{-1}$]
Ω	Atomic number of the element. Subscript k refers to the target element and j refers to all elements in the rock.
P	Average probability of muon capture by a nucleus relative to that of oxygen (von Egidy & Hartmann, 1982) [<i>unitless</i>]
$P_{\mu-,m}$	Production rate for negative muon production of nuclide m. See eqns B.3 and B.32.
$P_{\mu,fast,m}$	Production rate for fast muon production of nuclide m. See eqn B.24.
$P_{n,\mu}$	Production rate for muon-induced neutrons. See eqn B.29.
$P_{n,\mu}(Z)$	Total muon-induced neutron production at depth Z [neutrons cm $^{-2}$ yr $^{-1}$]; value at surface is $P_{n,\mu}(0)$ $P_{n,\mu}(Z) = Y_s\Psi_\mu(Z) + 5.8 \times 10^{-6}\Phi_{\mu f}(Z) \quad (\text{E.41})$
Continued on next page	

Table E.8 – continued from previous page

Term	Definition
$\Phi_{\nu,0}$	Vertical muon flux at SLHL as a function of depth. Only valid for depths of $<200,000 \text{ g/cm}^2$. See equation B.17. $[cm^{-2}s^{-1}sr^{-1}]$
$\phi_{\mu f}(Z, \theta)$	Fast muon flux at depth Z [muons $g^{-1}yr^{-1}$]; calculated from the muon code
$\Psi_{\mu-}(Z)$	Slow negative muon stopping rate at depth Z [muons $g^{-1}yr^{-1}$]; calculated from the muon code
$R_{\mu-}(h)$	Rate of negative muons stopping at an atmospheric depth of h
$R_{\mu}(Z)$	Ratio of muon production to epithermal neutron production [<i>unitless</i>] $R_{\mu}(Z) = \frac{S_{el,\mu}P_{n,\mu}(Z)}{S_{el}P_f(0)R_{eth}} \quad (E.42)$
R'_{μ}	Ratio of the muon production rate to the production rate for thermal neutrons. [<i>unitless</i>] See eqn B.33. $R'_{\mu} = \frac{p(E_{th})_a}{p(E_{th})} R_{\mu} \quad (E.43)$
σ_{190}	Cross-section for fast muon production at 190 GeV [<i>mb</i>]. Note: 1 barn= $1 \times 10^{-24} \text{ cm}^2$
Y_s	Average neutron yield per stopped negative muon [neutrons/(stopped negative muon)] $Y_s = \sum_k f_{c,k,bulk} f_{d,k} Y_{n,k} \quad (E.44)$
$Y_{n,k}$	Average neutron yield per captured muon for element k - (Fabryka-Martin, 1988)

Radiogenic Production

$F_{k,bulk}$	Fractional abundance of element k in ppm in the bulk rock
Continued on next page	

Table E.8 – continued from previous page

Term	Definition
P_r	Total radiogenic production from all mechanisms in a particular sample. (equation B.37)
$P_{n,\alpha}$	Production rate of neutrons from alpha particles in neutrons/g/yr
$P_{n,sf}$	Neutron production rate due to the spontaneous fission of ^{238}U
S_k	Mass stopping power of element k for α -particles of a given energy
X	Neutron production factors related to the light isotope composition of the rock matrix. See equation B.40.
Y	Neutron production factors related to the light isotope composition of the rock matrix. See equation B.41.
Y_n^U	Neutron yields of element i per ppm U in equilibrium
Y_n^{Th}	Neutron yields of element i per ppm Th in equilibrium
<i>Accumulation</i>	
D	Depth of the sample with ‘old’ representing the original sample depth and ‘new’ is the updated sample depth, accounting for erosion during the time period
Δt	Time step in the CRONUScalc program.
ϵ	Erosion rate [g/cm ²]
f_{decay}	Decay factor that accounts for the fact that some of the nuclides produced at the beginning of the time period will have decayed by the end of the period. (equation 8)
λ	Decay constant for the nuclide
N_{tot}	Total inventory in the sample up to the current time step
N_{prev}	Inventory from all previous time steps.
P_{tot}	Instantaneous production rate of the nuclide from all mechanisms and is the sum of production from all other mechanisms.

References

- Amidon, W. H., & Farley, K. A. (2010). Mass spectrometric He-3 measurement in He-4-rich phases: Techniques and limitations for cosmogenic He-3 dating of zircon, apatite, and titanite. *Geochemistry Geophysics Geosystems*, 11.
- Amidon, W. H., & Farley, K. A. (2012). Cosmogenic He-3 and Ne-21 dating of biotite and hornblende. *Earth and Planetary Science Letters*, 313, 86–94.
- Amidon, W. H., Farley, K. A., Burbank, D. W., & Pratt-Sitaula, B. (2008). Anomalous cosmogenic (3)He production and elevation scaling in the high Himalaya. *Earth and Planetary Science Letters*, 265, 287–301.
- Amidon, W. H., Rood, D. H., & Farley, K. A. (2009). Cosmogenic He-3 and Ne-21 production rates calibrated against Be-10 in minerals from the Coso volcanic field. *Earth and Planetary Science Letters*, 280, 194–204.
- Argento, D. C., Stone, J. O., Reedy, R. C., & O’Brien, K. (2014). Physics-based modeling of cosmogenic nuclides part II – Key aspects of in-situ cosmogenic nuclide production. *Quaternary Geochronology*, (p. doi:10.1016/j.quageo.2014.09.005).
- Aumer, R. A. (2010). *Calibration of low energy production of ^{36}Cl and the creation of an exposure age calculator*. M.S. Thesis New Mexico Tech.
- Balco, G., Stone, J. O., Lifton, N., & Dunai, T. J. (2008). A complete and easily accessible means of calculating surface exposure ages or erosion rates from ^{10}Be and ^{26}Al measurements. *Quaternary Geochronology*, 3, 174–195.
- Bevington, P. R., & Robinson, D. K. (1992). *Data Reduction and Error Analysis for the Physical Sciences*. (2nd ed.). McGraw-Hill, Inc.
- Bierman, P. R. (1994). Using in situ produced cosmogenic isotopes to estimate rates of landscape evolution: A review from the geomorphic perspective. *Journal of Geophysical Research*, 99, 13885–13896.
- Blard, P.-H., Balco, G., Burnard, P., Farley, K., Fenton, C., Friedrich, R., Jull, A., Niedermann, S., Pik, R., Schaefer, J. M., Scott, E., Shuster, D., Stuart, F., Tibari, B., Winckler, G., & Zimmermann, L. (2014). An

1830 inter-laboratory comparison of cosmogenic ^3He and ^4He in the CRONUS-
1831 P pyroxene standard. *Quaternary Geochronology, CRONUS-Earth Special*
1832 *Volume*, doi:10.1016/j.quageo.2014.08.004.

1833 Blard, P.-H., & Farley, K. (2008). The influence of radiogenic ^4He on cos-
1834 mogenic ^3He determinations in volcanic olivine and pyroxene. *Earth and*
1835 *Planetary Science Letters*, 276, 20–29.

1836 Blard, P.-H., & Pik, R. (2008). An alternative isochron method for measuring
1837 cosmogenic ^3He in lava flows. *Chemical Geology*, 251, 20–32.

1838 Borchers, B., Marrero, S. M., Balco, G., Caffee, M., Goehring, B., Gosse,
1839 J., Lifton, N., Nishiizumi, K., Phillips, F. M., Schaefer, J., & Stone,
1840 J. O. (2015). Geological calibration of spallation production rates in the
1841 CRONUS-Earth project. *Quaternary Geochronology, CRONUS-Earth spe-*
1842 *cial volume*, doi:10.1016/j.quageo.2015.01.009.

1843 Braucher, R., Bourles, D., Merchel, S., Vidani Romani, J., Fernadez-
1844 Mosquera, D., Marti, K., Leanni, L., Chauvet, F., Arnold, M., Aumaitre,
1845 G., & Keddadouche, K. (2013). Determination of muon attenuation lengths
1846 in depth profiles from in situ produced cosmogenic nuclides. *Nuclear In-*
1847 *struments & Methods in Physics Research Section B - Beam Interactions*
1848 *with Materials and Atoms*, 294, 484–490.

1849 Braucher, R., Brown, E. T., Bourles, D., & Colin, F. (2003). In situ produced
1850 ^{10}Be measurements at great depths: implications for production rates by
1851 fast muons. *Earth and Planetary Science Letters*, 211, 251–258.

1852 Braucher, R., Del Castillo, P., Siame, L., Hidy, A. J., & Bourles, D. L. (2009).
1853 Determination of both exposure time and denudation rate from an in situ-
1854 produced ^{10}Be depth profile: A mathematical proof of uniqueness. model
1855 sensitivity and applications to natural cases:. *Quaternary Geochronology*,
1856 4, 56–57.

1857 Braucher, R., Merchel, S., Borgomano, J., & Bourles, D. L. (2011). Pro-
1858 duction of cosmogenic nuclides at great depth: A multi element approach.
1859 *Earth and Planetary Science Letters*, 309, 1–9.

1860 Cerling, T. E. (1990). Dating Geomorphic Surfaces Using Cosmogenic ^3He .
1861 *Quaternary Research*, 33, 148–156.

- 1862 Charalambus, S. (1971). Nuclear transmutation by negative stopped muons
1863 and the activity induced by the Cosmic-Ray muons. *Nuclear Physics*,
1864 *A166*, 145–161.
- 1865 Chmeleff, J., von Blankenburg, F., Kossert, K., & Jakob, D. (2010). Determi-
1866 nation of the ^{10}Be half-life by multicollector ICP-MS and liquid scintillation
1867 counting. *Nuclear Instruments and Methods in Physics Research Section*
1868 *B - Beam Interactions with Materials and Atoms*, *268*, 192–199.
- 1869 Dep, L., Elmore, D., Lipshutz, M., Vogt, S., Phillips, F., & Zreda, M. G.
1870 (1994). Depth dependence of cosmogenic neutron-captured-produced ^{36}Cl
1871 in a terrestrial rock. *Nuclear Instruments and Methods in Physics Research*
1872 *B*, *92*, 301–307.
- 1873 Desilets, D., & Zreda, M. G. (2003). Spatial and temporal distribution of
1874 secondary cosmic-ray nucleon intensities and applications to in situ cos-
1875 mogenic dating. *Earth and Planetary Science Letters*, *206*, 21–42.
- 1876 Desilets, D., Zreda, M. G., Almasi, P. F., & Elmore, D. (2006a). Determina-
1877 tion of cosmogenic ^{36}Cl in rocks by isotope dilution: innovations, validation
1878 and error propagation. *Chemical Geology*, *233*, 185–195.
- 1879 Desilets, D., Zreda, M. G., & Prabu, T. (2006b). Extended scaling factors
1880 for in situ cosmogenic nuclides: New measurements at low latitude. *Earth*
1881 *and Planetary Science Letters*, *246*, 265–276.
- 1882 Dorman, L. I., Valdes-Galicia, J. F., & Dorman, I. V. (1999). Numerical
1883 simulation and analytical description of solar neutron transport in the
1884 Earth’s atmosphere. *Journal of Geophysical Research*, *104*, 22417–22426.
- 1885 Dunai, T. (2001a). Influence of secular variation of the geomagnetic field
1886 on production rates of in situ produced cosmogenic nuclides. *Earth and*
1887 *Planetary Science Letters*, *193*, 197–212.
- 1888 Dunai, T., Binnie, S. A., Hein, A. S., & Paling, S. M. (2014). The effects of a
1889 hydrogen-rich ground cover on cosmogenic thermal neutrons: Implications
1890 for exposure dating. *Quaternary Geochronology*, *22*, 183–191.
- 1891 Dunai, T. J. (2000). Scaling factors for production rates of in situ produced
1892 cosmogenic nuclides: a critical reevaluation. *Earth and Planetary Science*
1893 *Letters*, *176*, 157–169.

- 1894 Dunai, T. J. (2001b). Reply to comment on 'Scaling factors for production
1895 rates of in situ produced cosmogenic nuclides: a critical reevaluation' by
1896 Darin Desilets, Marek Zreda, and Nathaniel Lifton. *Earth and Planetary
1897 Science Letters*, 188, 289–298.
- 1898 Dunai, T. J. (2010). *Cosmogenic Nuclides: Principles, Concepts and Appli-
1899 cations in the Earth Surface Sciences*. Cambridge University Press.
- 1900 Dunai, T. J., Stuart, F. M., Pik, R. I., Burnard, P., & Gayer, E. (2007).
1901 Production of ^3He in crustal rocks by cosmogenic thermal neutrons. *Earth
1902 and Planetary Science Letters*, 258, 228–236.
- 1903 Dunne, J., Elmore, D., & Muzikar, P. (1999). Scaling factors for the rates of
1904 production of cosmogenic nuclides for geometric shielding and attenuation
1905 at depth on sloped surfaces. *Geomorphology*, 27, 3–11.
- 1906 von Egidy, T., & Hartmann, F. J. (1982). Average muonic coulomb capture
1907 probabilities for 65 elements. *Physical Review A*, 26, 2355–2360.
- 1908 Eidelman, S. (2004). Review of Particle Physics*1. *Physics Letters B*, 592,
1909 1–5.
- 1910 Evans, J. M. (2001). *Calibration of the production rates of cosmogenic ^{36}Cl
1911 from potassium*. Ph.D. thesis The Australian National University, Can-
1912 berra. Doctorate of Philosophy.
- 1913 Fabryka-Martin, J. (1988). *Production of radionuclides in the earth and
1914 their hydrogeologic significance, with emphasis on chlorine-36 and iodine-
1915 129*. Ph.D. thesis University of Arizona, Hydrology and Water Resources,
1916 Tucson. Doctor of Philosophy with a major in Hydrology.
- 1917 Farber, D. L., Mériaux, A.-S., & Finkel, R. C. (2008). Attenuation length
1918 for fast nucleon production of ^{10}Be derived from near-surface production
1919 profiles. *Earth and Planetary Science Letters*, 274, 295–300.
- 1920 Farley, K. A., Libarkin, J., Mukhopadhyay, S., & Amidon, W. (2006). Cos-
1921 mogenic and nucleogenic He-3 in apatite, titanite, and zircon. *Earth and
1922 Planetary Science Letters*, 248, 451–461.
- 1923 Feige, Y., Oltman, B. G., & Kastner, J. (1968). Production Rates of Neutrons
1924 in Soils Due to Natural Radioactivity. *Journal of Geophysical Research*,
1925 73, 3135–3142.

- 1926 Friedlander, G., Kennedy, J. W., Macias, E. S., & Miller, J. M. (1981).
1927 *Nuclear and Radiochemistry*. (2nd ed.). John Wiley & Sons, Inc.
- 1928 Gaisser, T. K. (1990). *Cosmic Rays and Particle Physics*. Cambridge: Cam-
1929 bridge University Press.
- 1930 Goehring, B. M., Kelly, M. A., Schaefer, J. M., Finkel, R., & Lowell, T. V.
1931 (2010a). Dating of raised marine and lacustrine deposits in east Green-
1932 land using beryllium-10 depth profiles and implications for estimates of
1933 subglacial erosion. *Journal of Quaternary Science*, *26*, 865–874.
- 1934 Goehring, B. M., Kurz, M. D., Balco, G., Schaefer, J. M., Licciardi, J., &
1935 Lifton, N. (2010b). A reevaluation of in situ cosmogenic ^3He production
1936 rates. *Quaternary Geochronology*, *5*, 410–418.
- 1937 Goehring, B. M., Schimmelpfennig, I., & Schaefer, J. M. (2014). Capabilities
1938 of the lamont-doherty earth observatory in situ ^{14}C extraction laboratory
1939 updated. *Quaternary Geochronology*, *19*, 194–197.
- 1940 Goldhagen, P., Reginatto, M., Kniss, T., Wilson, J. W., Singleterry, R. C.,
1941 Jones, I. W., & Steveninck, W. V. (2002). Measurement of the energy
1942 spectrum of cosmic-ray induced neutrons aboard an ER-2 high-altitude
1943 airplane. *Nuclear Instruments and Methods in Physics Research A*, *476*,
1944 42–51.
- 1945 Gosse, J. C., & Phillips, F. M. (2001). Terrestrial in situ cosmogenic nuclides:
1946 theory and application. *Quaternary Science Reviews*, *20*, 1475–1560.
- 1947 Granger, D., & Muzikar, P. (2001). Dating sediment burial with in situ-
1948 produced cosmogenic nuclides: theory, techniques, and limitations. *Earth
1949 and Planetary Science Letters*, *188*, 269–281.
- 1950 Granger, D. E. (2006). A review of burial dating methods using ^{26}Al and
1951 ^{10}Be . In L. Siame, D. L. Bourles, & E. T. Brown (Eds.), *In situ-produced
1952 cosmogenic nuclides and quantification of geological processes* (pp. 1–16).
1953 volume 415 of *Geological Society of America Special Papers*.
- 1954 Granger, D. E., & Smith, A. L. (2000). Dating buried sediments using ra-
1955 dioactive decay and muogenic production of Al-26 and Be-10. *Nuclear
1956 Instruments & Methods in Physics Research*, *B126*, 822–826.

- 1957 Groom, D., Mokhov, N., & Striganov, S. (2001). Muon stopping power and
1958 range tables 10 MeV-100 TeV. *Atomic Data and Nuclear Data Tables*, 78,
1959 183–356.
- 1960 Handwerger, D. A., Cerling, T. E., & Bruhn, R. L. (1999). Cosmogenic ^{14}C
1961 in carbonate rocks. *Geomorphology*, 27, 13–24.
- 1962 Hein, A. S., Hulton, N. R., Dunai, T. J., Schnabel, C., Kaplan, M. R.,
1963 Naylor, M., & Xu, S. (2009). Middle Pleistocene glaciation in Patagonia
1964 dated by cosmogenic-nuclide measurements on outwash gravels. *Earth*,
1965 286, 184–197.
- 1966 Heisinger, B., Lal, D., Jull, A. J. T., Kubik, P., Ivy-Ochs, S., Knie, K.,
1967 & Nolte, E. (2002a). Production of selected cosmogenic radionuclides by
1968 muons: 2. Capture of negative muons. *Earth and Planetary Science Let-*
1969 *ters*, 200, 357–369.
- 1970 Heisinger, B., Lal, D., Jull, A. J. T., Kubik, P., Ivy-Ochs, S., Neumaier,
1971 S., Knie, K., Lazarev, V., & Nolte, E. (2002b). Production of selected
1972 cosmogenic radionuclides by muons: 1. Fast muons. *Earth and Planetary*
1973 *Science Letters*, 200, 345–355.
- 1974 Hidy, A. J., Gosse, J. C., Pederson, J. L., Mattern, J. P., & Finkel,
1975 R. C. (2010). A geologically constrained Monte Carlo approach to mod-
1976 eling exposure ages from profiles of cosmogenic nuclides: An example
1977 from Lees Ferry, Arizona. *Geochemistry Geophysics Geosystems*, 11, doi:
1978 10.1029/2010GC003084.
- 1979 Hillas, A. M. (1972). *Cosmic Rays*. Oxford: Pergamon Press.
- 1980 Jull, A., Scott, E., & Bierman, P. (2013). The CRONUS-Earth inter-
1981 comparison for cosmogenic isotope analysis. *Quaternary Geochronology*,
1982 *CRONUS-Earth Special Volume*, doi:10.1016/j.quageo.2013.09.003.
- 1983 Jull, A., Scott, E., & Marrero, S. (2011). The CRONUS-Earth inter-
1984 comparison for cosmogenic isotope analysis. In *The Twelfth International*
1985 *Conference on Accelerator Mass Spectrometry* (p. 242).
- 1986 Kim, K. J., & Englert, P. A. J. (2004). Profiles of in situ ^{10}Be and ^{26}Al
1987 at great depths at the Macraes Flat, East Otago. *Earth and Planetary*
1988 *Science Letters*, 223, 113–126.

- 1989 Kim, K. J., Lal, D., Englert, P. A. J., & Southon, J. (2007). In situ ^{14}C depth
1990 profile of subsurface vein quartz samples from Macraes Flat New Zealand.
1991 *Nuclear Instruments and Methods in Physics Research Section B - Beam*
1992 *Interactions with Materials and Atoms*, 259, 632–636.
- 1993 Korschinek, G., Bergmaier, A., Faestermann, T., Gerstmann, U. C., Knie, K.,
1994 Rugel, G., Wallner, A., Dillmann, I., Dollinger, G., Lierse von Gostomski,
1995 C., Kossert, K., Maiti, M., Poutivtsec, M., & Remmert, A. (2010). A
1996 new value for the half-life of ^{10}Be by heavy-ion elastic recoil detection and
1997 liquid scintillation counting. *Nuclear Instruments and Methods in Physics*
1998 *Research Section B - Beam Interactions with Materials and Atoms*, B268,
1999 187–191.
- 2000 Korte, M., & Constable, C. G. (2005). Continuous geomagnetic field models
2001 for the past 7 millennia: 2. CALS7K. *Geochemistry, Geophysics, Geosys-*
2002 *tems*, 6, Q02H16.
- 2003 Kurz, M. D. (1986). Cosmogenic helium in a terrestrial igneous rock. *Nature*,
2004 320, 435–439.
- 2005 Laj, C., Kissel, C., Beer, J., Channell, J., Kent, D., Lowrie, W., & Meert, J.
2006 (2004). High resolution global paleointensity stack since 75 kyr (GLOPIS-
2007 75) calibrated to absolute values. *Timescales of the Geomagnetic Field*,
2008 (pp. 255–265).
- 2009 Lal, D. (1958). *Investigations of Nuclear Interactions Produced by Cosmic*
2010 *Rays*. Phd Bombay University.
- 2011 Lal, D. (1987). Production of ^3He in terrestrial rocks. *Chemical Geology*, 66,
2012 89–98.
- 2013 Lal, D. (1988). In Situ-Produced Cosmogenic Isotopes in Terrestrial Rocks.
2014 *Ann. Rev. Earth Planet. Sci*, 16, 355–388.
- 2015 Lal, D. (1991). Cosmic ray labeling of erosion surfaces: In situ nuclide
2016 production rates and erosion models. *Earth and Planetary Science Letters*,
2017 104, 424–439.
- 2018 Lal, D., & Peters, B. (1967). Cosmic ray produced radioactivity on the earth.
2019 In K. Sitte (Ed.), *Hanbuch der Physik* (pp. 551–612). Berlin: Springer.

- 2020 Lifton, N., Sato, T., & Dunai, T. J. (2014). Scaling in situ cosmogenic
2021 nuclide production rates using analytical approximations to atmospheric
2022 cosmic-ray fluxes. *Earth and Planetary Science Letters*, 386, 149–160.
- 2023 Lifton, N., Smart, D. F., & Shea, M. A. (2008). Scaling time-integrated in
2024 situ cosmogenic nuclide production rates using a continuous geomagnetic
2025 model. *Earth and Planetary Science Letters*, 268, 190–201.
- 2026 Lifton, N. A., Bieber, J. W., Clem, J. M., Duldig, M. L., Evenson, P., Hum-
2027 ble, J. E., & Pyle, R. (2005). Addressing solar modulation and long-term
2028 uncertainties in scaling in situ cosmogenic nuclide production rates. *Earth
2029 and Planetary Science Letters*, 239, 140–161.
- 2030 Lifton, N. A., Jull, A. J. T., & Quade, J. (2001). A new extraction tech-
2031 nique and production rate estimate for in situ cosmogenic ^{14}C in quartz.
2032 *Geochimica et Cosmochimica Acta*, 65, 1953–1969.
- 2033 Lupker, M., Hippe, K., Kober, F., Wacker, L., Braucher, R., Bourles, D. L.,
2034 Vidal Romani, J., & Weiler, R. (2013). Depth-dependence of the pro-
2035 duction rate of in-situ ^{14}C in quartz. *American Geophysical Union Fall
2036 Meeting, Poster EP13C-0849*.
- 2037 Lupker, M., Hippe, K., Wacker, L., Kober, F., Maden, C., Braucher, R.,
2038 Bourles, D., Vidal Romani, J., & Wieler, R. (2015). Depth-dependence of
2039 the production rate of in-situ ^{14}C in quartz from the Leymon High core,
2040 Spain. *Quaternary Geochronology*, 28, 80–87.
- 2041 Marrero, S., Phillips, F., Caffee, M., & Gosse, J. (2015). CRONUS-Earth
2042 cosmogenic ^{36}Cl calibration. *Quaternary Geochronology, CRONUS-Earth
2043 Special Volume*, submitted.
- 2044 Marrero, S. M. (2012). *Calibration of Cosmogenic Chlorine-36*. Doctorate
2045 New Mexico Tech, Dept of Earth & Environmental Science.
- 2046 Marrero, S. M., Phillips, F. M., Caffee, M., Stone, J. O., Swanson, T., &
2047 Hinz, M. (this volume, submitted). Resampling of puget lowlands yields
2048 lower discrepancy in cosmogenic chlorine-36 production rates. *Quaternary
2049 Geochronology, CRONUS Special Volume*.
- 2050 Masarik, J., Kollar, D., & Vanya, S. (2000). Numerical simulation of in
2051 situ production of cosmogenic nuclides: Effects of irradiation geometry.

- 2052 *Nuclear Instruments and Methods in Physics Research Section B: Beam*
2053 *Interactions with Materials and Atoms*, 172, 786–789.
- 2054 Mughabghab, S. (2006). *Atlas of Neutron Resonances: Resonance parameters*
2055 *and thermal cross-sections Z=1-100*. Elsevier Science Ltd.
- 2056 Nishiizumi, K., Imamura, M., Caffee, M. W., Southon, J. R., Finkel, R. C.,
2057 & McAninch, J. (2007). Absolute calibration of ^{10}Be AMS standards.
2058 *Nuclear Instruments and Methods in Physics Research Section B - Beam*
2059 *Interactions with Materials and Atoms*, 258, 403–413.
- 2060 Nishiizumi, K., Winterer, E. L., Kohl, C. P., Klein, J., Middleton, R., Lal,
2061 D., & Arnold, J. R. (1989). Cosmic ray production rates of ^{10}Be and ^{26}Al
2062 in quartz from glacially polished rocks. *Journal of Geophysical Research*,
2063 94, 9.
- 2064 Phillips, F., Stone, W. D., & Fabryka-Martin, J. (2001). An improved
2065 approach to calculating low-energy cosmic-ray neutron fluxes near the
2066 land/atmosphere interface. *Chemical Geology*, 175, 689–701.
- 2067 Phillips, F. M., Argento, D. C., Balco, G., Caffee, M. W., Clem, J., Dunai,
2068 T., Finkel, R., Goehring, B., Gosse, J. C., Hudson, A., Jull, T. A., Kelly,
2069 M., Kurz, M., Lal, D., Lifton, N., Marrero, S. M., Nishiizumi, K., Reedy,
2070 R., Schaefer, J., Stone, J. O., Swanson, T., & Zreda, M. G. (2015). The
2071 cronus-earth project: A synthesis. *Quaternary Geochronology*, *CRONUS-*
2072 *Earth*, submitted.
- 2073 Phillips, F. M., & Plummer, M. A. (1996). CHLOE: a program for interpret-
2074 ing in-situ cosmogenic nuclide data for surface exposure dating and erosion
2075 studies. *Radiocarbon (Abstr. 7th Int. Conf. Accelerator Mass Spectrom-*
2076 *etry)*, 38, 98–99.
- 2077 Pigati, J., Lifton, N., Jull, A., & Quade, J. (2010). A simplified in situ
2078 cosmogenic ^{14}C extraction system. *Radiocarbon*, 52, 1236–1243.
- 2079 Pigati, J. S., & Lifton, N. (2004). Geomagnetic effects on time-integrated
2080 cosmogenic nuclide production with emphasis on in situ ^{14}C and ^{10}Be .
2081 *Earth and Planetary Science Letters*, 226, 193–205.

- 2082 Reedy, R. C. (2013). Cosmogenic nuclide production rates: Reaction cross
2083 section update. *Nuclear Instruments and Methods in Physics Research*
2084 *Section B - Beam Interactions with Materials and Atoms*, 294, 470–474.
- 2085 Sato, T., Yasuda, H., Niita, K., Endo, A., & Sihver, L. (2008). Development
2086 of PARMA: PHITS-based analytical radiation model in the atmosphere.
2087 *Radiation Research*, 170, 244–259.
- 2088 Schaefer, J. M., Denton, G. H., Kaplan, M. R., Putnam, A. E., Finkel, R.,
2089 Barrell, D. J. A., Andersen, B. G., Schwartz, R., Mackintosh, A., Chinn,
2090 T., & Schluchter, C. (2009). High-frequency holocene glacier fluctuations
2091 in new zealand differ from the northern signature. *Science*, 324, 622–625.
- 2092 Schaefer, J. M., Winckler, G., Blard, P.-H., Balco, G., Shuster, D., Friedrich,
2093 R., & Schluechter, C. (2014). Performance of CRONUS-P: a pyroxene
2094 reference material for helium isotope analysis. *Quaternary Geochronology*,
2095 *CRONUS-Earth Special Volume*, doi:10.1016/j.quageo.2013.09.003.
- 2096 Schaller, M., Ehlers, T., Blum, J., & Kallenberg, M. (2009). Quan-
2097 tifying glacial moraine age, denudation, and soil mixing with cosmo-
2098 genic nuclide depth profiles. *Journal of Geophysical Research*, 114, doi:
2099 10.1029/2007/JF000921.
- 2100 Schimmelpfennig, I. (2009). *Cosmogenic ^{36}Cl in Ca and K rich minerals:*
2101 *analytical developments, production rate calibrations and cross calibration*
2102 *with ^3He and ^{21}Ne* . Doctorale Universite Paul Cezanne Aix-Marseille III
2103 Cerege.
- 2104 Schimmelpfennig, I., Benedetti, L., Finkel, R., Pik, R., Blard, P.-H., Bourlès,
2105 D., Burnard, P., & Williams, A. (2009). Sources of in-situ ^{36}Cl in
2106 basaltic rocks. Implications for calibration of production rates. *Quater-*
2107 *nary Geochronology*, (pp. 441–461).
- 2108 Schimmelpfennig, I., Benedetti, L., Pik, R., Burnard, P., Blard, P., Dunai,
2109 T. J., & Bourles, D. L. (2008). In situ cosmogenic ^{36}Cl production rate
2110 calibration from Ca and K in lava flows. *Goldschmidt Abstracts*, .
- 2111 Shea, M. A., & Smart, D. F. (1983). A world grid of calculated cosmic ray
2112 vertical cutoff rigidities for 1980. *Proceedings from the 18th International*
2113 *Cosmic Ray Conference*, 3, 415–418.

- 2114 Stone, J. (2000). Air pressure and cosmogenic isotope production. *Journal*
2115 *of Geophysical Research*, *105*, 23753–23760.
- 2116 Stone, J. O. H., Evans, J. M., Fifield, L. K., Allan, G. L., & Cresswell,
2117 R. G. (1998). Cosmogenic chlorine-36 production in calcite by muons.
2118 *Geochimica et Cosmochimica Acta*, *62*, 433–454.
- 2119 Uppala, S., Kallberg, P., Simmons, A., Andrae, U., Bechtold, V., Fiorino,
2120 M., Gibson, J., Haseler, J., Hernandez, A., Kelly, G., Li, X., Onogi, K.,
2121 Saarinen, S., Sokka, N., Allan, R., Andersson, E., Arpe, K., Balmaseda,
2122 M., Beljaars, A., Berg, L., Bidlot, J., Bormann, N., Caires, S., Chevallier,
2123 F., Dethof, A., Dragosavac, M., Fisher, M., Fuentes, M., Hagermann, S.,
2124 Holm, E., Hoskins, B., Isaksen, I., Janssen, P., Jenne, R., McNally, A.,
2125 Mahfouf, J., Morcrette, J., Rayner, N., Saunders, R., Simon, P., Sterl, A.,
2126 Trenberth, K., Untch, A., Vasiljevic, D., Viterbo, P., & Woollen, J. (2005).
2127 The ERA-40 reanalysis. *Quarterly Journal of the Royal Meteorological*
2128 *Society*, *131*, 2961–3012.
- 2129 Vermeesch, P., Balco, G., Blard, P.-H., Dunai, T. J., Kober, F., Nieder-
2130 mann, S., Shuster, D., Strasky, S., Stuart, F., Wieler, R., & Zimmerman,
2131 L. (2012). Interlaboratory comparison of cosmogenic ^{21}Ne in quartz. *Qua-*
2132 *ternary Geochronology*, <http://dx.doi.org/10.1016/j.quageo.2012.11.009>,
2133 *CRONUS-Earth Special Volume*.
- 2134 Wieler, R., Beer, J., & Leya, I. (2013). The Galactic Cosmic Ray Inten-
2135 sity over the Past 10^6 - 10^9 Years as Recorded by Cosmogenic Nuclides in
2136 Meteorites and Terrestrial Samples. *Space Science Reviews*, *176*, 351 –
2137 363.
- 2138 Williams, A., Stuart, F., Day, S., & Phillips, W. (2005). Using pyroxene
2139 microphenocrysts to determine cosmogenic ^3He concentrations in old vol-
2140 canic rocks: an example of landscape development in central gran canaria.
2141 *Quaternary Science Reviews*, *24*, 211–222.
- 2142 Ziegler, L. B., Constable, C. G., Johnson, C. L., & Tauxe, L. (2011).
2143 PADM2M: a penalized maximum likelihood model of the 0-2 Ma paleo-
2144 magnetic axial dipole moment. *Geophys. J. Int.*, doi: 10.1111/j.1365-
2145 246X.2010.04905.x, .

2146 Zreda, M., Desilets, D., Ferre, T. P. A., & Scott, R. L. (2008). Measuring soil
2147 moisture content non-invasively at intermediate spatial scale using cosmic-
2148 ray neutrons. *Geophysical Research Letters*, 35.